Integrated Ferroelectrics, 141:154–166, 2013

ISSN: 1058-4587 print / 1607-8489 online
DOI: 10.1080/10584587.2013.787778

Taylor & Francis
Taylor & Francis Group

Materials Characterization of Potassium Sodium Niobate based Tellurite Glass-Ceramics

PLOYPAILIN YONGSIRI[1,*] AND KAMONPAN PENGPAT[1,2]

[1]Department of Physics and Materials Science, Faculty of Science, Chiang Mai University, Chiang Mai 50200, Thailand
[2]Materials Science Research Center, Faculty of Science, Chiang Mai 50200, Thailand

In this research, materials characterization of transparent glass-ceramics containing ferroelectric potassium sodium niobate ($K_{0.5}Na_{0.5}$)NbO_3 (KNN) crystals in a tellurite glass system were studied. The samples were prepared via an incorporation method. Glass-ceramics containing KNN crystals were successfully fabricated by mixing KNN calcined powder with TeO_2 of about 70 and 80 mol% and melting at 800°C for 15 min in a platinum crucible. The prepared glasses were then subjected to heat treatment at 350–550°C. The optical properties of the samples were characterized by UV-Vis-NIR and ellipsometer. It was found that heat treatment temperature had significantly affected the optical properties. XRD patterns of the glass-ceramics revealed an amorphous-like structure with different degrees of crystallinity. SEM results confirmed the XRD data, where the degree of crystallinity increased with increasing heat treatment temperature.

Keywords Potassium sodium niobate; Glass-ceramics; Tellurium dioxide

1. Introduction

Glass-ceramics containing ferroelectric crystals, such as $BaTiO_3$:BT, ($K_{0.5}Na_{0.5}$)NbO_3:KNN and $LiNbO_3$ have been studied extensively as they possesses the properties of non-porous glasses and solid crystals, giving rise to novel materials that have the good mechanical properties of glass and the electro-optical properties of ferroelectric crystals [1–2]. Among these crystals, KNN is of particular interest due to its good electrical and non-linear optical properties [3]. Moreover, KNN contains no toxic lead oxide, which can easily evaporate and accumulate in the human body. Thus, the KNN crystal has the potential benefit of reducing the use of lead-based materials which have been used for many decades in electrical industries worldwide [4].

Tellurium oxide (TeO_2), one of the glass forming oxides, is used for producing glasses with high refractive index (n2). Moreover, its IR transmission range is up to 6 μm and it possesses a large third order non-linear optical susceptibility (χ^3) [5–6]. These unique optical and electrical properties make tellurite glass a potential candidate material for IR windows, all-optical switching devices and laser hosts [7].

In our previous work [8], we prepared glass ceramic KNN-SiO_2 which contained KNN single phase by the incorporation method. The resulting glass-ceramics have high

Received June 30, 2012; in final form October 16, 2012.
*Corresponding author. E-mail: kamonpan.p@cmu.ac.th

transmission and high dielectric constant. The crystal size and crystallinity were found to increase with increasing heat treatment temperature, which then plays an important role in controlling the properties of the glass-ceramics, including physical, optical, and dielectric properties. The transparency of the glass samples, however, decreased with increasing crystal size. The maximum room temperature dielectric constant (ε_r) was 474 at 10 kHz with a low loss (tanδ) of around 0.02 at 10 kHz.

In this work, KNN powders were firstly prepared by a mixed oxide method and subsequently mixed with TeO_2 in a Pt crucible, and the well mixed powder melted at a suitable temperature to form a glass. The crystallization of the KNN crystals in the glass was accomplished by heat treatment processes which were also used to control the KNN crystal shape and size. Here, we report the physical, electrical and optical properties of the prepared KNN glass-ceramics generated using TeO_2 and a modified incorporation method. Phase identification, thermal analysis, percent transmission and microstructures of the prepared glass and glass-ceramics were investigated by X-ray diffraction [XRD], differential thermal analysis [DTA], UV visible spectroscopy and scanning electron microscopy [SEM], respectively.

2. Experimental

From our previous work, it was found that the incorporation method was a suitable way to prepare glass-ceramics containing KNN single phase [8]. In the incorporation method [9–10], KNN precursor was first prepared by using Na_2CO_3 (Riedel-de Haën, 99.9%), K_2CO_3 (Sigma-Aldrich, 99.9%) and Nb_2O_5 (Sigma-Aldrich, 99.9%) powders. From a related study [11], KNN single phase was successfully prepared by excess Na_2CO_3 and K_2CO_3 of about 5mol% with ratio 1:1 in order to achieve the pure phase. The starting powders were mixed by a ball milling technique for 24 hours in a polyethylene bottle using zirconia balls and acetone as grinding and liquid media respectively. Well mixed powder was dried by using a magnetic stirring hot plate at 40–60°C for 24 hours and the sample was kept in an oven for 24 hours at the same temperature. Then, the dried powder was calcined in an electric furnace at 900°C for 5 hours with a heating rate of 1.67°C/min and a cooling rate of 5°C/min. The prepared KNN powder was agglomerated and therefore, was sieved to separate the fine powder. To identify some phase of this KNN powder, XRD [X-ray diffractometer; D500 type, Siemens, UK], FE-SEM [scaning electron microscope; JSM 6335F type, JEOL, JP] and EDS [energy dispersive spectroscopy] were employed. The KNN powders were then mixed with the glass forming substance; TeO_2 at a composition of 70 and 80 mol%, in order to form transparent glass-ceramics. The components were mixed in a platinum crucible and subsequently melted at 800°C for 15 min and then quenched between stainless steel plates. The quenched glass was immediately annealed in another electric furnace for 6 hours to release their stress. Thermal properties of as-received glass were measured to find the glass transition temperature (T_g) and crystallization temperature (T_c) by using DTA [Differential thermal analysis; Du Pont Instrument, USA]. Then, as-received glass was subjected to heat treatment (HT) at temperatures ranging between 300 to 550°C depending upon the T_g and T_c of each glass, for 4 hours. Heating rate of 5°C/min and cooling rate of 10°C/min was employed.

To analyze the glass and glass-ceramic properties, various techniques were employed. XRD and SEM techniques were used to investigate the phase composition and to observe the microstructure of the glass and glass-ceramic samples. The room temperature dielectric constant (ε_r) and dielectric loss (tanδ) of the glass-ceramics were measured at various frequencies from 10 kHz to 1 MHz using a precision LCZ meter [E4980A type, Agilent

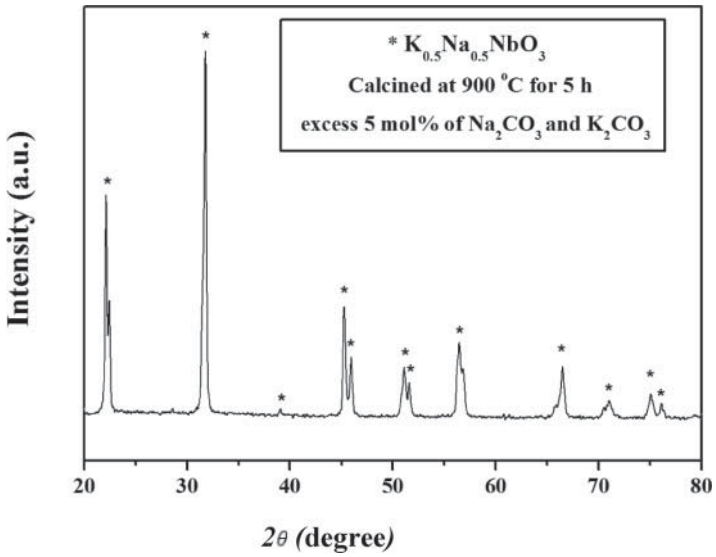

Figure 1. X-ray diffraction patterns of KNN with 5 mol% of $Na_2CO_3$and K_2CO_3 in ratio 1:1 and calcined at 900°C for 5 h (* $K_{0.5}Na_{0.5}NbO_3$ phase)

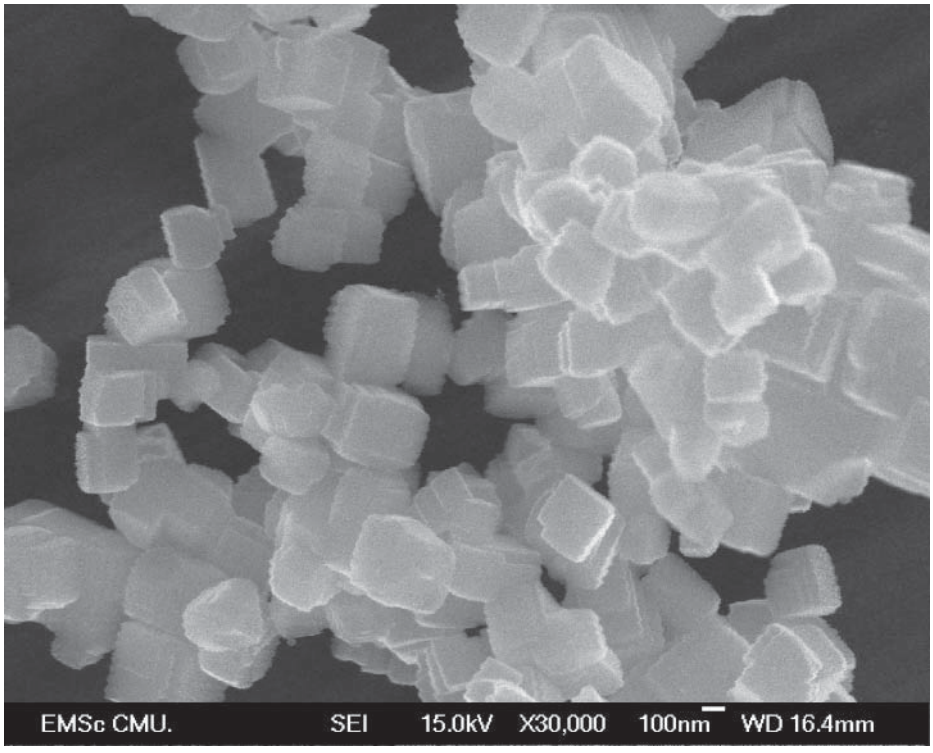

Figure 2. The SEM image of KNN powder obtained cubic crystal sizes 100–200 nm at 900°C for 5 hours

Technologies, Malaysia]. The transmission and refractive index values were measured by UV-Vis-NIR Spectrophotometer [VARIAN Cary 50, USA; λ = 190–1100 nm.] and Ellipsometer [J.A. Woollam Co., Inc. series α-SE^{TM}, USA].

3. Result and Discussion

Powder Characterization

Generally, to prepare the single phase of KNN powder by conventional mixed oxide method is rather difficult. Many studies have revealed that the alkaline carbonate precursor was sensitive to moisture, leading to difficulty in obtaining the KNN single phase [4]. Bomlai et al. [11] reported that an excess of 1, 3 and 5 mol% of Na_2CO_3 and K_2CO_3 with ratio 1:1 resulted in the ease of formation of KNN single phase. We therefore have chosen to prepare KNN powder with an excess of 5 mol% Na_2CO_3 and K_2CO_3 (ratio 1:1). XRD result of the calcined powders is shown in Fig. 1.

From Fig. 1, it is clearly seen that the KNN single phase can be achieved by the excess of 5 mol% Na_2CO_3 and K_2CO_3. To confirm single phase, data was compared with JCPDS file number 77-0038.

It can be assumed that by using stoichiometric compositions of Na_2CO_3, K_2CO_3 and Nb_2O_5 to prepare the KNN powder, the incomplete reaction via calcination method is likely to occur because of the compositional fluctuation from easily volatile precursors such as Na_2CO_3 and K_2CO_3 at high temperature [3].

The FE-SEM micrograph in Fig. 2 shows the morphology of the prepared KNN crystals with cubic shape and size ranging from 100-200 nanometers. The EDS study (Table 1) also confirms the composition of the prepared powder which has the weight and atomic ratio of Na:K close to 1:1 as expected.

Glass Preparation and Properties

Transparent KNN glasses were obtained after melting and quenching of KNN and TeO-$_2$ powder with weight ratio 30:70 and 20:80 mol%. As-received glasses were orange in color

Table 1
Quantitative analysis of calcined KNN powder at 900°C for 5 hours by EDS technique.

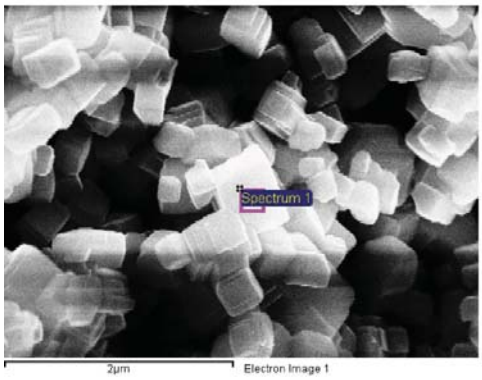

Element	Weight%	Atomic%
O K	41.35	72.88
Na K	6.14	7.53
K K	8.73	6.30
Nb L	43.78	13.29
Totals	100.00	

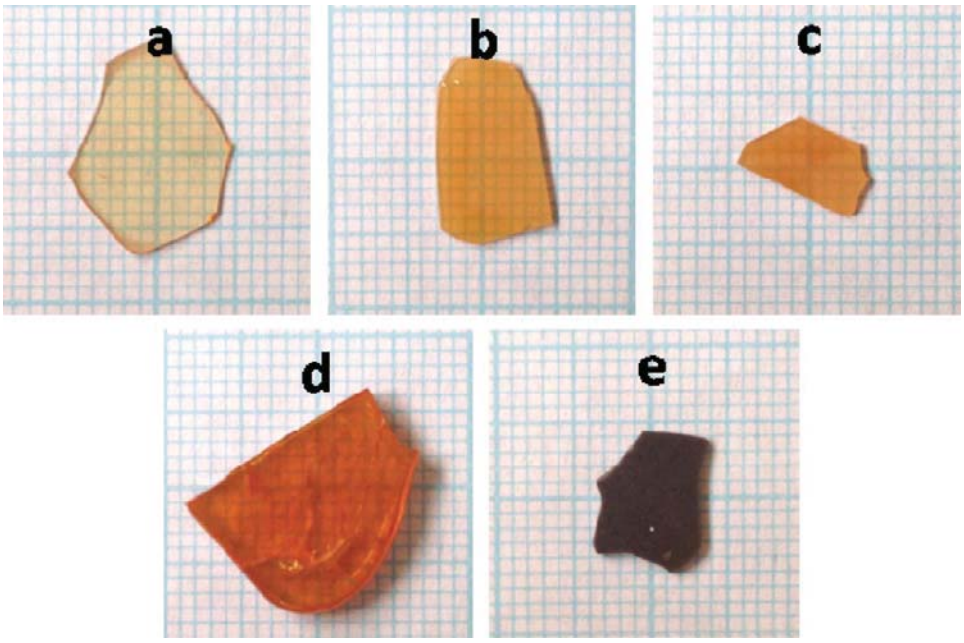

Figure 3. Physical appearances of 30KNN-70TeO_2 glass-ceramics after various heat treatment (HT) temperatures **a)** 300°C **b)** 325°C **c)** 350°C **d)** 420°C and **e)** 522°C.

and had low mechanical strength as shown in Fig. 3 and 4. Thus, annealing is an important process which was employed to reduce stress in the quenched glass. Annealing temperature for the glass were decided from the DTA traces of the two glasses and were chosen near their T_g points. DTA traces are shown in Fig. 5.

Fig. 5 shows that 30KNN-70TeO_2 and 20KNN-80TeO_2 glasses have T_g around 300°C. Crystallization temperatures of the two glass compositions were different. For the 30KNN-70TeO_2 glass, T_{c1} and T_{c2} at 420°C and 522°C were observed while for 20KNN- 80TeO_2 glass, T_{c1} and T_{c2} were at 408°C and 498°C. Small differences between these thermal parameters may arise from the difference in TeO_2 concentration. It may be assumed by considering the difference between T_{c1} and T_g ($T_{c1}-T_g$) of each glass that the 30KNN-70TeO_2 (T_{c1}-T_g ≈120°C) is more stable than that of the 20KNN- 80TeO_2 (with $T_{c1}-T_g$ ≈108°C).

The heat treatment process was employed in order to crystallize KNN crystals in the glass matrix with the desired crystal size. The glasses were subjected to a heat treatment schedule at 300°C, 325°C, 350°C and at their T_{c1} and T_{c2}. The heat treatment near T_g in the range of 300–350°C was performed to achieve transparent glass-ceramics, while the heat treatment at T_{c1} and T_{c2} was for checking formation of crystal phases at their crystallization temperatures. The appearances of all glass-ceramics are displayed in Fig. 3 and Fig. 4.

Glass-Ceramics Properties

The XRD results in Fig. 6 of the heat treated glass-ceramics revealed that KNN; $(K_{0.5}Na_{0.5})NbO_3$ was not retained by the incorporation method. This may be due to the very

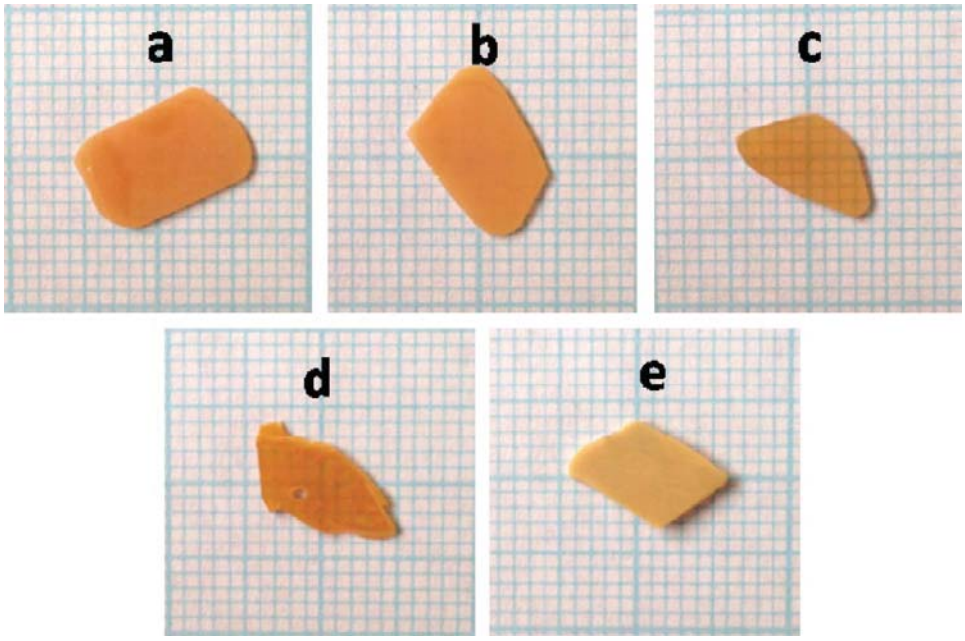

Figure 4. Physical appearances of 20KNN-80TeO_2 glass-ceramics at various heat treatment (HT) temperatures **a)** 300°C **b)** 325°C **c)** 350°C **d)** 408°C and **e)** 498°C.

low viscosity of telluride glasses at their melting temperatures, giving rise to compositional fluctuation in these glasses [5–7]. However, the heat treatment temperature plays an important role in controlling the crystal phase in these glass-ceramics. At low HT from 300°C to 350°C, the resulting glass-ceramics for both compositions, contained similar crystal phase,

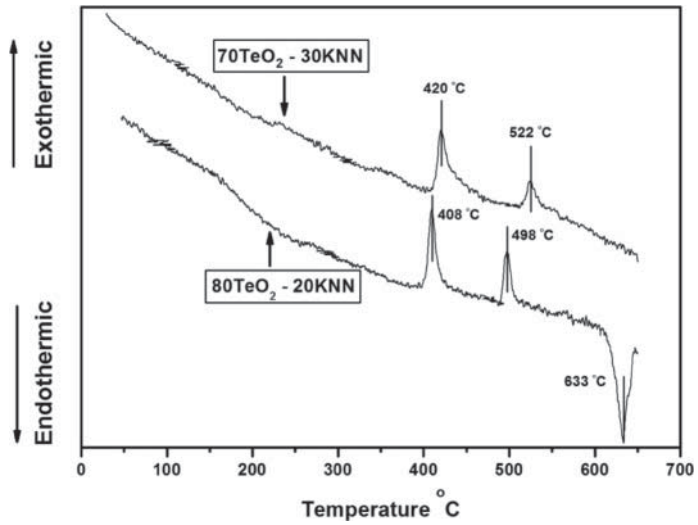

Figure 5. Thermal analysis (DTA) of KNN-TeO_2 glasses which were melted at 900°C for 15 minutes and quenched between stainless steel plates at room temperature.

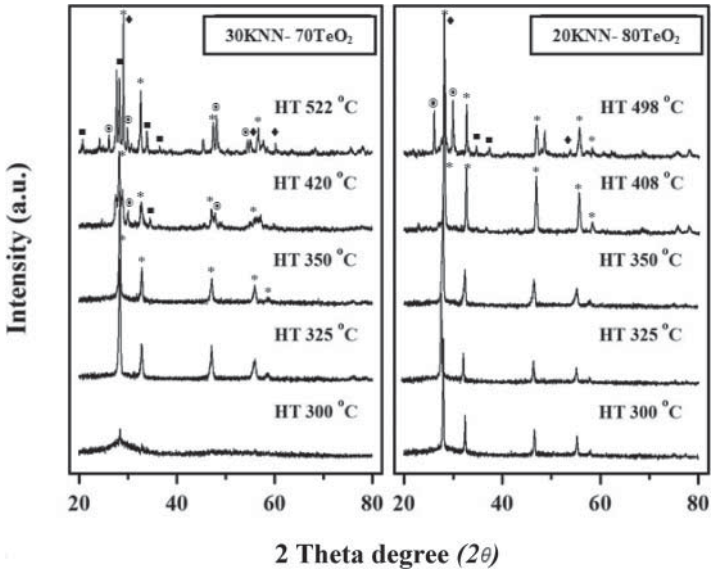

Figure 6. XRD patterns of two series of glass-ceramics after various HT temperatures. (■ $KNbTeO_6$ peaks, ⊙ T_eO_2 peaks and ♦ $Na_2Nb_4O_{11}$ peaks)

which may be identified as the typical cubic structure of (K,Na)NbO_3 with random variation of K and Na ions in the A-site of the unit cell. This result is consistent with the work done by Jeong et al. [10] who studied the glasses of xK_2O-(14-x)Na_2O-14Nb_2O_5–72TeO_2 where x = 0∼12 mol%. For HT at 300°C, the glass-ceramics sample for the 30KNN-70TeO_2 glass series exhibited slightly amorphous patterns with a trace at crystalline peaks of the same cubic (K,Na)NbO_3 phase. For the 20KNN-80TeO_2 series, the crystalline peaks of the cubic phase were more revealed, indicating a higher degree of crystallinity. This is more evidence of greater glass stability of the 30KNN-70TeO_2 glass series over that of

Table 2
The calculated average crystallite sizes in two glass compositions.

Heat treatment temperature (°C)	Crystallite size (nm)
30KNN- 70TeO_2	
300	35
325	62
350	31
420 (T_{c1})	35
522 (T_{c2})	46
20KNN- 80TeO_2	
300	46
325	111
350	69
408 (T_{c1})	111
498 (T_{c2})	62

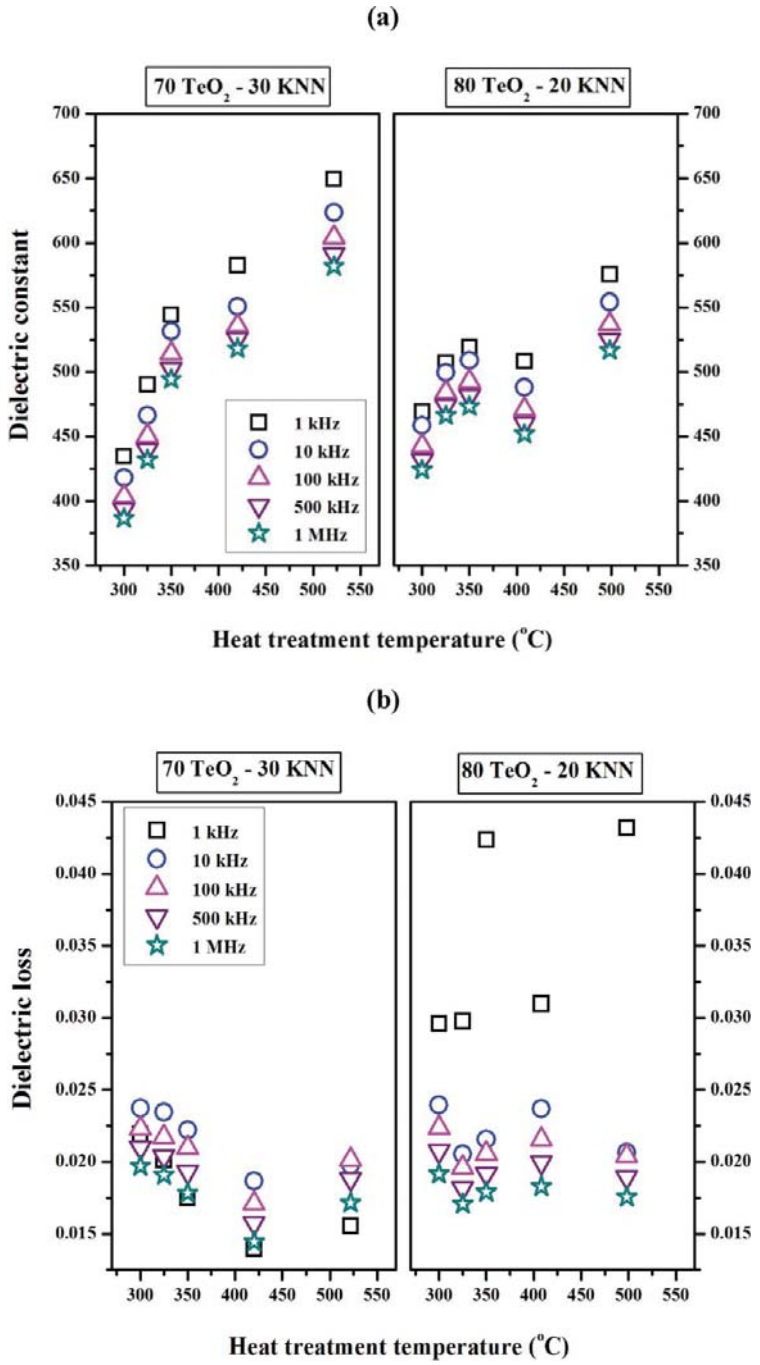

Figure 7. Dielectric constant (a) and dielectric loss (b) of two series of glass-ceramics at various HT temperatures and frequencies (Color figure available online).

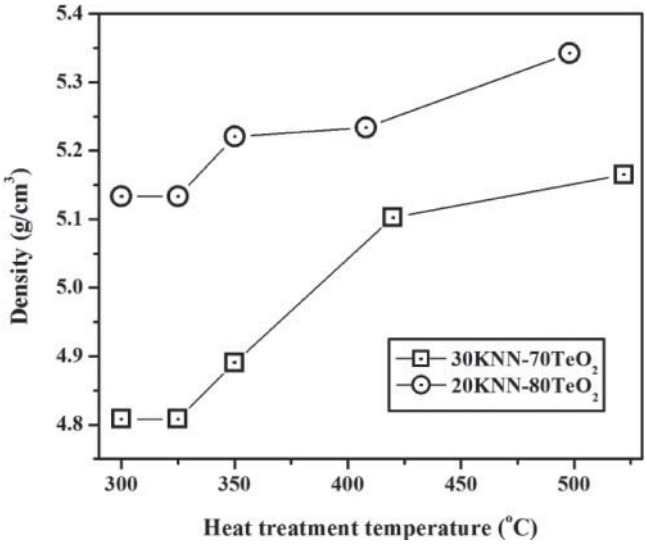

Figure 8. Density of glass and glass-ceramics versus HT temperature.

the 20KNN-80TeO_2, confirming the DTA result as mentioned before. Moreover, this also affirms the previous work done by Jeong et al. [10].

The glass-ceramics heat treated at T_{c1} and T_{c2} for each glass series are also illustrated in Fig 6. It can be seen that the 30KNN-70TeO_2 glass ceramic with HT = 420°C (T_{c1}) contained two other phases apart from the cubic (K,Na)NbO_3 phase, which may be identified as $KNbTeO_6$ (■) and TeO_2 (⊙), while that of the 20KNN-80TeO_2 glass ceramic had no trace of any other phase apart from the (K,Na)NbO_3. At T_{c2} for both glass series, the additional $Na_2Nb_4O_{11}$ (♦) phase was clearly revealed, together with two phases of $KNbTeO_6$ (■) and TeO_2 (⊙). However, the amount of $KNbTeO_6$ phase of the 30KNN-70TeO_2 (HT at T_{c2} = 522°C) was greater than that found in the 20 KNN-80TeO2 (HT at T_{c2} = 498°C).

From the full width at half maximum (FWHM) values of the most intense diffraction peak detected from XRD patterns, the average crystallite sizes (diameter, *d*) were calculated by conventional procedure using the Scherrer's equation.

$$d = \frac{0.9\lambda}{\beta \cos \theta}$$

where, λ is the wavelength of X-ray radiation (CuKα = 1.5406 A°), β is the FWHM of the reflection peak that has the maximum intensity in the diffraction pattern. The diffraction peak located at $2\theta = 28°$ (2θ = maximum intensity peak) has been considered for this estimation. The calculated average crystallite sizes are summarized in Table 2. It can be seen that the crystallite size analyzed from XRD increased with increasing heat treatment temperature. The crystallite sizes are varied after different heat treatment glasses because of the occurrence of new phases at high heat treatment temperatures.

Fig. 7 shows the dielectric properties of the heat treated glass-ceramics at various temperatures. The maximum dielectric constant was found in 30KNN-70TeO_2 glass-ceramic heat treated at T_{c2}, which was as high as 650 at 1 kHz and the dielectric loss was rather low about 0.02. It can be seen that the dielectric constant increased with increasing heat

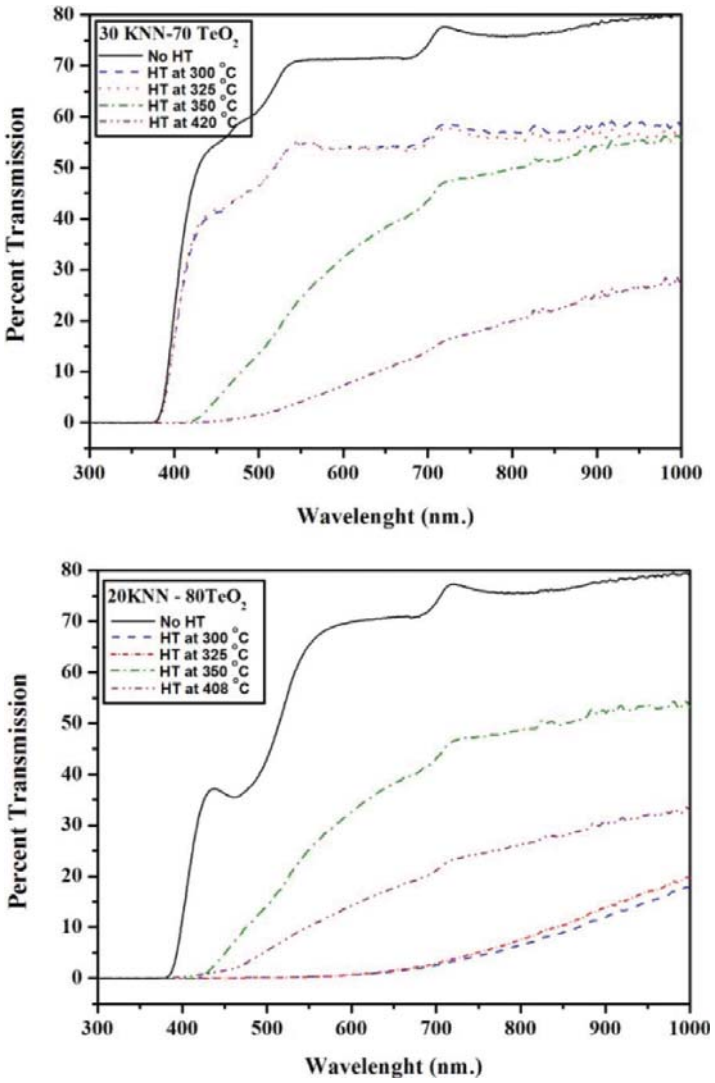

Figure 9. The percent transparent of glass-ceramic which heat treated at various temperatures.

treatment temperature. The overall dielectric values of both glass-ceramics indicate that the higher amount of KNN addition in such a series of 30KNN-70TeO_2 glass-ceramics could improve their dielectric properties.

Densities as a function of HT temperature of the prepared glass-ceramics are shown in Fig. 8. The density variation was consistent with the dielectric trend which was found to increase with increasing HT temperature. Higher values were found in the series of 20KNN-80TeO_2 glass-ceramics. This may be due to the lower value of density of KNN (4.64 g/cm^3) than that of TeO_2 (5.67 g/cm^3)

Fig. 9, shows optical transmission spectra of the quenched and heat treated samples of the 30KNN-70$TeO_2$and 20KNN-80TeO_2 glass-ceramics. All optical transmission spectra were recorded at room temperature. The percent transmission of all glass-ceramics tends

to decrease with increasing HT temperature. The low transmission in glass-ceramics of 20KNN-80TeO_2 series heat treated at 300–325°C confirms the appearance of glass-ceramics as shown in Fig. 3 and 4, having low transparency. The 30KNN-70TeO_2 and 20KNN-80TeO_2 samples heat treated at their T_{c2} are opaque. The effect of HT temperature on the transparency of glass originates from the type and size of crystals precipitated in the glass matrix. For visible light, samples possessing crystals larger than 200 nm should show light scattering and hence the respective samples should be opaque. Transparent samples should contain crystals $\ll$200 nm and also a small crystal size distribution. For 30KNN-70TeO_2 glass-ceramics, the crystal size may play an important role in the transparency of the glass-ceramics as the increase in HT temperature caused the decrease in transparency up to the HT 350°C. This is consistent with the XRD result where the crystallinity of the (K,Na)NbO_3 crystals increased with increasing HT temperature. When the HT temperature was 420°C, a secondary phase of $KNbTeO_6$ occurred and reduced the transparency of the glass ceramic greatly. For the 20KNN-80TeO_2 glass-ceramics, there is no good tendency between transparency and HT temperature. Considering their corresponding XRD patterns, only one crystal phase of cubic (K,Na)NbO_3 was observed in all glass-ceramics with HT temperature from 300°C–408°C. The highest degree of crystallinity was found in the glass-ceramic sample with HT of 408°C, while other lower HT temperature samples (300–350°C) posses similar crystallinity. It may be assumed that the crystal sizes in these 20KNN-80TeO_2 glass ceramic series may come from the inhomogeneous distribution of the cubic (K,Na)NbO_3 in the glass matrices. The corresponding SEM micrographs of these glass-ceramics are shown in Fig 10. It can be clearly seen from the micrographs that, some large crystals (bright phase) were inhomogeneously dispersed in the glass matrices.

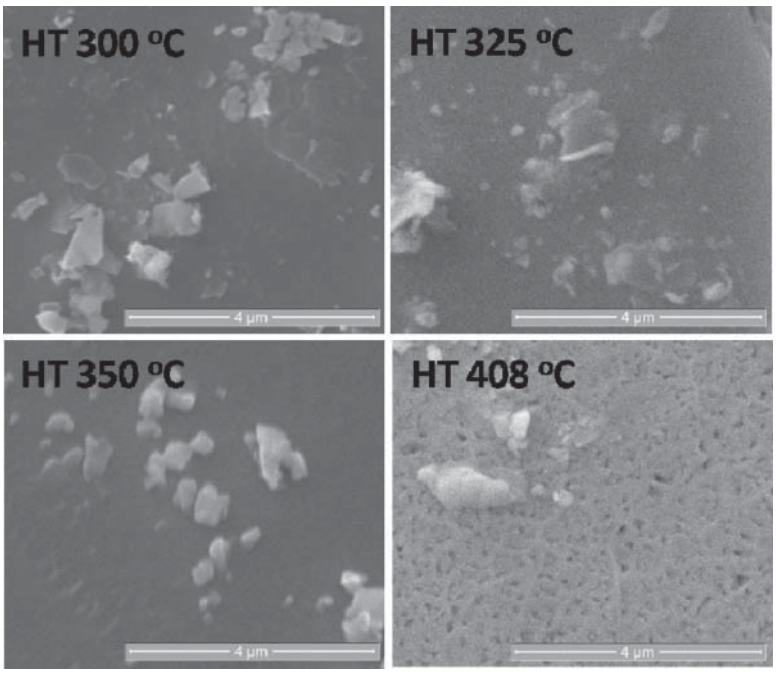

Figure 10. SEM photographs of 20KNN-80TeO_2 glass ceramic heat treated at HT of 300°C–408°C.

Table 3
Refractive indices of various heat treatment temperature glass-ceramics samples of two glass composition.

Heat treatment temperature (°C)	Refractive index of various HT glasses (at 532 nm.)
30KNN- 70TeO_2	
300	2.090
325	2.012
350	2.086
420 (T_{c1})	2.154
20KNN- 80TeO_2	
300	2.165
325	2.183
350	2.089
408 (T_{c1})	2.177

Table 3 shows the refractive indices of the heat treated glass-ceramics at various temperatures. It can be noted that the overall refractive indices of 30KNN-70TeO_2 glass-ceramics are lower than that of 20KNN-80TeO_2. This consistent with the density result, as in general the higher density of glass is, the greater refractive index is obtained.

4. Conclusion

Various materials characterization techniques were performed to study the effect of heat treatment temperature on physical, phase, dielectric and optical properties of KNN-TeO_2 glass-ceramics prepared via incorporation method. It was found that the amount of KNN in glass controlled the thermal stability of glass where a higher amount of KNN (30 mol%) promotes the stability of the glass. The XRD revealed similar crystals phase of cubic (K,Na)NbO_3 in all glass-ceramics with low HT temperature of 300°C–350°C. The glass-ceramics heat treated at T_{c1} and T_{c2} of each glass composition contained additional $Na_2Nb_4O_{11}$, $KNbTeO_6$ and TeO_2 with amount depending on the added KNN content. The crystal phases and their sizes in turn play the most important role in controlling physical, appearance, density, dielectric and optical properties of the heat treated glass-ceramics. It was found that the larger amount of KNN (30 mol%) gave improved properties of the glass-ceramic, as a glass-ceramic with high transparency, good mechanical and high dielectric constant could be obtained. Further studies should add for more understand KNN-TeO-$_2$ phenomena.

Acknowledgments

The authors would like to express their sincere gratitude to the Thailand Research Fund, National Metal and Materials Technology Center, and Faculty of Science, Chiang Mai University for financial support. We wish to thank the Graduate School Chiang Mai University and The National Research University Project under Thailand's Office of the Higher Education Commission for financial support. P. Yongsiri would like to thank the Thailand Graduate Institute of Science and Technology for her scholarship.

References

1. G. H. Hartling, Ferroelectric Ceramics: History and Technology. *J A Ceram Soc* **82**, 797–818 (1999).
2. B. Jaffe, W. R. Cook, H. Jaffe, *Piezoelectric ceramics*. Academic Press, London. JCPDS 71-2171, 1971.
3. N. F. Borrelli, M. M. Layton, Electroopic properties of transparent ferroelectric glass-ceramic system. *Trans Electron Device* **6**, 511–514 (1969).
4. L. Egerton, D. M. Dillon, Piezoelectric and dielectric properties of ceramicsin the system potassium-sodium niobate. *J Am Ceram Soc* **42**, 438–442 (1959).
5. H. Nasu, O. Matsushita, K. Kamiya, H. Kobayashi and K. Kubodera, "Third harmonic generation from Li_2O-TiO_2-TeO_2 glasses", *J Non-Cryst Solids* **124**, 275–277 (1990).
6. S. H. Kim, T. Yoko, S. Sakka, *J Am Ceram Soc* **76**, 2486–2490 (1993).
7. A. H. El-Mallawany Raouf "*Tellurite glasses handbook : physical properties and data*", CRC Press LLC, USA, 2002.
8. P. Yongsiri, S. Eitssayeam, G. Rujijanagul, S. Sirisoonthorn, T. Tunkasiri and K. Pengpat "Fabrication of transparent lead-free KNN glass-ceramics by incorporation method", *Nanoscale Research Letters* **7**, 136 (2012).
9. K. Pengpat, D. Holland, "Glass-ceramics containing ferroelectric bismuth germinate (Bi_2GeO_5)", *J. Eur. Ceram.Soc.* **23**, 1599 (2003).
10. P. Prapitpongwanich, R. Harizanova, K. Pengpatand, C. Rüssel, "Nanocrystallization of ferroelectric lithium niobate in $LiNbO_3$-SiO_2 glasses", *Materials Letters* **63**, 1027–1029 (2009).
11. P. Bomlai, P. Wichianrat, S. Muensit, S. J. Milne, "Effect of calcination and excess alkali carbonate on the phase formation and particle morphology of $K_{0.5}Na_{0.5}NbO_3$ powders", *J Am Ceram Soc* **90**, 1650–1655 (2007).
12. E. D. Jeong, M. G. Ha, H. K. Pak, B. K. Ryu, P. H. Borse, J. S. Lee, T. Komatsu, H. J. Kim, and H. G. Kim, "Thermal Stabilities, Physical and Optical Properties of K_2O-Na_2O-Nb_2O_5-TeO_2 Glasses", *J. Ind. Eng. Chem.* Vol. **12**, No. 6, 926–931 (2009).

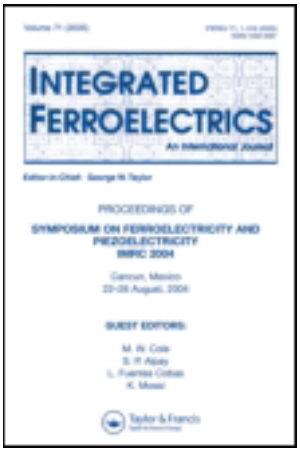

Integrated Ferroelectrics: An International Journal

Publication details, including instructions for authors and subscription information:
http://www.tandfonline.com/loi/ginf20

Effect of BCZT on Electrical Properties and Bioactivity of 45S5 Bioglass

Nuttapon Pisitpipathsin [a] , Puripat Kantha [c] , Sukum Eitsayeam [a b] , Gobwut Rujijanakul [a b] , Ruyan Guo [d] , Amar S. Bhalla [d] & Kamonpan Pengpat [a b]

[a] Department of Physics and Materials Science, Faculty of Science , Chiang Mai University , Chiang Mai , 50200 , Thailand

[b] Materials Science Research Center, Faculty of Science , Chiang Mai University , Chiang Mai , 50200 , Thailand

[c] School of Ceramic Engineering, Institute of Engineering , Suranaree University of Technology , Nakhon Ratchasima , 30000 , Thailand

[d] ECE/COE, University of Texas at San Antonio , San Antonio , TX , 78256 , USA

Published online: 30 May 2013.

To cite this article: Nuttapon Pisitpipathsin , Puripat Kantha , Sukum Eitsayeam , Gobwut Rujijanakul , Ruyan Guo , Amar S. Bhalla & Kamonpan Pengpat (2013) Effect of BCZT on Electrical Properties and Bioactivity of 45S5 Bioglass, Integrated Ferroelectrics: An International Journal, 142:1, 144-153, DOI: 10.1080/10584587.2013.780574

To link to this article: http://dx.doi.org/10.1080/10584587.2013.780574

Integrated Ferroelectrics, 142:144–153, 2013

ISSN: 1058-4587 print / 1607-8489 online
DOI: 10.1080/10584587.2013.780574

Taylor & Francis
Taylor & Francis Group

Effect of BCZT on Electrical Properties and Bioactivity of 45S5 Bioglass

NUTTAPON PISITPIPATHSIN,[1,2] PURIPAT KANTHA,[3] SUKUM EITSAYEAM,[1,2] GOBWUT RUJIJANAKUL,[1,2] RUYAN GUO,[4] AMAR S. BHALLA,[4] AND KAMONPAN PENGPAT[1,2,*]

[1]Department of Physics and Materials Science, Faculty of Science, Chiang Mai University, Chiang Mai 50200, Thailand
[2]Materials Science Research Center, Faculty of Science, Chiang Mai University, Chiang Mai 50200, Thailand
[3]School of Ceramic Engineering, Institute of Engineering, Suranaree University of Technology, Nakhon Ratchasima 30000, Thailand
[4]ECE/COE, University of Texas at San Antonio, San Antonio TX 78256, USA

In this work, ferroelectric $Ba_{0.92}Ca_{0.08}Zr_{0.05}Ti_{0.95}O_3$/45S5 bioglass composite or (BCZT/45S5 composite) has been produced for orthopedic applications. The BCZT concentrations ranged from 0–15 wt.%. The BCZT/45S5 composite was prepared by conventional melting method at 1300°C for 1 h following by heat treatment schedule at the crystallization temperatures of glass. The effects of BCZT addition on the dielectric and piezoelectric properties and the biocompatibility of BCZT/45S5 composites were investigated. It was found that, the addition of BCZT improved the hardness and dielectric properties of materials, which may be caused by the presence of the BCZT. Moreover, the bioactivity of the 45S5 bioglass was improved with addition of BCZT phase as evident by the formation of bone like apatite layers on the surface of all BCZT/45S5 composites after soaking in simulated body fluid (SBF).

Keywords 45S5 Bioglass; Barium Calcium Zirconium Titanate; Ferroelectric; Piezoelectric

1. Introduction

Due to the disadvantages related with bone grafting and bone replacement procedures using autograft and allograft, the development of synthetic bone replacement materials has continuously augmented. The materials, having biomechanical properties matching that of bone and sufficient bioactivity to form a bond with living bone and soft tissues, are of particular interest in the biomaterials field [1].

45S5 bioglass is a commercially available inorganic material which has been used as bone replacement for more than 20 years. This bioactive glass was firstly developed by Hench *et al.* in 1969 [2]. The chemical composition of this bioglass composites of 45 wt.% SiO_2, 24.5 wt.% Na_2O, 24.5 wt.% CaO and 6 wt.% P_2O_5. The bioactivity of this glass resulted from the formation of a hydroxycarbonate apatite (HCAp) layer on its surface.

Received June 30, 2012; in final form October 24, 2012.
*Corresponding author. E-mail: kamonpan.p@cmu.ac.th

This layer is chemically similar to the mineral part of bone. The rate of HCAp formation has a significant effect on the tissue bonding rate, following a sequence of reactions between the implanted material and the physiologic fluids and surrounding tissue [3].

Many researchers have found the improvement in osteobonding and bone growth on the surface of polarized hydroxy apatite (HA) due to the generation of a permanent surface charge on the materials in *vitro*. Nagamura *et al.* [4] found that apatite crystal growth on HA was accelerated by the negatively charged surface. Moreover, it is known that bone displays intrinsic piezoelectric behavior and possesses a charge under the application of a mechanical stress. It has been hypothesized that stress-induced potentials in bone affect the activity of osseous formation [5].

Ferroelectric materials have attracted some interest in medical applications. Feng *et al.* prepared HA-$BaTiO_3$ composites with piezoelectric coefficient (d_{33}) of 6 pC/N, which promoted osteogenesis in the jaw bones of dogs [6]. N. Pisitpipathsin *et al.* studied HA-$BaZr_{0.05}Ti_{0.95}O_3$ composites, and found that the bioactivity of the HA composites was improved with 10 wt.% $BaZr_{0.05}Ti_{0.95}O_3$ after soaking in simulated body fluid (SBF) for 15 days [7].

In this work, the fabrication of BCZT/45S5 composites with the amount of BCZT being 0, 5, 10 and 15 wt.%, was carried out in order to study phase evolution and the mechanical and electrical properties and bioactivity of BCZT/45S5 composites. The selected $Ba_{0.92}Ca_{0.08}Zr_{0.05}Ti_{0.95}O_3$ (BCZT) phase has a high piezoelectric coefficient (d_{33}) of about 365 pC/N [8].

2. Experimental

2.1 Materials Preparation

The BCZT/45S5 composites with $Ba_{0.92}Ca_{0.08}Zr_{0.05}Ti_{0.95}O_3$ (BCZT) concentrations 0, 5, 10 and 15 wt.% were prepared by melt-quenching method. The mixed powders of these compositions were prepared from reagent grade Na_2CO_3, CaO, $NH_4H_2PO_4$, SiO_2 and $Ba_{0.92}Ca_{0.08}Zr_{0.05}Ti_{0.95}O_3$ powders. The powders were mixed and melted in Pt crucibles for 1 h at 1300°C. Each melt was quenched between stainless steel plates at room temperature. The thermal properties of the selected samples were investigated using difference thermal analysis (DTA). The resulting glasses were subjected to heat treatment schedules for crystallization at temperature of 750°C with heating/cooling rates of 5/10°C/min, respectively and with 4 h dwell time.

2.2 Materials Characterization

X-ray diffraction (XRD: Siemen D-500) technique was employed to investigate the phase composition in the prepared BCZT/45S5 bioglass composites. Well-polished surfaces were subjected to Vickers indentation (Galileo Microscan, LTF S.p.a., Antegnate, Italy) for hardness (Hv) determination. The room temperature dielectric constant (ε_r) and loss ($\tan\delta$) of BCZT/45S5 bioglasses was measured using LCZ meter (Model 4276A, Hewlett Packard) at 100 Hz to 2 MHz. The dielectric constant was calculated from the capacitance by the following equation [9]:

$$\varepsilon_r = \frac{Cd}{\varepsilon_0 A} \tag{1}$$

where C is the capacitance (farads), ε_0 is the free space dielectric constant value (8.854×10^{-12} Fm^{-1}), A is the capacitor area (m^2) and d is the thickness (m) of the BCZT/45S5 composites. In vitro test was carried out by soaking in SBF. The SBF was buffered at pH 7.4 and maintained at 37°C in order to simulate near physiological condition for 7 days. After that, the formation of apatite layers was investigated by using scanning electron microscope (SEM Model JEOL JSM-5910LV). The piezoelectric properties were measured at room temperature by using a piezoelectric-d_{33}-meter (S5865 d_{33} METER).

3. Result and Discussions

In this study, the heat treatment temperature (750°C) was determined from thermal parameters, such as, glass transition temperature (T_g) and crystallization temperature (T_c), measured from the DTA trace of the 45S5 bioglass (0 wt.% BCZT) as shown in Figure 1. From the trace, two exothermic peaks at 759°C and 916°C were observed, which corresponds to two crystallization temperatures T_{C1} and T_{C2}, respectively. The softening temperature (T_S) was found at 689°C while two glass transition (T_g) temperatures observed in the DTA trace were calculated to be at 560°C (T_{g1}) and 844 (T_{g2}).

Consequently, the heat treatment temperature of 750°C as mentioned earlier, was chosen between T_s (689°C) and T_{c1} (759°C) of the 45S5 bioglass (0 wt.% BCZT), to avoid the crystallization peak of T_{c1} (759°C), which also applied to other higher BCZT content samples. Generally at the peak of T_c, the crystallization occurs at the highest rate, leading to a high migration rate of atoms or molecules. Thus, a porous body of the BCZT/45S5 composites may be obtained after the chosen heat treatment process.

The increasing trend of density data of the BCZT/45S5 composites with increasing BCZT content is illustrated in Figure 2. However, the SEM micrographs of the BCZT/45S5 composites (Fig. 3.), show interesting result as the highest porosity sample was obtained

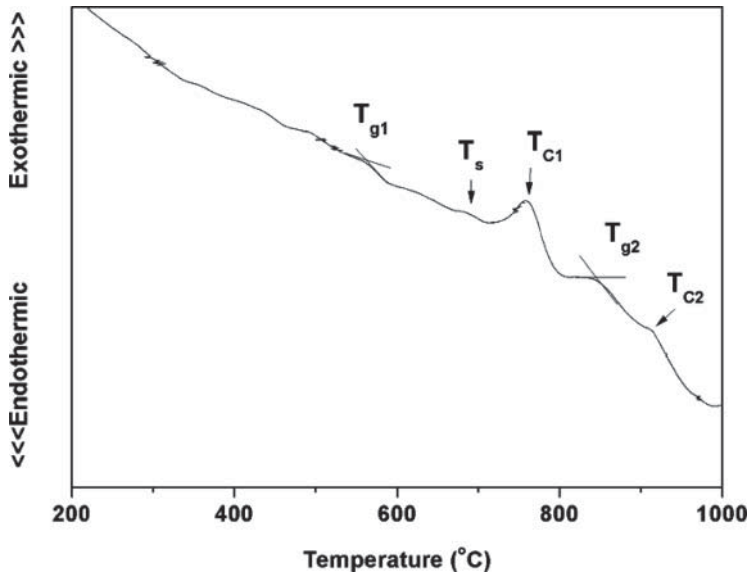

Figure 1. DTA trace of 45S5 bioglass.

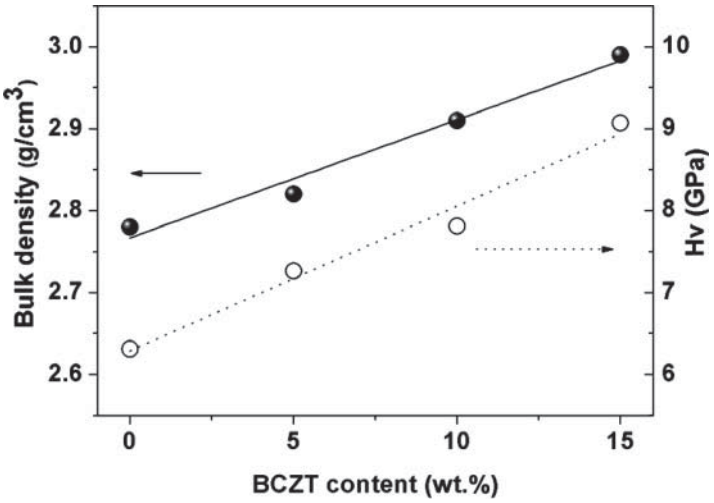

Figure 2. The density and Vicker hardness value of the BCZT/45S5 composites for various BCZT contents.

from the highest BCZT content sample (15 wt.%). This may result from the higher density of BCZT (∼5.70 g/cm^3) than compound with of 45S5 bioglass (∼2.78 g/cm^3).

The linearly increasing trend of hardness (Hv) versus BCZT content, similar to the density trend, was also obtained as illustrated in Figure 2. This is believed to be contributed

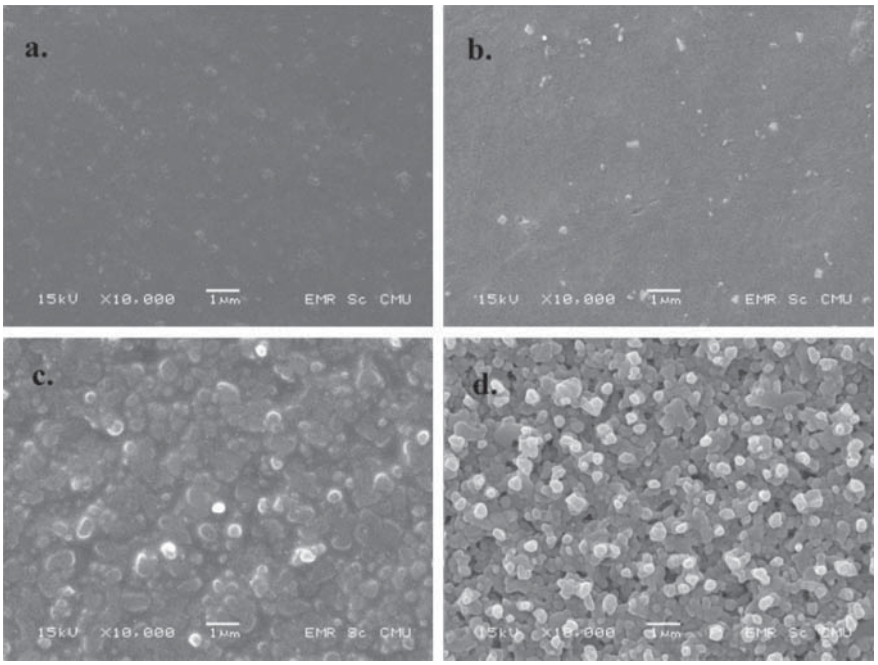

Figure 3. SEM micrographs of the BCZT/45S5 composites; (a.) 0 wt.% of BCZT, (b.) 5 wt.% of BCZT, (c.)10 wt.% of BCZT, (d.)15 wt.% of BCZT.

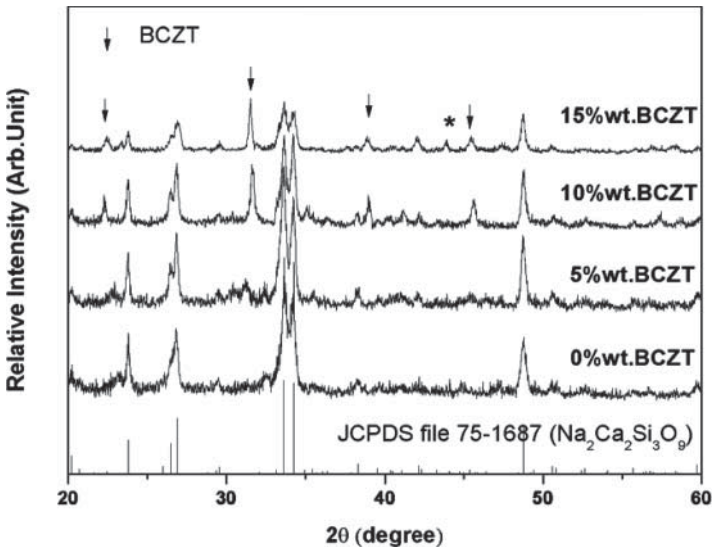

Figure 4. XRD patterns of BCZT/45S5 composites for 2θ between 20° and 60°.

by the occurrence of grains in these composites. Grain boundaries are known as stress concentration sites, which acted as effective obstacles to dislocation pile-up in the adjacent grains, leading to harder materials [10]. This was the reason that the highest BCZT content sample (15 wt.%), has the smallest grain size, possessed the highest hardness value compared to those with larger grain or no grain boundary as in the lower BCZT content samples (0–10 wt.%). As can be seen in Fig. 3, the higher grain boundary was obtained from the higher BCZT content samples.

The XRD profiles of heat treatment BCZT/45S5 composites for 2θ between 20° and 60° are presented in Figure 4. The main diffraction peaks of all ceramics corresponded to the crystal structure of the sodium calcium silicate ($Na_2Ca_2Si_3O_9$) (JCPDS0075-1687). The BCZT peaks are clearly observed for the high BCZT content samples of 10 and 15 wt.%. The relative intensity of the $Na_2Ca_2Si_3O_9$ phase was found to decrease with increasing BCZT content. This may be due to the decomposition of $Na_2Ca_2Si_3O_9$ to from a trace of unknown secondary phase (*), at the high BCZT content of 15 wt.% samples.

The frequency dependence of the relative permittivity (ε_r) is presented in Figure 5. Results indicated that all BCZT/45S5 samples showed a degree of dielectric dispersion at low frequency ($f < 1$ kHz). The permittivity magnitude and degree of dispersion increased with increasing BCZT content, which may be caused by the presence of the added ferroelectric BCZT phase [11]. The dispersions of the BCZT/45S5 composites may result from the dipole moment of ions and the presence of some dc conductivity in these materials [12, 13]. The dielectric loss ($\tan\delta$) of the BCZT/45S5 composites is presented in the inset of Figure 5. It can be seen that the $\tan\delta$ values of the BCZT/45S5 composites were between 0.1–0.4 at 1 kHz.

The ac conductivity (σ) of the BCZT/45S5 composites was investigated at different frequencies as shown in Figure 6. The ac electrical conductivity of the BCZT/45S5 samples was calculated from the following equation [14]:

$$\sigma_{ac} = \omega\varepsilon_0\varepsilon_r \tan\delta \tag{2}$$

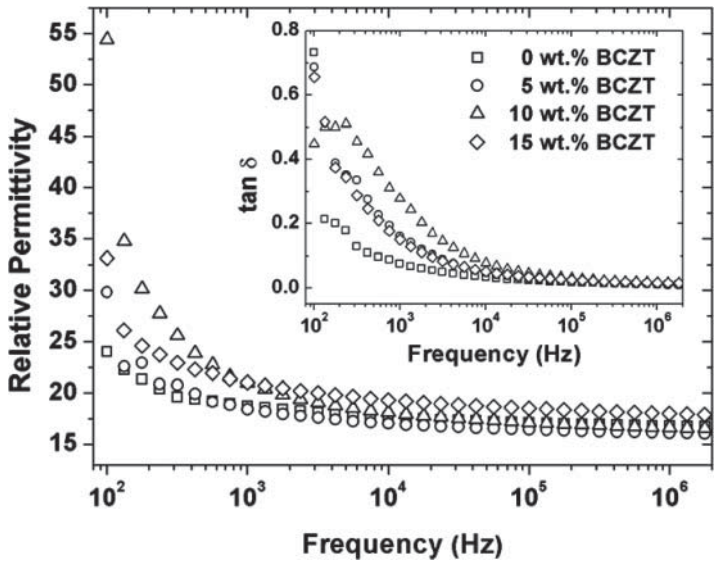

Figure 5. The frequency dependence of relative permittivity and dielectric loss (tanδ) of BCZT/45S5 composites.

where ε_o is the vacuum dielectric permittivity and ω is the angular frequency ($2\pi f$). At low frequency (<0.3 kHz), the conductivity showed insignificant changes with varying in frequency. However, at higher frequencies (>0.3 kHz) the conductivity increased almost linearly with frequency (f) following the universal power law behavior [15] such that $\sigma\ (\omega)\ \alpha\omega^n$ where n is $0.58 < n < 0.70$. Moreover, the ac conductivity at a particular frequency increased with increasing BCZT content. It can be assumed that all BCZT/45S5

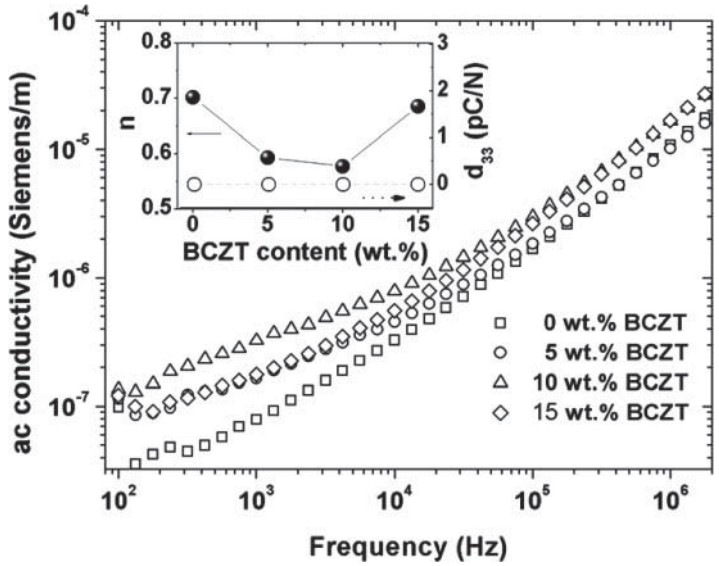

Figure 6. The frequency dependence of ac conductivity of BCZT/45S5 composites.

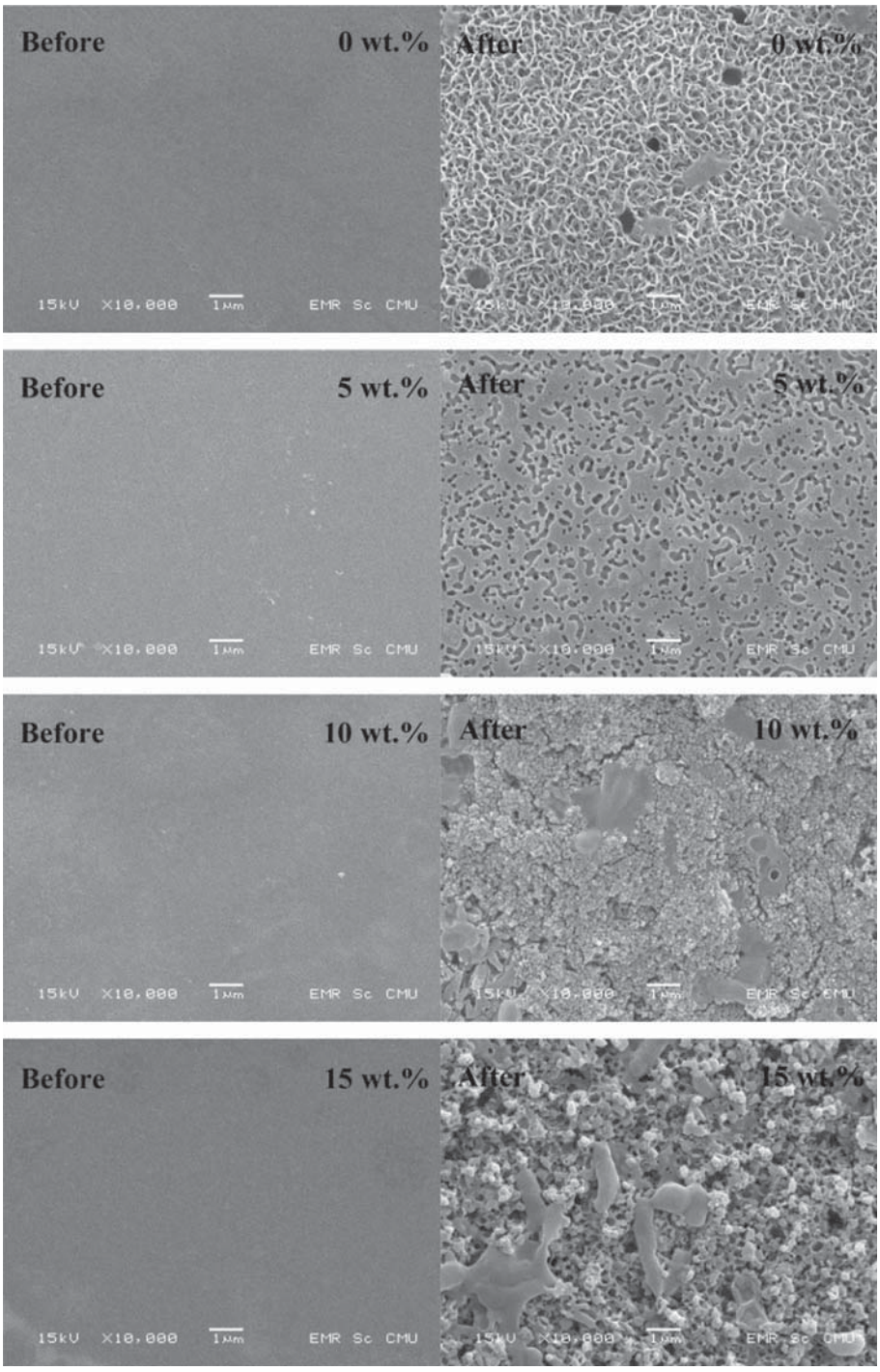

Figure 7. SEM micrographs of the BCZT/45S5 composites before and after 7 days in SBF.

composites exhibited the ac conductivity of the insulating phases [13], as $\omega\varepsilon_0\varepsilon_0$, contributes to the conductivity in the power law region.

The variation of the piezoelectric coefficient (d_{33}) as the function of BCZT content is plotted in the inset of Figure 6. All BCZT/45S5 composites exhibited no piezoelectric effect ($d_{33} = 0$ pC/N). In polymer-piezoelectric composites the polymer can mechanically possess the piezoelectric and prevent it from developing a strain during the poling process. This can lead to mechanical depolarization and loss of piezoelectric properties of composites [16]. For the case of these BCZT/45S5 composites the volume fraction of the glass matrices is much longer than that of the BCZT phase, leading to overall zero value of d_{33}. Thus, in order to improve the piezoelectric properties of these materials, a higher amount of BCZT phase of $>$20 wt.% should be considered.

SEM micrographs of the BCZT/45S5 composites for various BCZT contents before and after incubating in SBF for 7 days are presented in Figure 7. Apatite formation was observed on the surface for all samples. However, the morphology of the formed apatite layers varied with the different BCZT content in the composites. After incubation for 7 days, the surface of 0 wt.% BCZT sample was fully covered by one apatite layer, and this layer was composed of fiber-like apatite. For the sample containing 5 wt.% BCZT, the newly formed apatite layer was slightly compact. However, for the 10 wt.% BCZT samples, the surface was composed of two different zones of numerous small spherical particles and was a compact layer. Also for the 15 wt.% BCZT samples, different morphologies of the apatite layers were clearly observed. Furthermore, for the 0 and 15 wt.% of BCZT sample surfaces many pores were observed after soaking in SBF, which may be due to the dissolution of crystal phase during soaking in SBF [17]. Apatite formation upon the surface of BCZT/45S5 composites when in contact with physiologic fluids is speculated to progress by the following mechanism. The BCZT/45S5 composites release Na^+ and Ca^{2+}ions from the glass which exchange with the H^+ and H_3O^+ ions from SBF to form hydrated silica (Si–OH) groups on the glass surface. Apatite nucleation was induced by the Si–OH groups through the formation of calcium phosphate and amorphous calcium

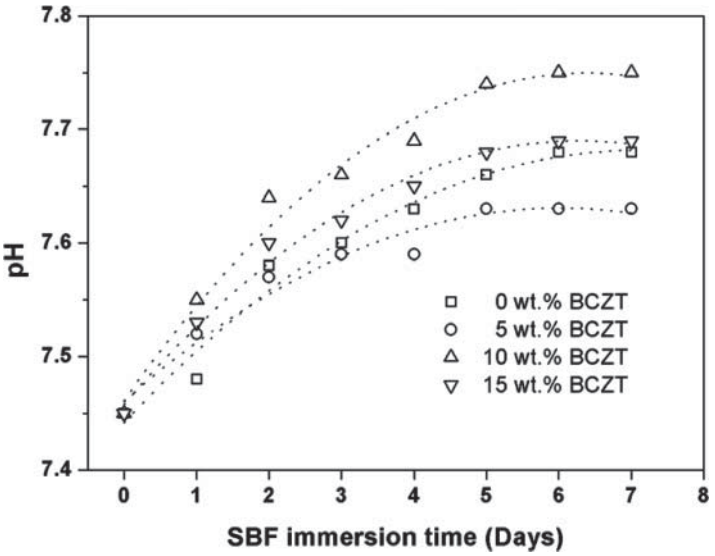

Figure 8. The pH as a function of immersion time in SBF for BCZT/45S5 composites.

silicate. Once nucleated, the apatite can grow spontaneously as the SBF fluid is highly supersaturated under normal condition. The Na^+ and Ca^{2+} ions released from the surface of the composite also accelerate apatite nucleation by increasing the ionic activity product of apatite in the SBF fluid. The dissolution of BCZT/45S5 composite is dependent on Na^+ and Ca^{2+} within it [18, 19].

The pH as a function of BCZT/45S5 composites immersion time in the SBF medium during 7 days is shown in Figure 8. Ions were leached out from the composites, and then exchanged with H^+ and H_3O^+ ions from the SBF solution. It was apparent that the pH of the SBF solution increased by the dissolution [20]. The dissolution rate as well as pH increment decreased after about 5 days due to the decrease of Na^+ and Ca^{2+} ionic concentration in surface. The BCZT/45S5 composite samples with high BCZT content of more than 10 wt.% possessed the highest rate of dissolution. This may affect the formation of the apatite layer, especially their morphologies as can be seen in the corresponding SEM micrographs in Fig 6.

4. Conclusions

Bioactive ferroelectric $Ba_{0.92}Ca_{0.08}Zr_{0.05}Ti_{0.95}O_3$/45S5 composites (BCZT/45S5 composites) for orthopedic applications were successfully formed by conventional melt quenching and heat treatment techniques. The addition of BCZT improved the Vickers hardness and dielectric property of materials, which may be attributed to the presence of the ferroelectric phase. The frequency dependence of ac conductivity and permittivity trends of all composites are typical of insulating component materials. Moreover, the bioactivity of a 45S5 composite was improved with addition of BCZT content as evident by the formation of bone like apatite layers on the surface of all BCZT/45S5 composites after soaking in simulated body fluid (SBF).

Acknowledgments

The authors would like to thank the Thailand Research Fund (TRF), the National Research University Project under Thailand's Office of the Higher Education Commission, the Royal Golden Jubilee Ph.D. Program, the Graduate School Chiang Mai University and Faculty of Science, Chiang Mai University, Thailand for financial support. Also the UTSA acknowledges the support of NSF/INAMM GRANT #0844081.

References

1. O. Peitl, E. D. Zanotto, F. C. Serbena, and L. L. Hench, Compositional and microstructural design of highly bioactive P_2O_5-Na_2O-CaO-SiO_2 glass-ceramics. *Acta Biomaterialia*, **8**, 321–332 (2012).
2. O. Bretcanu, X. Chatzistavrou, K. Paraskevopoulos, R. Conradt, I Thompson, and A. R. Boccaccini, Sintering and crystallisation of 45S5 bioglass powder. *Journal of the European Ceramic Socity*, **29**, 3299–3306 (2009).
3. L. Lefebvre, J. Chevalier, L. Gremillard, R. Zenati, G. Thollet, D. Bernache-Assolant, and A. Govin, Structural tranformations of bioactive glass 45S5 with thermal treatments. *Acta Materialia*, **55**, 3305–3313 (2007).
4. S. Nakamura, T. Kobayashi, and K. Yamachita, Enhanced osteobonding by negative surface charges of electrically polarized hydroxyapatite. *Journal of Biomedical Materials Research*, **57**, 477–484 (2001).

5. N. C. Teng, S. Nakamura, Y. Takagi, Y. Yamachita, M. Ohgaki, and K. Yamachita, A new approach to enhancement of bone formation by electrically polarized hydroxyapatite. *Journal of Dental Research*, **80**,1925–1929 (2001).
6. J. Q. Feng, H. P. Yuan, and X. D. Zhang, Promotion of oteogenesis by a piezoelectric biological ceramics. *Biomaterials*, **18**, 1531–1534 (1997).
7. N. Pisitpipathsin, P. Kantha, W. Leenakul, P. Sriprapha, K. Pengpat, S. Eitssayeam, and G. Rujijanagul, Effect of $BaZr_{0.05}Ti_{0.95}O_3$ addition on microstructure and piezoelectric properties of hydroxyapatite bone. *Advanced Materials Research*, **506**, 166–169 (2012).
8. W. Li, Z. Xu, R. Chu, P. Fu, and G. Zang, Piezoelectric and dielectric properties of $(Ba_{1-x}Ca_x)(Ti_{0.95}Zr_{0.05})O_3$ lead-free ceramics. *Journal of the American Ceramic Society*, **93**(10), 2942–2944 (2010).
9. C. Fu, H. Chen, X. Deng, W. Cai, L. Zhou, and Z. Liu, Microstructure and ferroelectric properties of $BaZr_{0.2}Ti_{0.8}O_3$ films prepared by sol-gel. *Integrated Ferroelectrics*, **107**, 24–30 (2009).
10. M. Promsawat, A. Watcharapasorn, and S. Jiansirisomboon, Effects of ZnO nanoparticulate addition on the properties of PMNT ceramics. *Nanoscale Research Letters*, **7:65**, 1–7 (2012).
11. N. Pisitpipathsin, P. Kantha, U. Inthata, S. Eitssayeam, G. Rujijanagul, D. Holland, and K. Pengpat, The Influence of Heat Treatment Condition on Electrical Properties of Glass-Ceramics Containing Ferroelectric Lead Bismuth Germanate ($(Pb_3Bi_2(GeO_4)_3)$. *Ferroelectrics*, **416**, 151–157 (2011).
12. B. Harihara, B. Venkataraman, and K. B. R. Varma, Frequency-dependent dielectric characteristics of ferroelectric $SrBi_2Nb_2O_9$ ceramics. *Solid StateIonics*, **167**, 197–202 (2004).
13. D. P. Almond, C. R. Bowen, and D. A.S. Rees, Composite dielectrics and conductors: simulation, characterization and design. *Journalof Physic D: Applied Physics*, **39**, 1295–1304 (2006).
14. A. Prasad, A. Basu, and M. Mahata, Impedance and conductivity analysis of Li_2SiO_3 ceramic. *Chalcogenide Letters*, **8**(8), 505–510 (2012).
15. A. K. Jonscher, The 'universal' dielectric response. *Nature*, **267**, 673–679 (1977).
16. T. Hauke, R. Steinhausen, W. Seifert, H. Beige, and M. Kamlah, Modeling of poling behavior of ferroelectric 1–3 composites. *Journal of Applied Physics*, **89**(9), 5040–5047 (2001).
17. J. Ma, C. Z. Chen, D. G. Wang, X. G. Meng, and J. Z. Shi, Influence of the sintering temperature on the structural feature and bioactivity of sol-gel derived SiO_2-CaO-P_2O_5 bioglass. *Ceramics International*, **36**, 1911–1916 (2010).
18. M. G. Cerruti, D. Greenspan, and K. Powers, An analytical model for the dissolution of different particle size samples of Bioglass ((R)) in TRIS-buffered solution. *Biomaterials*, **26**(24), 4903–4911 (2005).
19. D. A. Cortés, A. Medina, J. C. Escobedo, S. Escobedo, and M. A. López, " Effect of wollastonite ceramics and bioactive glass on the formation of a bonelike apatite layer on a cobalt base alloy, *Journal of Biomedical Materials Researchpart A*, **70**, 341–346 (2004).
20. J. P. Nayak, S. Kumar, and J. Bera, Sol-gel synthesis of bioglass-ceramics using rice husk as source for silica and its characterization. *Journal of Non-Crystalline Solids*, **356**, 1447–1451 (2010).

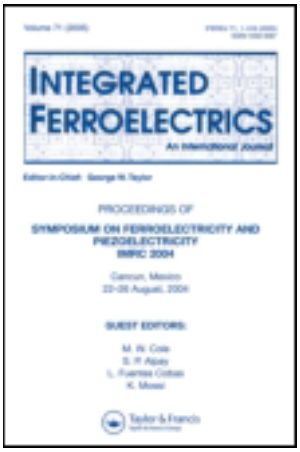

Integrated Ferroelectrics: An International Journal

Publication details, including instructions for authors and subscription information:
http://www.tandfonline.com/loi/ginf20

Effect of Camphor Addition on Mechanical Properties and Bioactivity of P_2O_5-CaO-Na_2O Bioactive Glass

Sutatip Thonglem [a] , Gobwute Rujijanagul [a b] , Sukum Eitssayeam [a b] , Tawee Tunkasiri [b] & Kamonpan Pengpat [a b]

[a] Department of Physics and Materials Science, Faculty of Science , Chiang Mai University , Chiang Mai , 50200 , Thailand

[b] Materials Science Research Center, Faculty of Science , Chiang Mai University , Chiang Mai , 50200 , Thailand

Published online: 30 May 2013.

To cite this article: Sutatip Thonglem , Gobwute Rujijanagul , Sukum Eitssayeam , Tawee Tunkasiri & Kamonpan Pengpat (2013) Effect of Camphor Addition on Mechanical Properties and Bioactivity of P_2O_5-CaO-Na_2O Bioactive Glass, Integrated Ferroelectrics: An International Journal, 142:1, 135-143, DOI: 10.1080/10584587.2013.780550

To link to this article: http://dx.doi.org/10.1080/10584587.2013.780550

Integrated Ferroelectrics, 142:135–143, 2013

ISSN: 1058-4587 print / 1607-8489 online
DOI: 10.1080/10584587.2013.780550

Taylor & Francis
Taylor & Francis Group

Effect of Camphor Addition on Mechanical Properties and Bioactivity of P_2O_5-CaO-Na_2O Bioactive Glass

SUTATIP THONGLEM,[1] GOBWUTE RUJIJANAGUL,[1,2] SUKUM EITSSAYEAM,[1,2] TAWEE TUNKASIRI,[2] AND KAMONPAN PENGPAT[1,2,*]

[1]Department of Physics and Materials Science, Faculty of Science, Chiang Mai University, Chiang Mai 50200, Thailand
[2]Materials Science Research Center, Faculty of Science, Chiang Mai University, Chiang Mai 50200, Thailand

In this work, we have studied the effects of camphor addition on the properties of porous ceramics of P_2O_5-CaO-Na_2O glass for biomedical applications. Mixed powders were formed into pellets and subsequently sintered at the temperatures ranging between 550 and 650°C. The sintered ceramics were investigated in terms of pore characteristics, phase formation, and in vitro bioactivity. The pore sizes of the structures were observed by SEM to be in the range of 150–400 μm. XRD results revealed that calcium phosphate and sodium phosphate phases were formed in the porous ceramics. In vitro bioactivity was assessed in SBF solution and the results confirm the formation of apatite like cells on the surface of all glass ceramic compositions.

Keywords P_2O_5-CaO-Na_2O glass; Porous ceramics; Calcium phosphate

1. Introduction

Bioactive ceramics such as hydroxyapatite, β-tricalcium phosphate, silicate based glass and phosphate based glass have been of much interest for biomedical applications [1–7], particularly, phosphate based glass, as it has greater osteoblastic activity comparing to hydroxyapatite [8, 9]. P_2O_5-CaO-Na_2O glass is one of the bioactive phosphate based glasses, which has already played a vital role in areas of clinical medicine [9–13].

P_2O_5-CaO-Na_2O glasses were found to exhibit low thermal parameters (glass transition temperature (T_g), crystallization temperature (T_x) and melting point (T_m)), depending on the amount of CaO content in glass composition [9–12]. CaO also has a strong effect in reducing the CaO dissolution rate in distilled water and simulated body fluid [SBF]. The thermal parameters increased and dissolution rate decreased with increasing CaO content as the network of cross-linked PO_4^{3-} groups with Ca^{2+} are stronger than that of the chain structure of PO_4^{3-} groups with Na^+ [9, 13]. The suitable composition of this glass system was found for samples where the amount of P_2O_5 was more than 40 mol% especially for the 45 mol% sample which also possessed good biocompatibility [9, 10]. Phosphate phases

Received June 30, 2012; in final form October 15, 2012.
*Corresponding author. E-mail: kamonpan.p@cmu.ac.th

which are essential in controlling biocompatibility can be formed in this P_2O_5-CaO-Na_2O glass system [11].

Porosity also plays an important role in bone substitute applications for bone tissue regeneration, cell increment and drug delivery. Dimension, morphology and distribution of pores are important factors to control bone tissue regeneration and a pore size range of 100–400 μm has been accepted as a suitable condition for cell in growth. Moreover, interconnectivity of pores in substitute bone is equally important for bone tissue regeneration, which allows penetration of the osteoblast-like cells [14, 15]. Porous structure was formed by including volatile materials which are burnt out during sintering. The volatile materials used were organic compounds such as paraffin, naphthalene, carbon, starch, flour, hydrogen peroxide and polymers. The pores characteristics (fraction, size, morphology and distribution) were controlled by the type, amount and properties of the volatile materials and the evaporation and sublimation mechanisms of the volatile materials during the burn out process [14, 15]. In addition, Ramay and Zhang [16] prepared porous hydroxyapatite scaffolds by a combination of gel-casting and polymer sponge methods. Their results showed that the scaffolds prepared have an open, uniform and interconnected porous structure with a pore size range of 200–400 μm. Due to the low sintering temperatures of P_2O_5-CaO-Na_2O glass production, low boiling point volatile materials should be considered.

In this study, camphor ($C_{10}H_{16}O$) was chosen as a suitable volatile material for forming P_2O_5-CaO-Na_2O porous ceramics because the evaporation process of camphor can be completed at its boiling point as low as 204°C (Materials Safety Data Sheets: (MSDS)). The influence of camphor addition on the porosity of the prepared ceramics with various compositions of P_2O_5-CaO-Na_2O glasses and a comparison of their properties with that of natural bone were reported.

2. Experimental

2.1 Glass Preparation

Three glasses were prepared from $(NH_4)_2HPO_4$, $CaCO_3$ and Na_2CO_3 with nominal compositions as shown in Table 1. The precursors were weighed and melted in an alumina crucible at 1200°C for 1 hour in an electric furnace. The homogeneous melts were quenched to room temperature onto a stainless steel mold and the quenched melts was subsequently pressed by another stainless steel plate to avoid crystallization. An automatic milling machine was employed for grinding the prepared glasses into a fine glass powder of about 2 μm in size.

Table 1
Nominal glass compositions, thermal parameters and sample codes used.

	Content (mol%)			Thermal Parameter (°C) [17]		
Code	P_2O_5	CaO	Na_2O	T_g	T_{x1}	T_{x2}
$P_{45}C_{32}N_{23}$	45	32	23	440	578	—
$P_{45}C_{36}N_{19}$	45	36	19	446	564	593
$P_{45}C_{40}N_{15}$	45	40	15	455	606	625

2.2 Preparation of Porous Ceramics Using Camphor

The three glass powders (70 wt%) were mixed with camphor (30 wt%) and the batches were pressed into pellets. The pellets were sintered in an electric furnace using a 3-stage schedule, including heating from room temperature to 204°C (boiling point of camphor) with heating rate of 5°C/min for 1 h (to burn off the camphor), afterward heating to the sintering temperature with heating rate of 5°C/min for 2 h, and finally cooling down to room temperature at a cooling rate of 5°C/min. Sintering temperatures, ranging between 550 to 650°C were employed as they are in the range of the crystallization temperatures of this P_2O_5-CaO-Na_2O glass system as show in Table 1 [17].

2.3 Characterization of the Porous Ceramics

The density and apparent porosity analysis of the porous ceramics were measured at room temperature via ASTM C20-00 (2010) Standard test methods. The shape and size of pores were investigated by scanning electron microscopy (SEM: JSM-6335F). Strength was measured using a universal testing machine (Instron model 55R4502) in compressive stress mode.The crystal structures of the porous ceramics were identified by X-ray diffraction (XRD: Bruker AXS D8 ADVANCE) and energy dispersive X-ray spectroscopy (EDX). Microstructures of the prepared ceramics were investigated by scanning electron microscopy (SEM: JSM-6335F).

2.4 In Vitro Bioactivity

Simulated body fluid (SBF) is an acellular solution with ion concentration similar to those of blood plasma, in order to reproduce formation of apatite on bioactive materials *in vitro* [18]. The SBF was prepared by dissolving reagent-grade chemicals in deionized water. The reagent-grade chemicals consisted of sodium chloride (NaCl), sodium hydrogen carbonate ($NaHCO_3$), potassium chloride (KCl), di-potassium hydrogen phosphate trihydrate ($K_2HPO_4 \cdot 3H_2O$), magnesium chloride hexahydrate ($MgCl_2 \cdot 6H_2O$), calcium chloride ($CaCl_2$) and sodium sulfate (Na_2SO_4). The solution was buffered to pH standards with Tris-hydroxymethylaminomethane ($(HOCH_2)_3CNH_2$)(Tris)) and hydrochloric acid (HCl) [19]. In vitro studies showed that when hydroxyapatite [20], silicate-based glass [6, 21] and phosphate-based glass [22–23] were immersed in SBF, apatite formation could be reproduced on their surfaces. These apatite layers are chemically and structurally equivalent to the mineral phase in bone.

In this study, the samples were immersed separately in solutions of SBF under a static regime [24] and stored with constant volume in the incubation apparatus for 7 days at a temperature of 37°C. After being immersed, the ceramics were rinsed with deionized water and dried in desiccators at room temperature [21]. The ceramics were then analyzed using SEM and energy dispersive spectroscopy (EDX) to investigate apatite formation.

3. Results and discussion

3.1 Phase Formation

The XRD patterns of all porous ceramics after sintering are shown in Fig. 1. The crystalline phase precipitated in sintered ceramics could be clearly assigned to four phases comprising two calcium phosphate phases and two sodium phosphate phases (with the same composition). The calcium phosphate phases were $Ca_2P_2O_7$ (JCPDS file no. 73-0440) and

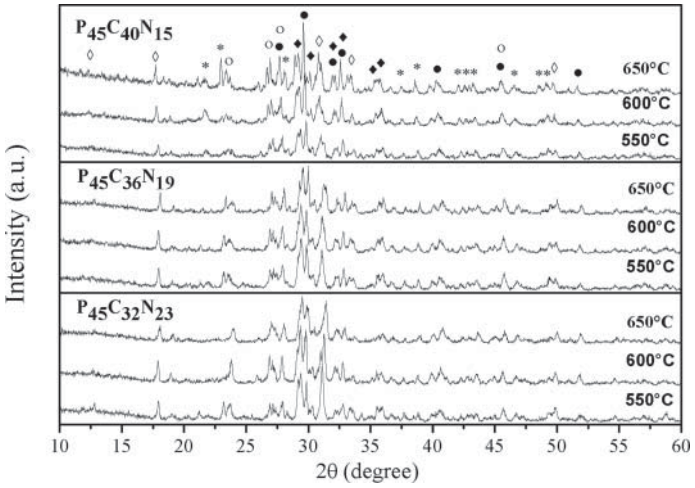

Figure 1. XRD patterns of all ceramics and of β-$Ca_2P_2O_7$ phase file no. 03-0604 (●), $Ca_2P_2O_7$ phase file no. 73-0440 (○), $NaPO_3$ phase file no. 76-0788 (⧫), $NaPO_3$ phase file no. 11-0650 (◊) and unknown (*).

β-$Ca_2P_2O_7$ (JCPDS file no. 03-0604) while sodium phosphate phases were $NaPO_3$ compounds with different JCPDS file no. of 11-0650 and 76-0788. The sodium phosphate phases increased with increasing sintering temperature to near crystallization temperature at T_{x1} and decreased with increasing sintering temperature above T_{x1}. Calcium phosphate phases were formed at the sintering temperature near crystallization temperature at T_{x2}. The $P_{45}C_{40}N_{15}$ sample that was sintered at 650°C contained the highest amount of β-$Ca_2P_2O_7$ phase, which is considered to be suitable for bioactive applications [8, 9].

3.2 Compressive Stress and Density

Fig. 2 shows the results of density and compressive stress of porous ceramics at various sintering temperatures. For the high Na_2O content glasses of $P_{45}C_{32}N_{23}$ and $P_{45}C_{36}N_{19}$,

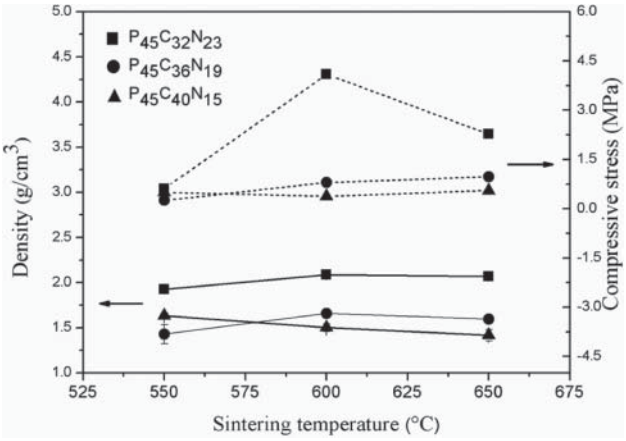

Figure 2. Relationship between compressive stress and density of porous ceramics.

the increase in sintering temperature from 500 to 600°C improve the compressive stress and density of the porous ceramics, while further increasing of the sintering temperature up to 650°C decreased both values. For the lowest Na_2O content glass of $P_{45}C_{40}N_{15}$, both compressive stress and density decreased with increasing sintering temperature.

3.3 Porosity

Fig. 3(a) shows apparent porosity of the three glass sample series. As expected, opposite trends between porosity and density were observed. It can be seen that the $P_{45}C_{32}N_{23}$ samples have lowest porosity ranging between 20–35%, while those of $P_{45}C_{36}N_{19}$ and $P_{45}C_{40}N_{15}$ were between 40–50%. Pore morphologies of all prepared porous ceramics are closely similar as shown in Fig. 4, showing facture images of the three ceramics sintered at the temperature of 650°C. The average pore size shown in Fig. 3(b) revealed the similar trends for all samples with sizes ranging between 150–400 μm, which is suitable for cell growth as described in previous works [14, 15]. However, poorly interconnect pores were formed by the evaporation process of camphor.

The changes in density and compressive strength depend very much on the structure of the glass network. In general, the basic building blocks in the P_2O_5-CaO-Na_2O glass consist of chain structures of PO_4^{3-} tetrahedral structural units while the modifier ions of Ca^{2+} and Na^+ act as charge compensators. The divalent cations Ca^{2+} can form cross-links between non-bridging oxygen atoms of two different PO_4^{3-} tetrahedral chains, leading to the strengthening of phosphate glass network [9, 13]. The density data of the porous sodium calcium phosphate glasses in Fig. 2, shows the lower density values of high CaO samples ($P_{45}C_{36}N_{19}$ and $P_{45}C_{40}N_{15}$), which may be attributed to the crystallization of some crystal phases during sintering. Sodium phosphate and calcium phosphate phases are distributed throughout the glass matrices as can be seen in the larger magnification micrographs in Fig. 5 as investigated by EDS. It is interesting to mention that the high Na_2O content samples ($P_{45}C_{32}N_{23}$ and $P_{45}C_{36}N_{19}$) contain the highest amount of $NaPO_3$ phases especially at low sintering temperatures (550 and 600°C). The surface crystallization of these crystal phases with needle like shape occurred as shown in Fig. 5, or the bright spots in the lower magnification micrographs in Fig. 4(a) and (b) of the ceramic fracture surfaces. This may reduce the pores and enhance the densification in the glass matrix by

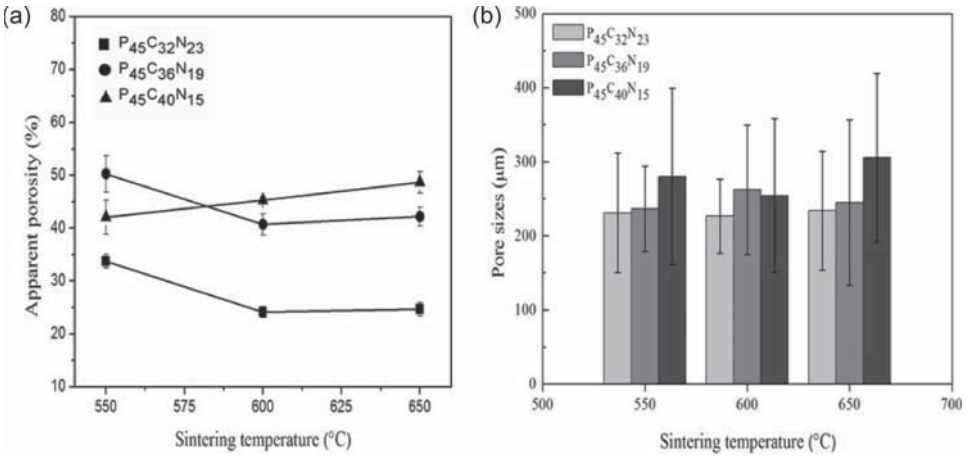

Figure 3. (a) Percentage of apparent porosity and (b) pore size of porous ceramics.

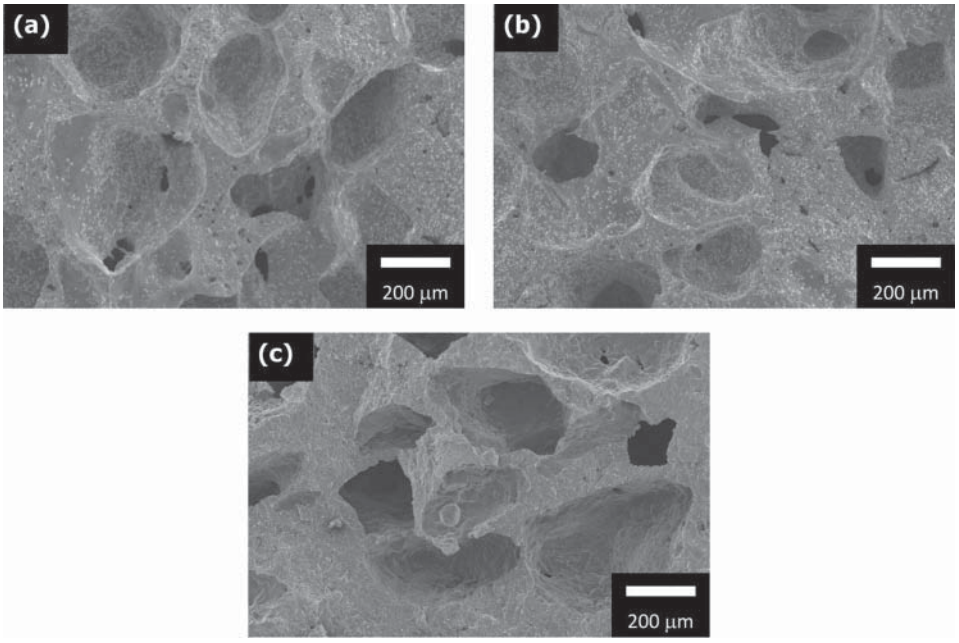

Figure 4. The facture images of porous ceramics sintered at 650°C: (a) $P_{45}C_{32}N_{23}$, (b) $P_{45}C_{36}N_{19}$ and (c) $P_{45}C_{40}N_{15}$.

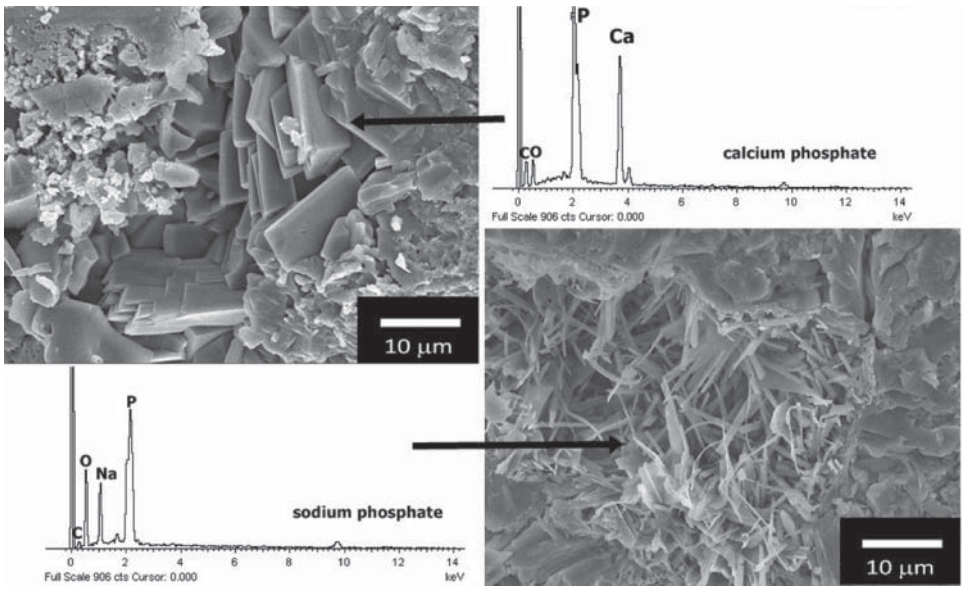

Figure 5. Energy dispersive X-ray spectroscopy (EDX) of calcium phosphate and sodium phosphate phases formed on porous ceramics after sintering at 650°C.

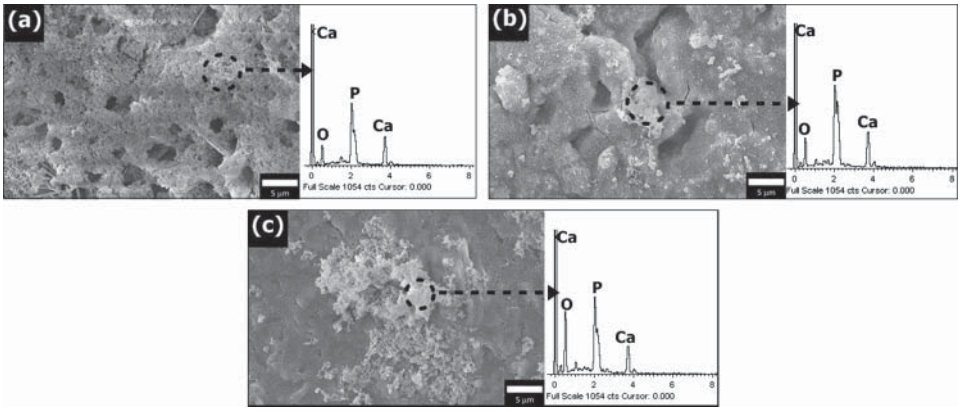

Figure 6. Mictrostructures and energy dispersive X-ray spectroscopy (EDX) of porous ceramics after sintering at 650°Cafter immersion in SBF solution for 7 days: (a) $P_{45}C_{32}N_{23}$, (b) $P_{45}C_{36}N_{19}$, (c) $P_{45}C_{40}N_{15}$ samples.

pulling in the glass particles to be closely attached to each other during sintering. This may result in the highest compressive stress and density values and lowest porosity values of the $P_{45}C_{32}N_{23}$ ceramics.

3.4 Assessment of Bioactive in Vitro

The bioactivity of porous ceramics was assessed in vitro using SBF solution for 7 days and the results are shown in Fig. 6. Formation of bone like apatite layers during bioactivity experiments was evaluated by the investigation of surface morphology. SEM and EDX were used to detect chemical composition of this apatite layer. Apatite-like layers were found to form on the surface of all calcium phosphate porous ceramics, confirmed by EDS spectra where phosphorus (P), calcium (Ca) and oxygen (O) atoms were detected in the apatite layer. On each surface, the formation of individual apatite grains like spherical balls, with diameters in the range of nanometers are clearly revealed. Apatite cell growth increases with increasing Na_2O content [19–20]. Samples having sodium phosphate crystals as a major phase exhibit better apatite cell growth.

The mechanism of apatite cells formation may be explained by initial dissolution of Na^+ and Ca^{2+} ions from the surface of ceramics which accelerate apatite nucleation in SBF solution [19, 22]. The dissolution rates of calcium phosphate phases are lower than that of sodium phosphate phases as the network structure of PO_4^{3-} groups forming cross-links with Ca^{2+} is stronger than that of PO_4^{3-} groups forming chain structure with Na^+ [9, 13]. Therefore, the $P_{45}C_{32}N_{23}$ sample series (Fig. 4(a)) with highest Na_2O content and containing $NaPO_3$ as a major phase possesses the optimum bioactivity as compared to the other samples.

4. Conclusion

Porous ceramics from the P_2O_5-CaO-Na_2O glass system were successfully produced by camphor addition. Changes in CaO/Na_2O ratio played an important role in controlling the densification and phase formation of the ceramics. The pore sizes formed by burnt out camphor were in a range of 150–400 μm for all sample conditions, and are suitable for cell

growth. The crystalline phases precipitated in sintered ceramics could be clearly assigned to calcium phosphate and sodium phosphate phases. In vitro study revealed the formation of apatite layers for all porous ceramics with the maximum apatite cell growth found in the $P_{45}C_{32}N_{23}$ sample series with the highest content of Na_2O and containing sodium phosphate as a major phase.

Acknowledgments

We wish to thank the National Research University Project under Thailand's Office of the Higher Education Commission (OHEC) for financial support. The authors would also like to thank the Thailand Research Fund (TRF), Faculty of Science and the Graduate School Chiang Mai University for financial support.

Reference

1. F. Rahimi, B. T. Maurer, and M. G. Enzweiler, Coralline hydroxyapatite: A bone graft alternative in foot and ankle surgery, *J. Foot. Ankle. Surg*, **36** 192–203 (1997).
2. S. H. Rhee, Synthesis of hydroxyapatite via mechanochemical treatment. *Biomaterials*, **23** 1147–1152 (2002).
3. F-H. Lin, C-J. Liao, K-S. Chen, J-S. Sun, and C-P. Lin, Petal-like apatite formed on the surface of tricalcium phosphate ceramic after soaking in distilled water. *Biomaterials*, **22** 2981–2992 (2001).
4. S-C. Liou and S-Y. Chen, Structural characterization of nano-sized calcium deficient apatite powders. *Biomaterials*, **23** 4541–4547 (2002).
5. D. C. Clupper, J. J MecholskyJr, G. P. LaTorre, and D. C. Greenspan, Bioactivity of tape cast and sintered bioactive glass-ceramic in simulated body fluid. *Biomaterials*, **23** 2599–2606 (2002).
6. R. K. Singh, G. P. Kothiyal, and A. Srinivasan, Bioactivity of SiO_2–CaO–P_2O_5–Na_2O glasses containing zinc–iron oxide. *Appl. Surf. Sci*, **255** 6827–6831 (2009).
7. V. Rajendran, A. V. G. Devi, M. Azooz, and F. H. El-Batal, Physicochemical studies of phosphate based P_2O_5–Na_2O–CaO–TiO_2 glasses for biomedical applications. *J. Non-Cryst. Solids*, **353** 77–84 (2007).
8. W. C. A. Vrouwenvelder, C. G. Groot, and K. de Groot, Histological and biochemical evaluation of osteoblasts cultured on bioactive glass, hydroxyapatite, titanium alloy, and stainless steel. *J. Biomed. Mater. Res*, **27** 465–475 (1993).
9. Hin, T. W., Engineering Materials for Biomedical Applications, World Scientific Publishing Co. Pte. Ltd (2004).
10. K. Franks, I Abrahums, G. Georgiou, and J. C. Knowles, Investigation of thermal parameters and crytallisation in a ternary CaO–Na_2O–P_2O_5-based glass system. *Biomaterials*, **22** 497–501 (2001).
11. I. Ahmed, M. Lewis, I Olsen, and J. C Knowles, Phosphate glasses for tissue engineering: Part 1. Processing and characterisation of a ternary-based P_2O_5–CaO–Na_2O glass system. *Biomaterials*, **25** 491–499 (2004).
12. I. Ahmed, M. Lewis, I Olsen, and J. C Knowles, Phosphate glasses for tissue engineering: Part 2. Processing and characterisation of a ternary-based P_2O_5–CaO–Na_2O glass fibre system. *Biomaterials*, **25** 501–507 (2004).
13. Z. M. Da Costa, W. M. Pontuschka, J. M. Giehl, and C. R. Da Costa, ESR dosimeter based on P_2O_5–CaO–Na_2O glass system. *J. Non-Cryst. Solids*, **352** 3663–3667 (2006).
14. I, Sopyan, M. Mel, S. Ramesh, and K. A. Khalid, Porous hydroxyapatite for artificial bone applications. *Sci. Techol. Adv. Mater*, **8** 116–123 (2007).
15. J. Sundaram, T. D. Durance, and R. Wang, Porous scaffold of gelatin–starch with nanohydroxyapatite composite processed via novel microwave vacuum drying. *Acta.Biomat*, **4** 932–942 (2008).

16. H. R. Ramay and M. Zhang, Preparation of porous hydroxyapatite scaffolds by combination ofthe gel-casting and polymer sponge methods. *Biomaterials*, **24** 3293–3302 (2003).
17. S. Thonglem, K. Pengpat, G. Rujijanagul, S. Eitssayeam, S. Punyanitya, and T. Tunkasiri, Effects of CaO on Properties of P_2O_5-CaO-Na_2O Glasses and Glass Ceramics, Journal of Metals. *Materials and Minerals*, **20** 173–177 (2010).
18. Y. Zhang and J. D. Santos, Microstructural characterization and in vitro apatite formation in CaO–P_2O_5–TiO_2–MgO–Na_2O glass-ceramics. *J. Eur. Ceram.Soc*, **21** 169–175 (2001).
19. T. Kokubo and H. Takadama, How useful is SBF in predicting in vivo bone bioactivity?. *Biomaterials*, **27** 2907–2915 (2006).
20. H-H. Kim, T. Himeno, T. Kokubo, and T. Nakamura, Process and kinetics of bonelike apatite formation on sintered hydroxyapatite in a simulated body fluid. *Biomaterials*, **26** 4366–4373 (2005).
21. J. P. Nayak and K. J. Bera, Sol–gel synthesis of bioglass-ceramics using rice husk ash as a source for silica and its characterization. *J. Non-Cryst. Solids*, **356** 1447–1451 (2010).
22. A. Arvidsson, V. Franke-Stenport, M. Arvidsson, P. Kjellin, Y-T. Sul, and A. Wennerberg, Formation of calcium phosphates on titanium implants with four different bioactive surface preparations. An in vitro study. *J. Mater Sci: Mater Med*, **18** 1945–1954 (2007).
23. A. S. Monem, H. A. ElBatal, E. M. A. Khalil, M. A. Azooz, and Y. M. Hamdy, In vivo behavior of bioactive phosphate glass-ceramics from the system P_2O_5–Na_2O–CaO containing TiO_2. *J. Mater Sci: Mater Med*, **19** 1097–1108 (2008).
24. G. Lutišanová, E. Kuzielová, M. T. Palou, and J. Kozánková, Static and dynamic in vitro test of bioactivity of glass ceramics. *Ceramics-Silikáty* **55** 106–113 (2011).

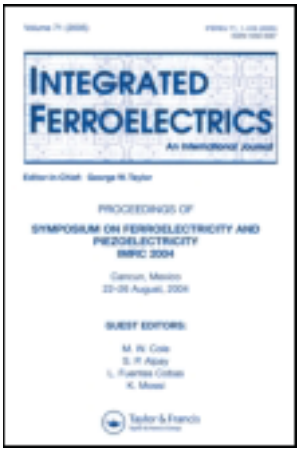

Integrated Ferroelectrics: An International Journal

Publication details, including instructions for authors and subscription information:
http://www.tandfonline.com/loi/ginf20

Microstructure and Dielectric Properties of Bismuth Germanate Glass-Ceramics

Puripat Kantha [a] , Nuttapon Pisitpipathsin [a] & Kamonpan Pengpat [a]

[a] Department of Physics and Materials Science, Faculty of Science , Chiang Mai University , Chiang Mai , 50200 , Thailand

Published online: 30 May 2013.

To cite this article: Puripat Kantha , Nuttapon Pisitpipathsin & Kamonpan Pengpat (2013) Microstructure and Dielectric Properties of Bismuth Germanate Glass-Ceramics, Integrated Ferroelectrics: An International Journal, 142:1, 79-86, DOI: 10.1080/10584587.2013.780406

To link to this article: http://dx.doi.org/10.1080/10584587.2013.780406

Integrated Ferroelectrics, 142:79–86, 2013

ISSN: 1058-4587 print / 1607-8489 online
DOI: 10.1080/10584587.2013.780406

Taylor & Francis
Taylor & Francis Group

Microstructure and Dielectric Properties of Bismuth Germanate Glass-Ceramics

PURIPAT KANTHA, NUTTAPON PISITPIPATHSIN, AND KAMONPAN PENGPAT*

Department of Physics and Materials Science, Faculty of Science, Chiang Mai University, Chiang Mai 50200, Thailand

Bismuth germanate composites containing Bi_2GeO_5-$Bi_4Ge_3O_{12}$ phases were prepared by glass ceramic method and sintering techniques. The existences of three bismuth germanate crystals of Bi_2GeO_5, $Bi_4Ge_3O_{12}$ and $BiBO_3$ were found in XRD patterns. The amount of each phase depended mostly on the sintering temperature where the $Bi_4Ge_3O_{12}$ phase was found to increase with increasing sintering temperature. The mixing of round and pyramidal shape crystals was observed in the sample sintered at 650°C. This gave rise to the improvement in its dielectric properties where the ε_r was found to increase from ∼78 to ∼395 for the sample sintered at 500°C and 650°C, respectively. Moreover, the tanδ was found to decrease greatly with increasing sintering temperature. Thus, this Bi_2GeO_5-$Bi_4Ge_3O_{12}$ composite may be considered as a promising candidate of microwave dielectric materials.

Keywords Bismuth germanate; glass-ceramics; dielectric properties

1. Introduction

Glass ceramics, having properties between glass and crystal, have shown a great potential in electroceramic design, preparation and application. Thus many glass ceramic compositions are being intensively studied and developed. A glass ceramic embedded with Bi_2GeO_5 crystals is one of particular interest as it is an environmentally friendly material and it was found to exhibit ferroelectric properties as first reported by Pengpat and Holland [1, 2]. After that, our work has been on the fabrication of these glass ceramics and we reported that it has a large dielectric constant (ε_r) of 77 with a low dielectric loss (tanδ) of about 0.005 which suits the requirements for use in microwave devices [3, 4]. The ε_r of Bi_2GeO_5 glass ceramics was found to increase up to 246 with a low tanδ after being annealed at 375°C for 12 h, due to the enhanced crystallinity of the glass ceramics [5]. However, these Bi_2GeO_5 crystals, having needle like shape, were crystallized near the surface and distributed heterogeneously within the bulk glass matrix. This non-uniform distribution together with the large amount of residual glass left in the glass matrix may cause the reduction in dielectric constant of the overall bulk glass ceramics. In order to enhance the electrical properties of these glass ceramics, the amount of Bi_2GeO_5 crystals should be increased and distributed homogenously in the samples.

Received June 29, 2012; in final form October 15, 2012.
*Corresponding author. E-mail: kamonpan.p@cmu.ac.th

In general, to produce materials for use in microwave devices, the conventional sintering method has been utilized due to its low cost and easier preparation in comparison to other methods of production. However, the Bi_2GeO_5 phase cannot be prepared by this method due to the metastable form of the Bi_2GeO_5 phase [1–2], thus making it difficult to synthesis by the conventional mixed-oxide method. Therefore, the glass ceramic route was chosen to prepare the pure Bi_2GeO_5 phase before the sintering method.

In this work, pure Bi_2GeO_5 glass ceramic was reground and pressed into pellets in order to enhance the surface area of the Bi_2GeO_5 crystals. This action may help to homogeneously distribute the ground Bi_2GeO_5 crystals within the pressed glass ceramic pellets or compacts. The pressed compacts were then subjected to the sintering method at different temperatures in order to recrystallize and form dense body of glass ceramic samples with mixed phases between Bi_2GeO_5 and $Bi_4Ge_3O_{12}$. The cubic phase of $Bi_4Ge_3O_{12}$ (non-ferroelectric phase) is actually one of most interest for bismuth germanate phases from the Bi_2O_3-GeO_2 glass system, as it possesses valuable electrical properties [6–9]. Therefore, we assume that mixing between $Bi_4Ge_3O_{12}$ and Bi_2GeO_5 phases may help to improve the dielectric properties of these composites as similar results were reported by other studies of binary systems of BNLT-BZT [10] and BNLT-BT ceramics [11]. Phase formation and microstructure of the as-sintered samples were then investigated using X-ray diffraction (XRD) and scanning electron microscopy (SEM) techniques. The physical and electrical properties of the sintered glass ceramics were finally characterized and discussed.

2. Experiments

2.1. Glass-ceramics Preparation

The glass ceramic route was employed for growing pure bismuth germanate (Bi_2GeO_5) crystals in the glass matrix following procedures from our previous work [1–5]. Bismuth oxynitrate ($BiONO_3.H_2O$), reagent grade germanium dioxide (GeO_2) and boron oxide (B_2O_3) were used as starting materials and weighed according to the composition of 60 mol% $BiO_{1.5}$: 20 mol% GeO_2: 20 mol% $BO_{1.5}$. The mixed powders were melted in a Pt crucible at 1075°C for 15 min and splat-quenched on a stainless steel plate at room temperature to form glass. The as-received glasses were subjected to a heat treatment schedule, in order to form pure Bi_2GeO_5 phase, of 18 h at 475°C using heating and cooling rates of 5 and 10°C/min respectively. After that, all samples were ground and made into pellets of 10 mm diameter using uniaxial pressing. The pellets were subsequently sintered between 500°C and 650°C in an electric furnace under a controlled heating and cooling rate of 5°C/min with a dwell time of 4 h to recrystallize and achieved a dense body for the Bi_2GeO_5-$Bi_4Ge_3O_{12}$ glass ceramic samples.

2.2. Glass-ceramics Characterization

After sintering, X-ray diffraction with CuKα radiation and scanning electron microscopy (SEM) were used to investigate the phase formation and microstructure of Bi_2GeO_5-$Bi_4Ge_3O_{12}$ glass ceramic samples. For dielectric measurements, two flat circular surfaces of the selected glass ceramic samples were polished and coated with silver paste as electrodes for electrical contact. The capacitance and loss tangent (tanδ) with variation of temperature between room temperature and 500°C were measured using a LCR meter over a frequency range of 1–100 kHz. The dielectric constant (ε_r) was calculated from the capacitance by

the following equation [12]:

$$\varepsilon_r = Cd/\varepsilon_0 A \tag{1}$$

where C is the capacitance (farads; F), ε_0 is the free space dielectric constant value (8.854×10^{-12} F/m), A is the electrode area (m^2) and d is the thickness (m) of the glass-ceramic sample.

3. Results and Discussion

3.1. Phase Formation

Phase formation investigation of the bismuth germanate glass ceramics sintered at various temperatures was carried out by XRD and their diffraction peaks are illustrated in Fig. 1. The main diffraction peaks of all recrystallized glass ceramic samples contained Bi_2GeO_5 phase with orthorhombic structure (JCPDS file no. 036-0289) after being sintered at 500°C, similar to that of non-recrystallized Bi_2GeO_5 glass ceramics as reported by Pengpat and Kantha [1–5]. The diffraction peaks of the interested bismuth germanate phase: cubic $Bi_4Ge_3O_{12}$ (JCPDS file no. 034-0416) were also found to coexist with the main phase for all sintered samples. The $Bi_4Ge_3O_{12}$ phase increased gradually with increasing sintering temperature and then started to be the dominant phase with a smaller amount of Bi_2GeO_5 phase in the glass ceramic samples sintered at temperatures from 600°C and higher. This is consistent with the results reported in [1–2] as the $Bi_4Ge_3O_{12}$ phase preferred to crystallize in the glass matrix after heat-treatment above 545°C. However, a phase of $BiBO_3$

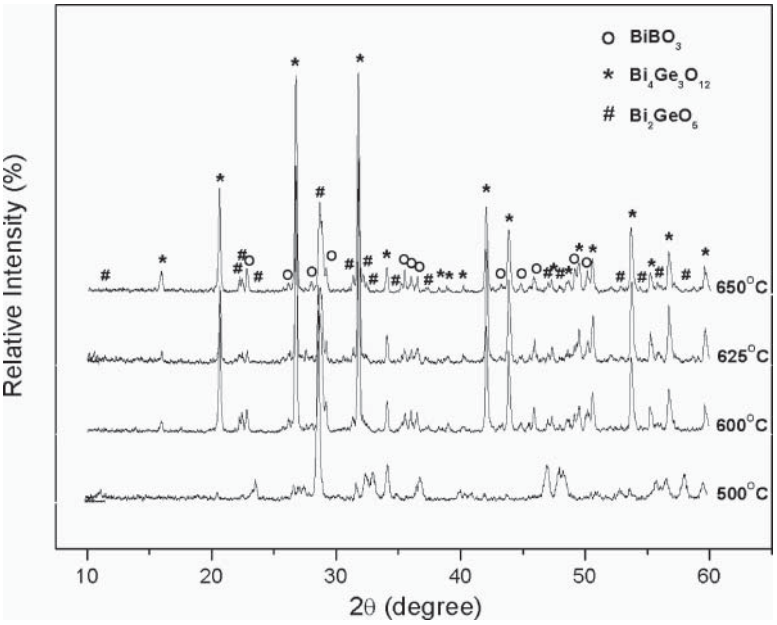

Figure 1. XRD patterns of bismuth germanate glass ceramics recrystallized at various sintering temperatures.

(JCPDS file no. 27-320) was also observed in those glass ceramic samples which may be due to compositional fluctuation during sintering.

3.2. Density and Surface Morphology

Figure 2 shows the SEM micrographs of the as-sintered surfaces of all bismuth germanate glass ceramics. It can be clearly seen that at the higher sintering temperature, lower amounts of pores were observed in the surface of the glass ceramic samples. This agrees well with the density data where the density value increased at higher sintering temperature as shown in Fig.3. From the SEM micrographs in Fig. 2, not only the reduction of porosity was found but also an alteration of morphology was observed with increasing the sintering temperature. At lower sintering temperature, an agglomeration of round shape crystals was revealed while two different types of round and pyramidal shape crystals were observed in the glass ceramic sample sintered at the highest temperature of 650°C. These pyramidal crystals may be $Bi_4Ge_3O_{12}$ phase, similar to the work done by Souza [7] who studied the $Bi_4Ge_3O_{12}$ glass ceramic of the $BiO_{1.5}$-$BO_{1.5}$-GeO_2 system. However, Bi_2GeO_5 and $BiBO_3$ phases were not obviously distinguished from the corresponding SEM micrographs.

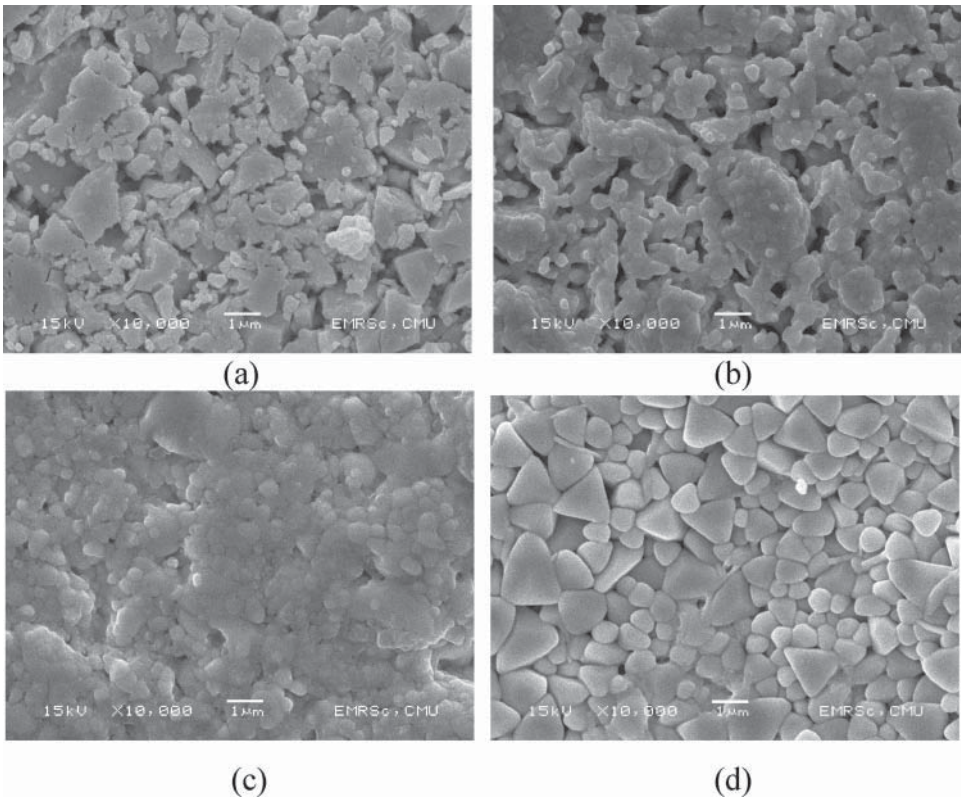

Figure 2. SEM micrographs of bismuth germanate glass ceramics subjected to various sintering temperatures: (a) 500°C, (b) 600°C, (c) 625°C and (d) 650°C.

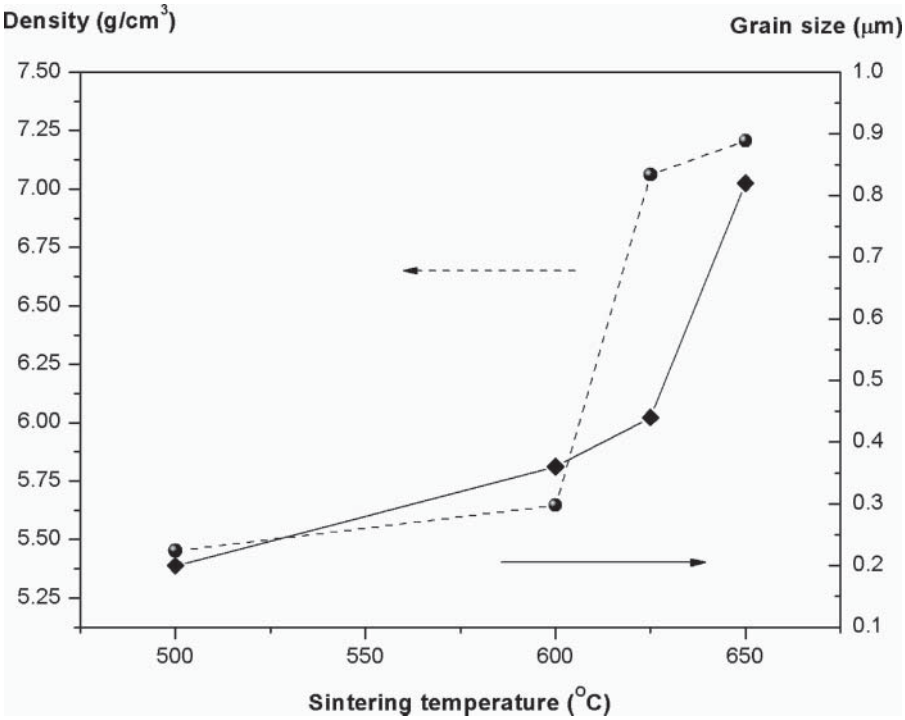

Figure 3. Density and average grain size of bismuth germanate glass ceramics sintered at different temperature**s.**

3.3. Dielectric Properties

Figure 4 shows the temperature dependence of the dielectric constant (ε_r) and dielectric loss (tanδ) of sintered bismuth germanate (Bi_2GeO_5-$Bi_4Ge_3O_{12}$) glass ceramics measured at different frequencies. All recrystallized bismuth germanate glass ceramics exhibited a higher dielectric constant with increasing temperature (from room temperature to 500°C) with dielectric constant decreasing with increasing frequency. This behavior is consistent with that of relaxor-liked ferroelectrics [13]. Higher values of ε_r at lower frequencies could be due to the contribution from many different types of polarizations (i.e., interfacial, dipolar, atomic, ionic or electronic contribution) in the material, with some of that polarization having less contribution to ε_r at high frequency [13]. Not only that, dielectric anomalies, indicating some phase transition (T_x) at around 200–400°C, were found in Bi_2GeO_5-$Bi_4Ge_3O_{12}$ glass ceramic samples sintered at 600 to 650°C, while the sample sintered at 500°C showed no transition in both ε_r and tanδ curves. The glass ceramic sample sintered at 500°C contained Bi_2GeO_5 as the major phase, therefore the phase transition may not be observed for this sample as the Bi_2GeO_5 single crystal has a high phase transition temperature of more than 527°C [1]. For the samples sintered at higher temperatures (600–650°C), the phase transition T_x may be attributed to some structural change of the $Bi_4Ge_3O_{12}$, which was found to be a major phase in those high sintering temperature ceramics, as confirmed by the XRD patterns in Fig.1. Moreover, the higher the sintering temperature, the more profound relaxor behavior was obtained.

Considering the dielectric loss (tanδ) of Bi_2GeO_5-$Bi_4Ge_3O_{12}$ glass ceramics, it was found that the tanδ of all sintered glass ceramics exhibited a strong dependence with both

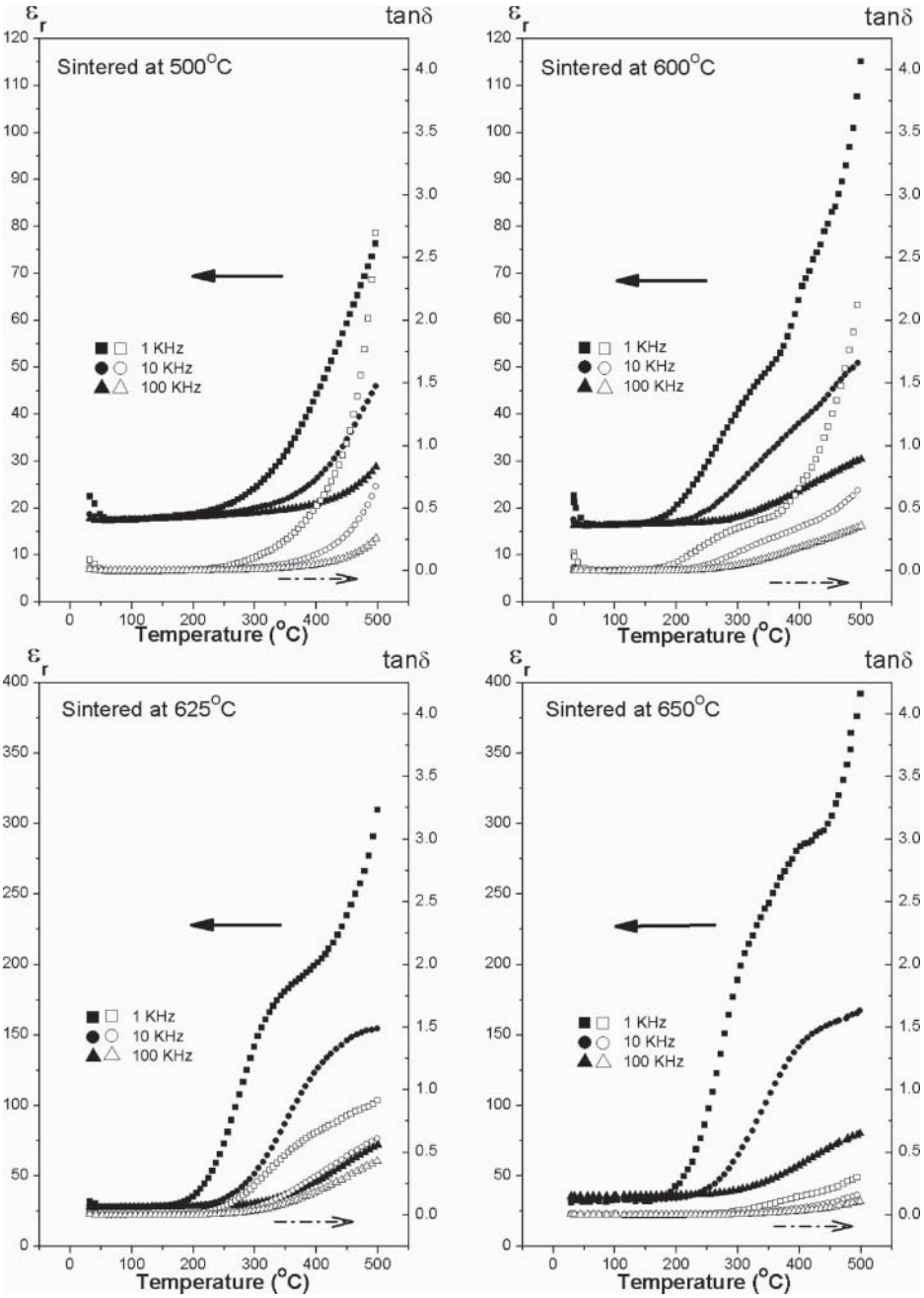

Figure 4. Temperature and frequency dependence of the dielectric constant (ε_r) and dielectric loss (tanδ) of sintered bismuth germanate glass ceramics.

temperature and frequency. The samples sintered at higher temperatures had lower dielectric loss for all frequencies. This may be attributed to the reduction of porosity and increase in density of the samples sintered at higher temperatures as confirmed by SEM micrograph (Fig. 2) and density data (Fig. 3). The dielectric loss values of these ceramics dramatically

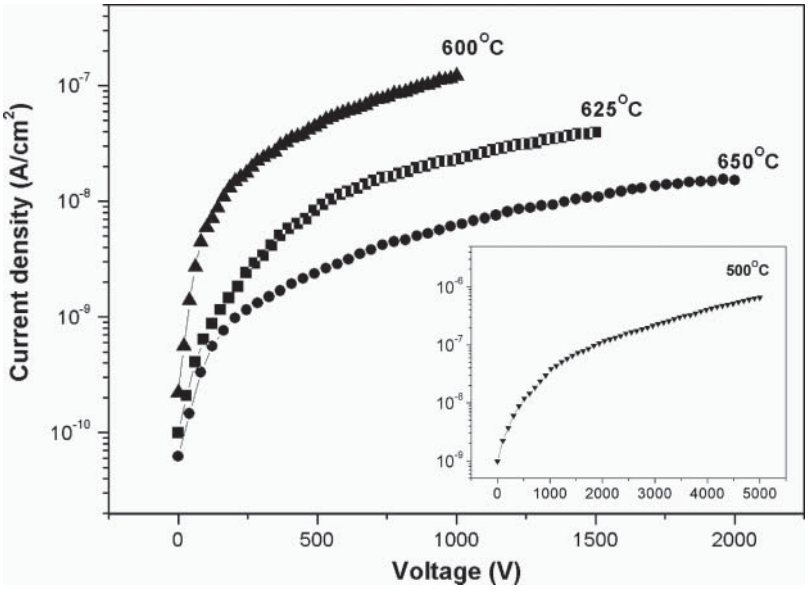

Figure 5. Leakage current density of sintered bismuth germanate glass ceramics at different voltages.

decreased at high frequency (100 kHz), which may be useful for microwave applications where low loss is particularly needed at high frequency.

The leakage current density of all recrystallized glass ceramic samples was measured and plotted versus applied voltage as shown in Fig. 5. Higher leakage current densities were observed for the ceramic sintered at 500°C which also exhibited the highest dielectric loss. As sintering temperature increased, the leakage current density was found to drop to the range of 10^{-8} to 10^{-7} A/cm^2. This confirmed that the high temperature sintered samples have lower conductivity.

4. Conclusions

To homogeneously distribute Bi_2GeO_5 crystals formed by the glass ceramic method, they were reground and sintered from 500 to 650°C to re-grow Bi_2GeO_5 crystals and form dense bismuth germanate glass ceramic bodies. The Bi_2GeO_5 phase only remained as a major phase in samples at 500°C while $Bi_4Ge_3O_{12}$ phase started to be the dominant phase in samples sintered at 600°C and above. The sintering temperature also altered their density, microstructures as well as their dielectric properties. The maximum density with well-defined microstructures was achieved for the sample sintered at 650°C. This sample also provided the highest dielectric constant of 395 with the lowest dielectric loss of 0.29 at the measured temperature of 500°C, compared to that found in the other sintered samples. This may have further applications as microwave dielectric materials.

Acknowledgments

The authors would like to express their sincere gratitude to the Thailand Research Fund (TRF) and Faculty of Science, Chiang Mai University for their financial support. P.Kantha

is also thankful for his financial support from the Royal Golden Jubilee Ph.D. Program and the Graduate School of Chiang Mai University.

References

1. K. Pengpat, and D. Holland, Glass-ceramics containing ferroelectric bismuth germanate (Bi_2GeO_5). *Journal of the European Ceramic Society*, **23**, 1599–1607 (2003).
2. K. Pengpat, and D. Holland, Ferroelectric glass ceramics based on the bismuth germanate system. *Physics and Chemistry of Glasses*, **45**, 79–82 (2004).
3. P. Kantha, S. Sirisoonthorn, and K. Pengpat, The effect of processing parameters on properties of Bi_2GeO_5 glass ceramics. *Advanced Materials Research*, **55–57**, 437–440 (2008).
4. P. Kantha, K. Pengpat, G. Rujijanagul, T. Tunkasiri, S. Eitssayeam, U. Intatha, and S. Sirisoonthorn, Effect of heat treatment conditions on properties of lead-free Bi_2GeO_5 ferroelectric glass ceramics. *AIP Conference Proceedings*, **1151**, 166–168 (2009).
5. P. Kantha, N. Pisitpipathsin, W. Leenakul, S. Eitssayeam, G. Rujijanagul, S. Sirisoonthorn, and K. Pengpat, Enhanced electrical properties of lead-free Bi_2GeO_5 ferroelectric glass ceramics by thermal annealing. *Ferroelectrics*, **416**, 158–167 (2011).
6. V. V. Zyryanov, V. I. Smirnov, and M. I. Ivanovskaya, Mechanochemical synthesis of crystalline compounds in the Bi_2O_3-GeO_2 system. *Inorganic Materials*, **41**, 618–626 (2005).
7. N. C. Souza, R. Lebullenger, M. C. C. Custodio, and A. C. Hernandes, $BiO_{1.5}$-$BO_{1.5}$-GeO_2 glass system and crystallization of $Bi_4Ge_3O_{12}$ phase. *Journal of Non-Crystalline Solids*, **273**, 94–99 (2000).
8. F. A. A. Jesus, R. S. Silva, and Z. S. Macedo, Synthesis of $Bi_4Ge_3O_{12}$ ceramic scintillators by the polymeric precursor method. *Journal of Thermal Analysis and Calorimetry*, **100**, 537–541 (2009).
9. V. Trnovcova, I. Furar, and D. Schultze, Electrical properties of bismuth phosphate and bismuth germanate single crystals. *Solid State Ionics*, **179**, 131–134 (2008).
10. P. Kantha, K. Pengpat, P. Jarupoom, U. Intatha, G. Rujijanagul, and T. Tunkasiri, Phase formation and electrical properties of BNLT-BZT lead-free piezoelectric ceramic system. *Current Applied Physics*, **9**, 460–466 (2009).
11. N. Pisitpipathsin, K. Pengpat, P. Kantha, W. Leenakul, S. Eitssayeam, G. Rujijanagul, and T. Tunkasiri, Dielectric properties of lead-free solid solution of $Bi_{0.487}Na_{0.487}La_{0.017}TiO_3$ and $BaTiO_3$. *Phase Transitions*, **83**, 875–883 (2010).
12. C. Fu, H. Chen, X. Deng, W. Cai, L. Zhou, and Z. Liu, Microstructure and ferroelectric properties of $BaZr_{0.2}Ti_{0.8}O_3$ films prepared by sol-gel. *Integrated Ferroelectrics*, **107**, 24–30 (2009).
13. P. Kantha, N. Pisitpipathsin, K. Pengpat, G. Rujijanagul, R. Guo, and Amar S. Bhalla, Microstructure and electrical properties of $BaFe_{0.5}Nb_{0.5}O_3$ doped with GeO_2 (1–5 wt.%). *Ferroelectrics*, **425**, 27–38 (2011).

Electron. Mater. Lett., Vol. 9, No. 6 (2013), pp. 833-836
DOI: 10.1007/s13391-013-6022-6

Effects of NiO Nanoparticles on Electrical and Magnetoelectric Properties of BNT Based Ceramics

Chatchai Kruea-In,[1] Thitima Glansuvarn,[2] Sukum Eitssayeam,[2] Kamonpan Pengpat,[2] and Gobwute Rujijanagul[2,*]

[1]Faculty of Science and Technology, Chiang Mai Rajabhat University, Chiang Mai 50300, Thailand
[2]Department of Physics and Materials Science, Faculty of Science, Chiang Mai University, Chiang Mai, 50200, Thailand

(received date: 15 October 2012 / accepted date: 9 January 2013 / published date: 10 November 2013)

The properties of 0.94BNT-0.06BT/xNiO lead-free nanocomposites were investigated. The NiO additive influenced dielectric properties as well as the phase transition behavior of the samples. Dielectric properties under applied magnetic fields were also measured. After addition of the additive, the loss tangent could be controlled by an applied magnetic field. Furthermore, the *P-E* hysteresis loop changed from a normal hysteresis loop for the unmodified sample to a constricted loop for the $x = 0.5$ and 1.0 vol. % samples, and then became a lossy capacitor hysteresis loop for the $x = 2.0$ vol. % sample. These results suggest that NiO nanoparticles have a strong influence on the properties of the composites.

Keywords: magnetocapacitance, ferroelectric, nanocomposites

1. INTRODUCTION

Due to environmental concerns, many lead free electroceramics have been investigated, such as bismuth sodium titanate ($(Bi_{0.5}Na_{0.5})TiO_3$, BNT), barium titanate ($BaTiO_3$, BT), and potassium bismuth titanate ($(K_{0.5}Bi_{0.5})TiO_3$, KBT) based materials.[1-7] Among them, BNT is an interesting lead free piezoelectric material with a perovskite structure. It has Bi^{3+} and Na^+ on the A-site of the ABO_3 perovskite structure with a rhombohedral symmetry.[3] BNT has recently been considered to be a promising lead-free piezoelectric material to replace the widely used lead based materials, due to its high remnant polarization at room temperature. However, the large coercive field of BNT ceramics makes them hard to pole as a result of their weak piezoelectric properties. To overcome this problem, many BNT-based solid solutions have been fabricated to improve the properties. Among these solid solutions, $(1-y)$BNT-yBaTiO$_3$ (BNT-BT) ceramics have been intensively investigated by many authors after Xu *et al*. proposed that their BNT-BT ceramics had a morphotropic phase boundary (MPB) for $0.06 < y < 0.10$, and the $y = 0.06$ sample exhibited high piezoelectric properties.[8]

Recently, magnetoelectric (ME) ceramics have attracted considerable attention for their impact on basic science and electronic applications. The properties of these MEs are thought to be induced by the interaction between electrical and magnetic dipoles. Unfortunately, single phase materials which exhibit a large ME at room temperature are very rare. Therefore, researching large ME materials has been an interesting topic of research in recent years. Recently, significant ME values have been found in some multiphase materials, such as composites of BT/$CoFe_2O_4$ and lead zirconate titanate (PZT)/nickel ferrite.[9,10] However, the nanocomposites which show the ME effect have not been widely investigated. Furthermore, many authors have reported that nanocomposites show other interesting properties compared to ordinary composites, such as the enhanced mechanical properties of PZT/Al_2O_3 nanocomposites.[11] In the present work, we report on our investigation of a new nanocomposite of BNT-BT/xNiO. BNT-BT (at a composition of $y = 0.06$) ceramics and NiO nanoparticles were used as the matrix and dispersed phases of the nanocomposites, respectively.

2. EXPERIMENTAL PROCEDURE

$0.94Bi_{0.5}Na_{0.5}TiO_3$-$0.06BaTiO_3$ powders were prepared using the conventional solid-state mixed oxide method. The mixed raw metal oxide powders were calcined at temperatures ranging from 800°C to 900°C for 2 h. The high purity perovskite phase obtained using powders at the optimum calcination temperatures were then combined with NiO ($x =$ 0.5, 1.0 and 2.0 vol. %) nanoparticles (average particles size less than 100 nm) and sintered at 1100°C for 2 h. Phase formation was determined using the x-ray diffraction

*Corresponding author: rujijanagul@yahoo.com

technique (XRD). The dielectric properties were determined at various temperatures and magnetic fields by using an LCR meter (Model 4276A, Hewlett Packard). The *P-E* hysteresis loop was measured at room temperature using a ferroelectric tester (Radiant Technologies Inc.).

3. RESULTS AND DISCUSSION

The phase formation of the studied samples was determined using the XRD technique at room temperature. The XRD patterns in Fig. 1 indicate that all samples exhibited a pure phase with rhombohedral symmetry. Peaks of secondary phases, such as $Bi_{12}TiO_{20}$ and $Bi_4Ti_3O_{12}$, were not observed in the XRD patterns. This result is consistent with that reported in previous works.[12] Furthermore, no peak was observed for the NiO phase in any of the XRD patterns. This may be due to the low level of NiO additive which was too little to be detected at the sensitivity level of the XRD instrument. In addition, intensities of the XRD peaks decreased, and their XRD peak widths decreased, with increasing NiO concentrations. These results indicate that the NiO additive produced a lower degree of crystallinity. Furthermore, structural and chemical composition heterogeneity may have occurred in higher NiO content samples due to the unintentional reaction between the matrix phase and the nanoparticles and/or the partial interdiffusion between BNT-BT and NiO.[13,14]

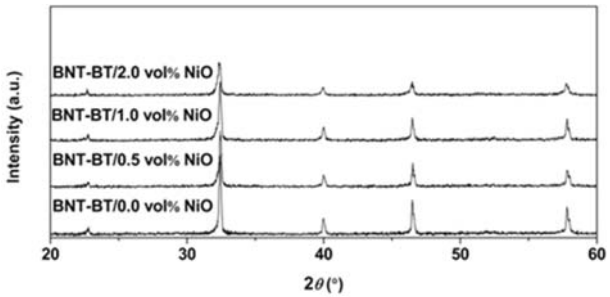

Fig. 1. XRD patterns of BNT-BT/xNiO nanocomposites.

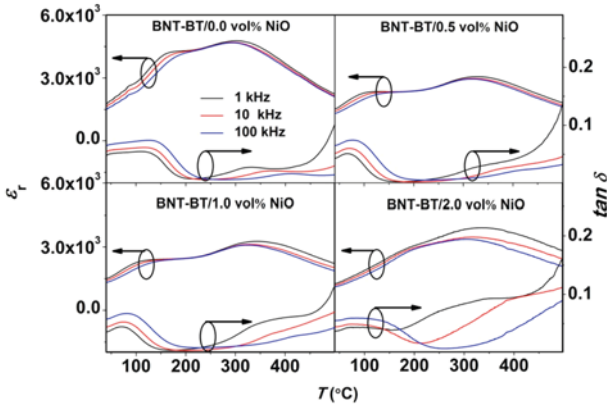

Fig. 2. Dielectric constant (ε_r) and loss tangent (tan δ) as a function of temperature for the nanocomposites.

Figure 2 displays plots of the dielectric constant and loss tangent versus temperature for various NiO concentrations. All samples showed a weak frequency dispersion of the dielectric constant. However, the additive produced a higher dielectric constant-temperature stability, especially for the 0.5 and 1.0 vol. % samples. Two phase transition peaks in the dielectric curve were observed for the BNT-BT ceramic. These peaks correspond to the rhombohedral to tetragonal (T_d~100°C - 180°C) and tetragonal to cubic (T_m~300°C - 340°C) phase transitions. The characteristics of the permittivity curves for the BNT-BT ceramics agreed well with the work done by Xu *et al.*[8] After addition of the additive, however, a variation in T_d and T_m was observed, i.e. there was no trend observed for these temperatures. Furthermore, the two phase transition peaks merged into a single diffuse phase transition at higher NiO contents ($x = 2.0$ vol. % sample). These behaviors may be due to heterogeneity of the structures of the composites. Figure 2 also shows the loss tangent as a function of temperature for various frequencies. The loss tangent tended to decrease with NiO content for the $x \leq 1.0$ samples, but it increased with further NiO content ($x = 2.0$ vol. % sample). The increase in loss tangent for the $x = 2.0$ vol. % sample implies that the $x = 2.0$ vol. % sample had higher electrical conductivities.

To determine the degree of the diffuse phase transition after adding the additive, the diffuseness parameter (δ_γ) was determined, using the following expression:[15]

$$\varepsilon_{r,\max}/\varepsilon_r = \exp((T - T_m)^2/2\delta_\gamma^2) \quad (1)$$

where $\varepsilon_{r,\max}$ is a dielectric constant at T_m. The value of δ_γ was calculated from a plot of $\ln(\varepsilon_{r,\max}/\varepsilon_r)$ versus the $(T - T_m)^2$. Figure 3 illustrates the values of δ_γ as a function of NiO content. The parameter δ_γ increased from 141 K for the unmodi-

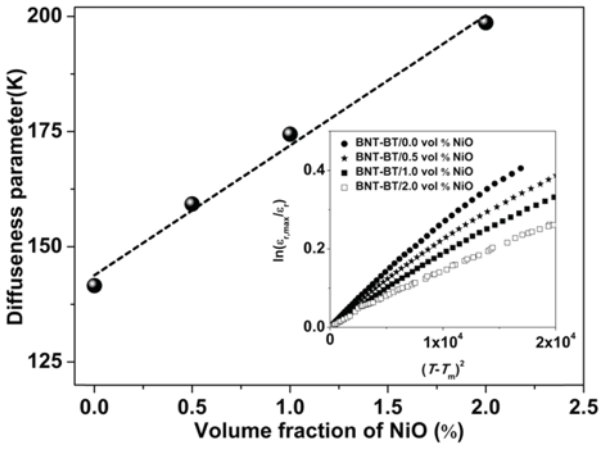

Fig. 3. Diffuseness parameter as a function of NiO content. Inset shows $\ln(\varepsilon_{r,\max}/\varepsilon_r)$ versus $(T - T_m)^2$ of the samples.

fied sample to 198 K for the $x = 2.0$ vol. % sample, confirming that the addition of NiO promoted the diffuse phase transition in the composites.

Figure 4(a) illustrates the variation of magnetocapacitance as a function of applied magnetic field at a 1 kHz frequency. The magnetocapacitance decreased with increasing magnetic field for all samples. The rate of change in the magnetocapacitance increased with increasing NiO content, i.e. the 2.0 vol. % sample showed a larger change in dielectric constant than the 1.0 and 0.5 vol. % samples, respectively. Figure 4(b) displays the magnetoloss as a function of the applied magnetic field at 1 kHz. The samples showed a large change in magnetoloss. The magnetoloss increased with the applied magnetic field, where a higher NiO content sample showed a higher rate of change of the magnetoloss value. This result suggests that the loss tangent can be controlled or tuned by the applied magnetic fields.

Figure 5 presents the ferroelectric hysteresis loops of the studied samples. The pure BNT-BT ceramics exhibited a normal ferroelectric behavior, characterized by a square shaped hysteresis loop. The ferroelectric behavior in this work is similar to the work done by Xu *et al*..[8] For samples with higher NiO contents, the hysteresis loop became a slim and constricted loop. The reason for the presence of the constricted loop in this work may be due to charged defects and/or defect complexes which occurred in the samples due to partial interdiffusion at the interfaces of the BNT-BT and NiO phases.[14] These defects may act as pinning points for the domain rotation which resulted in low polarization values.[14,16,17] Furthermore, it has been suggested that the formation of complex defects can reduce the coercive field, compared with the defect-free case.[14,18] In the case of the $x = 2.0$ vol. % sample, a lossy capacitor hysteresis loop was observed, indicating that this sample had a high conductivity. Plots of current density versus electric field of the samples at room temperature are illustrated in the insets of Fig. 5. The current densities at 13.3 kV/cm were 20.1, 2.8, 3.9 and 9.8 mA/cm^2 for the 0.0, 0.5, 1.0, and 2.0 vol. % samples, respectively. The reduction in current density for the 0.5 and 1.0 vol. % samples is consistent with the decrease in loss tangent at room temperature. However, the 2.0 vol. % sample exhibited a breakdown at an applied electric field of 13.3 kV/cm. The electric breakdown confirms that the 2.0 vol. % sample had high conductivity.

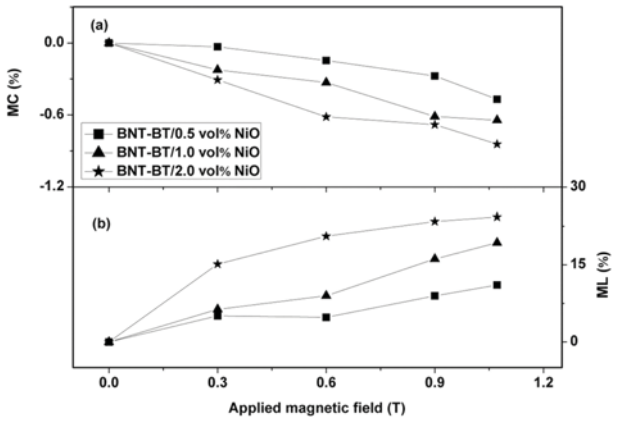

Fig. 4. (a) Magnetocapacitance (MC) and (b) magnetoloss (ML) as a function of applied magnetic field of the samples.

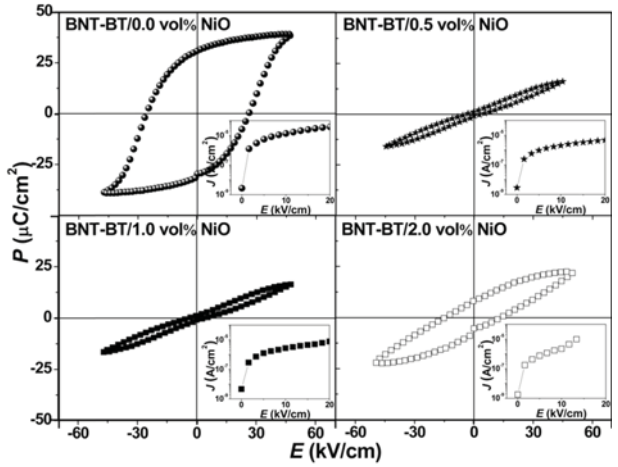

Fig. 5. Polarization (P) versus electric field (E) of the samples. Insets show current density (J) versus E.

4. CONCLUSIONS

In the present work, lead-free BNT-BT/xNiO nanocomposites were fabricated for the first time. The additive did have an influence on dielectric behavior. Obvious changes in ferroelectric properties were observed after adding small amounts of the additive. The additive also produced a large change in loss tangent value under an applied magnetic field suggesting that the loss tangent of this material can be tuned by the magnetic field. Based on these data, the nanocomposites of BNT-BT/xNiO showed many interesting behaviors as compared with pure BNT-BT ceramics.

ACKNOWLEDGEMENTS

This work was supported by The Thailand Research Fund (TRF), Faculty of Science, Chiang Mai University, Chiang Mai Rajabhat University, and Office of the Higher Education Commission (OCHE) Thailand.

REFERENCES

1. H. E. Kim, S. M. Choi, S. Y. Lee, Y. W. Hong, and S. I. Yoo, *Electron. Mater. Lett.* **9**, 325 (2013).
2. O. H. Kwon, B. K. Kim, Y. H. Jo, P. G. Sankar, Y. G. Jung, T. S. Jung, J. W. Lee, and Y. S. Cho, *Electron. Mater. Lett.* **7**, 337 (2011).

3. G. A. Smolenski and A. I. Aganovskaya, *J. Sov. Phys. Solid Stat.* **2**, 2651 (1961).
4. J. Kim, D. Kim, J. Kim, Y. N. Kim, K. N. Hui, and H. Lee, *Electron. Mater. Lett*. **7**, 155 (2011).
5. J. B. Lim, S. Zhang, and T. R. Shrout, *Electron. Mater. Lett*. **7**, 71 (2011).
6. C. C. Diao, C. F. Yang, and J. J. Lin, *J. Nanosci. Nanotechno*. **11**, 10562 (2011).
7. G. Rujijanagul and C. Kruea-In, *Electron. Mater. Lett.* **9**, 455 (2013).
8. C. Xu, D. Lin, and K. W. Kwok, *Solid State Sci.* **10**, 934 (2008).
9. G. Srinivasan, E. T. Rasmussen, B. J. Levin, and R. Hayes, *Phys. Rev. B* **65**, 134402 (2002).
10. C. W. Nan, *Phys. Rev. B* **50**, 6082 (1994).
11. C. Puchmark, G. Rujijanagul, S. Jiansirisomboon, T. Tunkasiri, N. Vittayakorn, T. Comyn, and S. J. Milne, *Curr. Appl. Phys*. **6**, 323 (2006).
12. B. H. Kim, S. J. Han, J. H. Kim, J. H. Lee, B. K. Ahn, and Q. Xu, *Ceram. Int*. **33**, 447 (2007).
13. C. Puchmark, G. Rujijanagul, and S. J. Milne, *Phase Transit*. **83**, 868 (2010).
14. W. Bai, X. Meng, J. Yang, T. Lin, Q. Zhang, J. Ma, J. Sun, and J. Chu, *J. Phys. D Appl. Phys*. **42**, 145008 (2009).
15. S. M. Pilgrim, A. E. Sutherland, and S. R. Winzer, *J. Am. Ceram. Soc.* **73**, 3122 (1990).
16. M. H. Lente and J. A. Eiras, *J. Phys.:Condens. Matter.* **12**, 5939 (2000).
17. S. Takahashi, *Ferroelectrics* **41**, 143 (1982).
18. R. Ahluwalia and W. Cao, *Phys. Rev. B* **63**, 012103 (2001).

Electron. Mater. Lett., Vol. 9, No. 6 (2013), pp. 825-827
DOI: 10.1007/s13391-013-6020-8

Morphology of Potassium Sodium Niobate based Silicate Glass System

Ploypailin Yongsiri,[1] Sukum Eitssayeam,[1,2] Somnuk Sirisoonthorn,[3] and Kamonpan Pengpat[1,2,*]

[1]Department of Physics and Materials Science, Faculty of Science, Chiang Mai University, Chiang Mai, 50200, Thailand
[2]Materials Science Research Center, Faculty of Science, Chiang Mai, 50200, Thailand
[3]National Metal and Materials Technology Center, Klong Luang, Pathumthani 12120, Thailand

(Received date: 14 October 2012 / Accepted date: 9 January 2013 / Published date: 10 November 2013)

In this research, the fabrication of lead-free ferroelectric glass-ceramics from the $(K_{0.5}Na_{0.5})NbO_3$ system via incorporation method was carried out. For the incorporation method, calcined KNN was added into glass batches as a heterogeneous nucleating agent. Glass-ceramics KNNs were prepared from two compositions of KNN-SiO_2 with a ratio of 75 : 25 (C1) and 80 : 20 (C2) mol. %. Thermal properties resulting from DTA showed samples C1 and C2 having glass transition temperatures of 532°C and 520°C and crystallization temperatures of 645°C and 620°C, respectively. The prepared glasses were subsequently subjected to a heat treatment schedule in a temperature range of 500°C - 575°C for crystallization. XRD results showed that the KNN phase occurred in C1. The C2 glass-ceramic samples contained unidentified phases together with the KNN phase. From SEM observation, it was found that bulk crystals with an equiaxed shape of KNN phase dispersed well in all glass-ceramic matrices. Crystal sizes increased with increasing heat treatment temperatures. In C2 glass-ceramics, unidentified phases were found together with the KNN phase.

Keywords: transparent glass-ceramics, KNN, incorporation method

1. INTRODUCTION

Glass ceramics containing $(K_{0.5}Na_{0.5})NbO_3$ [KNN] ferroelectric crystals have been studied extensively since the 1970s[1] as they possess the properties of non-porous glasses and solid crystals, which have given rise to novel materials that have the good mechanical properties of glass and the electro-optical properties of ferroelectric crystals.[1-3] This makes them suitable for electro-optical applications such as electronic parts.[4-6] Moreover, KNN is a lead-free ferroelectric material, making it environmentally friendly.

In this work, in order to reduce the chances of any unwanted second phase that frequently occurs in the conventional glass ceramic method,[7,8] the incorporation method was used to prepare glass-ceramics with KNN as the single crystal phase.

2. EXPERIMENTAL PROCEDURE

Glass ceramics containing KNN crystals were prepared from the incorporation method by using pure KNN powder mixed with SiO_2 and then melted by using conventional melting techniques. Similar to our previous work, for preparing powder and glass, KNN powder was calcined at 900°C for 4 hours. Then, the prepared KNN powder was mixed with SiO_2 in a composition of 75 : 25 mol. % (C1 system) and 80 : 20 mol. % (C2 system). The KNN-SiO_2 batches were melted at 1300°C for 15 min, and then quenched at room temperature. The quenched glasses were subjected to heat treatment schedules in order to study the effect of subsequent heat treatment temperature on phase formation.

The glass-ceramics were characterized in terms of thermal, physical, optical and electrical properties by DTA [Differential thermal analysis; Du Pont Instrument, USA], Archimedes method, XRD [X-ray diffraction; D500 type, Siemens, UK] and SEM [Scanning electron microscope; JSM 6335F type, JEOL, JP], respectively.

3. RESULTS AND DISCUSSION

The as-quenched glasses were transparent and light yellowish. The DTA traces of the C1 and C2 KNN glasses are shown in Fig. 1.

The endothermic peaks and exothermic peaks correspond to the glass transition [T_c] and crystallization temperature [T_g]. The glass thermal stability factor ($D = T_c - T_g$) was found to be approximately 100°C for the C1 system and 110°C for the C2 system, meaning that the C2 glass has slightly better stability than that of C1 glass. The high thermal stability factor specifies the ability of glass to form nano-structured glass-ceramics that controlled heat-treatment.[10] The two glass systems were then subjected to heat treatment

*Corresponding author: kamonpan.p@cmu.ac.th

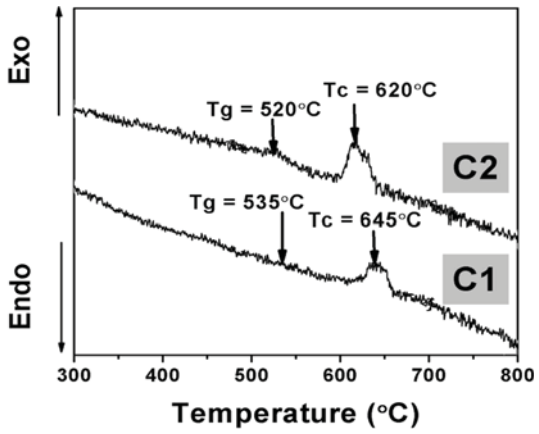

Fig. 1. DTA traces of the as-quenched glasses.

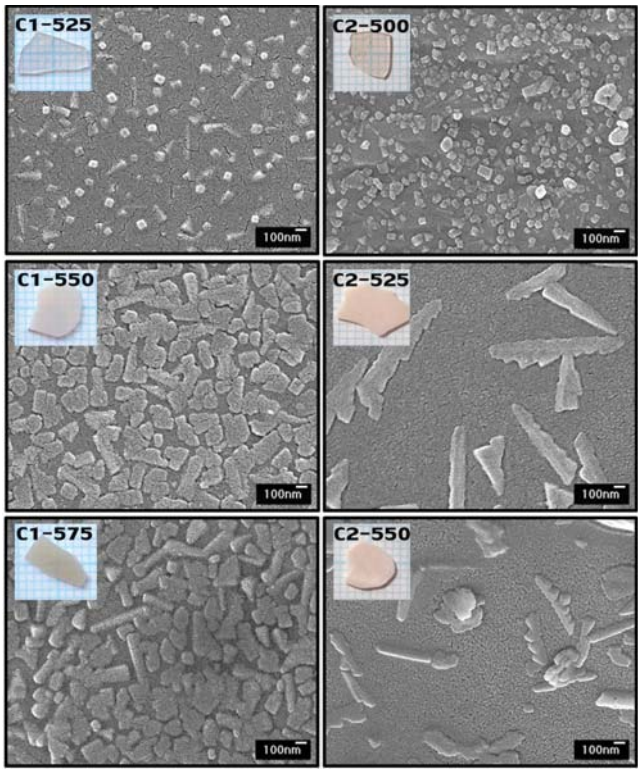

Fig. 2. SEM micrographs of glass-ceramic samples after heat treatment at various temperatures.

schedules depending on their T_g and T_c. The glass appearance is shown in Fig. 2 compared with their microstructure.

The SEM micrographs in Fig. 2 show a bulk crystallization of the KNN crystals with a rectangular shape occurring at the lowest heat treatment samples for both C1 and C2. After a higher heat treatment, an irregular shape of crystals is revealed. The increments in the size of crystals embedded in the glass matrix caused degradation with the glass transparency due to light scattering from the glass sample that has a crystallite size larger than 200 nm.[11] The crystals of all

Table 1. Physical properties data of C1 and C2 glass systems.

Heat treatment temperature	Density (g/cm^3)	Average crystallite size (nm)		Dielectric properties (1 kHz)	
		L	*D*	ε_r	tan δ
C1-quenched	3.61	-	-	-	-
C1-525°C	3.62	219.30 ± 16	108.94 ± 3	111	0.005
C1-550°C	3.77	294.74 ± 22	188.82 ± 15	153	0.042
C1-575°C	3.91	444.24 ± 35	266.45 ± 18	278	0.001
C2-quenched	3.70	-	-	-	-
C2-500°C	3.74	116.45 ± 10	109.32 ± 8	17	0.037
C2-525°C	3.77	886.84 ± 57	157.23 ± 10	134	0.068
C2-550°C	3.90	478.38 ± 31	175.75 ± 27	698	0.043

****L***, length, ***D***, diagonal values.

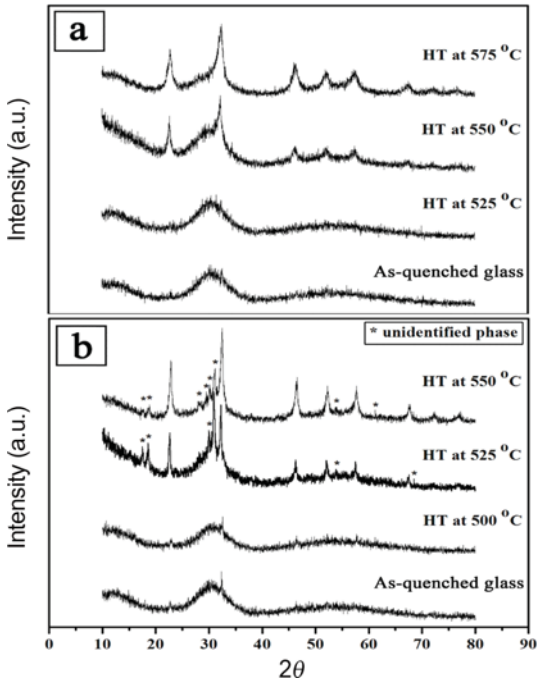

Fig. 3. XRD patterns of glass-ceramic samples at various temperatures. (a) C1 system, (b) C2 system.

samples were homogeneously embedded throughout the glass matrix with random orientations. The average crystal sizes were observed from the SEM micrographs and are summarized in Table 1.

It can be seen from Table 1 that the crystallite size of two glass-ceramic compositions increased with an increasing heat treatment temperature. At the lowest temperature, the crystallite size was smaller than 200 nm and may give less light scattering than the larger crystals. C2 glass-ceramic samples heated at 525°C and 550°C show a different morphology than other samples. This may be due to the occurrence of secondary phases as confirmed by XRD

results shown in Fig. 3. The density of the as-quenched glass was the lowest, and the heat treatment caused a general increase in density, as well as their dielectric constant (ε_r). It can be assumed that the higher density and ε_r of these glass ceramics resulted from the growth of the KNN crystals during the crystallization process.

The XRD patterns in Fig. 3 show diffraction peaks of the as-quenched glass and glass-ceramics. In both the C1 and C2 systems, the XRD patterns of the as-quenched glass and heat treated glass at 525°C and 500°C contain only a broad peak around the diffraction angle of $2\theta = 30$, which indicates a highly amorphous nature. The samples heat treated at higher temperatures (C1; HT > 525°C, C2; HT > 500°C) have diffraction peaks around $2\theta = 23°$, 32°, 46°, 52° and 57°, which confirms the existence of crystalline phases in the amorphous matrix. These crystalline phases were assigned to the potassium sodium niobate crystal phase (JCPDS number 77-0038). However, in the C2 glass system, other additional diffraction peaks occurred, which were marked as unidentified phases. (*)

4. CONCLUSIONS

The ferroelectric glass-ceramics from the KNN-SiO_2 system were successfully prepared via the incorporation method. The heat treatment temperature played a significant role in controlling the microstructure, crystallite sizes, and crystal quantity of the glass ceramics. Nano-crystals of KNN with a crystallite size lower than 200 nm were precipitated in a heat treatment temperature around 500°C (C2 system) and 525°C (C1 system). The results from XRD and SEM confirmed the formation of KNN nano-crystallite in the glass matrix. The crystallite sizes estimated from FE-SEM are in nanometer to micrometer scales depending on heat treatment temperature.

ACKNOWLEDGMENTS

The authors would like to express their sincere gratitude to the TRF, MTEC, and Faculty of Science of Chiang Mai University for financial support. We wish to thank the Graduate School of Chiang Mai University and the NRU under OHEC for financial support. P. Yongsiri would like to thank the TGIST for her scholarship.

REFERENCES

1. L. Egerton and D. M. Dillon, *J. Am. Ceram. Soc.* **42**, 438 (1959).
2. M. N. Ahamad and K. B. R. Varma, *J. Nanosci. Nanotechnol.* **9**, 4910 (2009).
3. N. F. Borrelli and M. M. Layton, *Trans Electron Device* **6**, 511 (1969).
4. G. T. Petrovskii, V. V. Golubkov, O. S. Dymshits, A. A. Zhilin, and M. P. Shepilov, *Glass Phys. Chem.* **29**, 243 (2003).
5. A. A. Zhilin, G. T. Petrovskii, V. V. Golubkov, A. A. Lipovskii, D. K. Tagantsev, B. V. Tatarintsev, and M. P. Phepilov, *J. Non-crystalline Solids* **345**, 182 (2004).
6. T. Prakash, *Electron. Mater. Lett.* **8**, 231 (2012).
7. P. Yongsiri, S. Eitssayeam, U. Inthata, G. Rujijanagul, S. Sirisoonthorn, T. Tunkasiri, and K. Pengpat, *Ferroelectrics* **416**, 144 (2011).
8. C. Karthik and K. B. R. Varma, *J. Nanosci. Nanotechnol.* **7**, 1006 (2007).
9. P. Yongsiri, S. Eitssayeam, G. Rujijanagul, S. Sirisoonthorn, T. Tunkasiri, and K. Pengpat, *Nanoscale. Res. Lett.* **7**, 136 (2012).
10. Y. S. Kim, K. H. Lee, T. H. Kim, Y. J. Jung, and B. K. Ryu, *Electron. Mater. Lett.* **4**, 1 (2008).
11. R. S. Chaliha, V. S. Tiwari, P. K. Gupta, K. Annapurna, A. Tarafder, and B. Karmakar, *J. Mater. Sci.: Mater. Electron.* **7**, 728 (2011).

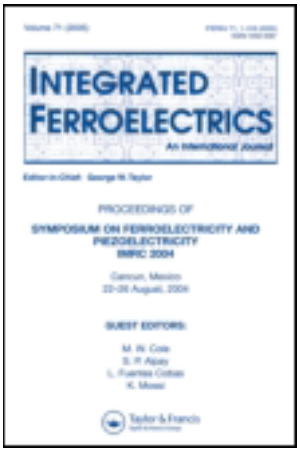

Integrated Ferroelectrics: An International Journal

Publication details, including instructions for authors and subscription information:
http://www.tandfonline.com/loi/ginf20

Magnetic Bioactive $SrFe_{12}O_{19}$-SiO_2-CaO-Na_2O-P_2O_5 Glass-Ceramics for Hyperthermia Treatment of Bone Cancer

W. Leenakul [a] , P. Intawin [a] , J. Ruangsuriya [b] , P. Jantaratana [c] & K. Pengpat [a]

[a] Department of Physics and Materials Science, Faculty of Science , Chiang Mai University , Chiang Mai , 50200 , Thailand

[b] Department of Biochemistry, Faculty of Medicine , Chiang Mai University , Chiang Mai , 50200 , Thailand

[c] Magnetic Materials Speciality Research Unit, Department of Physics, Faculty of Science , Kasetsart University , Bangkok , 10900 , Thailand

Published online: 07 Dec 2013.

To cite this article: W. Leenakul , P. Intawin , J. Ruangsuriya , P. Jantaratana & K. Pengpat (2013) Magnetic Bioactive $SrFe_{12}O_{19}$-SiO_2-CaO-Na_2O-P_2O_5 Glass-Ceramics for Hyperthermia Treatment of Bone Cancer, Integrated Ferroelectrics: An International Journal, 148:1, 81-89, DOI: 10.1080/10584587.2013.852034

To link to this article: http://dx.doi.org/10.1080/10584587.2013.852034

Integrated Ferroelectrics, 148:81–89, 2013

ISSN: 1058-4587 print / 1607-8489 online
DOI: 10.1080/10584587.2013.852034

Taylor & Francis
Taylor & Francis Group

Magnetic Bioactive $SrFe_{12}O_{19}$-SiO_2-CaO-Na_2O-P_2O_5 Glass-Ceramics for Hyperthermia Treatment of Bone Cancer

W. LEENAKUL,[1] P. INTAWIN,[1] J. RUANGSURIYA,[2]
P. JANTARATANA,[3] AND K. PENGPAT[1,*]

[1]Department of Physics and Materials Science, Faculty of Science, Chiang Mai University, Chiang Mai 50200, Thailand
[2]Department of Biochemistry, Faculty of Medicine, Chiang Mai University, Chiang Mai 50200, Thailand
[3]Magnetic Materials Speciality Research Unit, Department of Physics, Faculty of Science, Kasetsart University, Bangkok 10900, Thailand

The magnetic bioglass-ceramics were introduced for hyperthermia treatment of bone cancer. The aim of this work was to study the magnetic properties of ferrimagnetic glass-ceramics from $SrFe_{12}O_{19}$(SF)-SiO_2-CaO-Na_2O-P_2O_5 system by using the modified solid-state sintering method. The results showed that sodium calcium silicate ($Na_4Ca_4Si_6O_{18}$), strontium iron oxide ($SrFe_{12}O_{19}$) and iron oxide (Fe_2O_3) were precipitated in all samples. The saturation magnetization (M_s), remanence (M_r) and coercivity (H_c) increased by the addition of SF in the bioglass. The samples were soaked in simulated body fluid (SBF) for 14 days in order to investigate the bioactivity of the samples in vitro. The apatite layer was found on the surface of all bioglass-ceramics confirming their biocompatibility and it increased with increasing strontium ferrite content.

Keywords 45S5 bioglass; ferrimagnetic; solid-state sintering; biocompatibility

Introduction

Bioglass® 45S5, firstly discovered by Hench et al. [1], is one of the commercially available bioactive materials used extensively in medical applications. After his discovery, many researchers have focused on studying and developing this bioglass for a variety of medical applications [2, 3]. Recently, development of bioglass-ceramics with good bioactivity and possessing magnetic properties has received much attention as a thermo-seed in hyperthermia treatment of cancer, especially deep seated bone tumors. When glass-ceramic granules are implanted around tumors and then subjected to alternating magnetic field, heat is generated from the magnetic loss killing the tumors. In order to evaluate the materials for hyperthermia applications, room temperature hysteresis cycles were performed at much lower field amplitudes, for example about ±500 Oe. Generally [4], such tumors are effectively destroyed at temperatures around 42–45°C, without damaging of normal tissue. For this purpose, ferrimagnetic bioactive glass-ceramic is one of the potential candidates and

Received December 9, 2012; in final form August 25, 2013.
*Corresponding author. E-mail: kamonpan.p@cmu.ac.th

is being developed. Shah et al. [2] reported the ferromagnetic $ZnFe_2O_4$ containing bioactive glass-ceramic system $xZnO:25Fe_2O_3:(40\text{-}x):SiO_2:CaO:7P_2O_5:3Na_2O$ (x = 4, 6, 8, 10). Results showed that the saturation magnetization, coercivity and hence hysteresis area increased with increasing ZnO content. The $Li_2O\text{-}MnO_2\text{-}CaO\text{-}P_2O_5\text{-}SiO_2\text{-}Fe_2O_3$ glass system containing Li and Mn ferrite phase also shows high bioactivity [3]. Li et al. [4] reported the doping of Mn ferrite in $CaO\text{-}SiO_2\text{-}P_2O_5\text{-}MgO\text{-}CaF_2$ bioglass-ceramics, resulted in the development of magnetic properties. However this dopant reduced the bioactivity of the materials. Nevertheless, to the best of our knowledge, bioactive glass-ceramics containing strontium ferrite (Sr) as the magnetic phase has not been yet reported.

The motivation for the addition of Sr ferrite is due to its good biological properties and magnetic properties [5]. Researchers have shown that ion release from Sr doped silicate glass enhanced bone cell activity. Moreover, these Sr-doped glasses promoted osteoblast proliferation and alkaline phosphatase (ALP) activity when directly applied in contact with cells as solid bioglass-discs.

The present work, therefore, attempted to fabricate the $SiO_2\text{-}CaO\text{-}Na_2O\text{-}P_2O_5$ bioactive glass-ceramics containing $SrFe_{12}O_{19}$ (SrF) using the modified solid-state sintering method. In this method, SrF crystals were firstly produced using the solid-state sintering technique and then added to 45S5 bioglass powder, which was then further mixed and sintered to form the glass-ceramics. The influence of SrF addition on the structural and magnetic properties of the prepared glass-ceramics was studied and the bioactive properties of these materials were also investigated *in vitro*.

2. Experimental

2.1 Preparation of Materials

The samples were obtained using the modified sintering method. Firstly, strontium ferrite was produced starting from a mixture of Fe_2O_3 and $SrCO_3$, keeping the proportional ratio of 6:1. The mixture was calcined at 900°C for 6 h.

Secondly, 45S5 bioglass was produced by melting appropriate combinations of 45 wt.% SiO_2, 24.5 wt.% Na_2O, 24.5 wt.% CaO and 6 wt.% P_2O_5 in an alumina crucible. The mixture was melted at 1300°C for 2h. The glass was crushed and ground into powder which was then mixed with the calcined strontium ferrite $SrFe_{12}O_{19}$ at 5, 10, 20, and 40 wt.%. The respective samples were labeled with code names: 5SrF, 10SrF, 20SrF, and 40SrF. The green bodies were then sintered at 800°C for 2 h.

2.2 Materials Characterization

Thermal parameters (the glass transition temperature; T_g and crystallization temperature; T_c) of each samples were measured using differential thermal analysis (DTA). The phase structure was detected by X-ray diffractometer (XRD). Magnetic properties were measured by a vibrating sample magnetometer (VSM) at room temperature. Scanning electron microscopy (SEM) was used to characterize the microstructures of the magnetic bioglass-ceramics. In vitro test was carried out by soaking in simulated body fluid (SBF) for 14 days. The variation of ion concentrations in the SBF solution after soaking the sample was monitored by using inductive coupled plasma model (ICP). The changes in pH of the SBF solution as a function of time were measured using a pH meter.

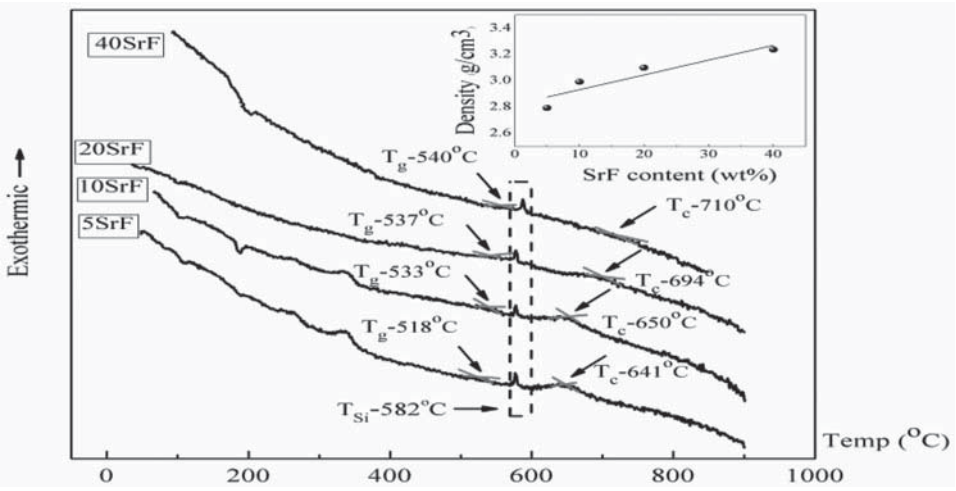

Figure 1. DTA traces and densities of glass samples. (Color figure available online.)

2.3 Cytotoxicity Measurement

Human osteoblast cell line (hFOB) cells were plated in each well of a 96-well plate at the density of 10000 cell/cm^2 in the total volume of 100 μl and the plate was incubated for 24 hours to let the cells attach on the surface of the well plate. Then, 150 μl of the fresh medium was replaced and UV-sterilised materials discs (size 0.06 g) were added onto the cell layer in each well. The cells were cultured with the materials for 4 days and the methyl-thiazolyl-tetrazolium (MTT) assay was then performed.

MTT assay was performed by removing the culture medium from each well and 150 μl of working MTT solution was added into each well. The plate was then incubated for 4 hours with the MTT solution and the solution was discarded. Each well had 100 μl DMSO added and then shaken on a shaker for 5 minutes. The materials were carefully removed from the well and the solution was determined by the light absorption at 540 nm.

3. Results and Discussion

The inclusion of SrF content was found to affect the thermal parameters (T_g and T_c), as shown in the DTA traces (Fig. 1). The trend of increasing density with SrF content was observed as 45S5 has a lower density (2.7 g/cm^3) than that of the SrF crystal (5.1 g/cm^3) as illustrated in the inset of Fig. 1. Generally, changes in thermal parameters with composition reflect a structural evolution in the glass network, and the linear trend of density value observed in this study confirms that no change in glass network occurred in the 45S5 bioactive glass samples with the addition of SrF compounds.

The phase formation behavior during the sintering process of the samples was investigated by XRD (Fig. 2). During the sintering process of 5SrF-20SrF with constant heating rate (5°C/min), the developments of three crystalline phases were obtained, including sodium calcium silicate ($Na_4Ca_4Si_6O_{18}$), strontium iron oxide ($SrFe_{12}O_{19}$) and iron oxide (Fe_2O_3). The intensity of the $SrFe_{12}O_{19}$ and Fe_2O_3 signal increased while the intensity of $Na_4Ca_4Si_6O_{18}$ signals decreased with increasing strontium ferrite content (5–20 SrF). However, the intensity of Fe_2O_3 phase was found to disappear in the 40SrF sample. These

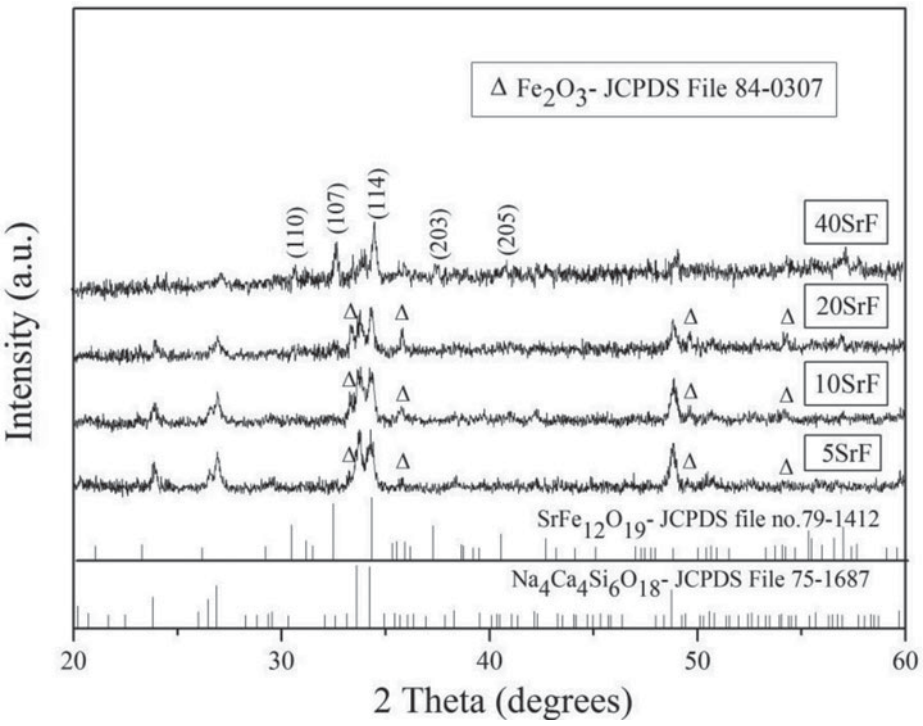

Figure 2. XRD patterns of the glass-ceramic samples.

samples were sintered at the same temperature of 800°C, however, their T_c(s) are different as can be seen from the DTA result (Fig. 1). These T_c (s) correspond to the crystallization of the $Na_4Ca_4Si_6O_{18}$ phase, which was faster for the lower T_c samples (5–20 SrF). The remaining heating may cause the decomposition of $SrFe_{12}O_{19}$, giving rise to the Fe_2O_3 phase in these samples. The higher amount of SrF in the 40SrF sample with high T_c, provided higher stability of the SrF phase.

The Hysteresis loops of all samples (Fig. 3) exhibit similar magnetic behavior, showing a wide hysteresis loop and high coercive field which confirms the characteristic of a hard magnetic material. Magnetic properties were strongly dependent on the added SrF content. The saturation magnetization (M_s), remanence (M_r) and coercivity increased with increasing SrF content as shown in the inset of Fig. 3. The 40 SrF sample had the highest magnetic phase with the highest value of saturation magnetization.

In addition, magnetic loss of materials can be calculated and is presented in the inset of Fig. 3. It is clearly seen that, for an applied field of ± 10 kOe, the area of the hysteresis loop increased with increasing content of SrF. The maximum area was obtained from the 40SrF glass ceramic sample exhibiting the highest magnetic phase content.

The enhancement of this magnetic property was a consequence of the crystallization process. The lower SrF content samples (5–20 wt.%) contained the magnetite Fe_2O_3 phase which played an important role in the enhancement of magnetic properties of the glass ceramics. Moreover, the XRD pattern of the 20SrF sample showed a small trace of the wanted SrF ($SrFe_{12}O_{19}$) phase which could easily be obtained for the higher SrF samples such as the 40 SrF samples.

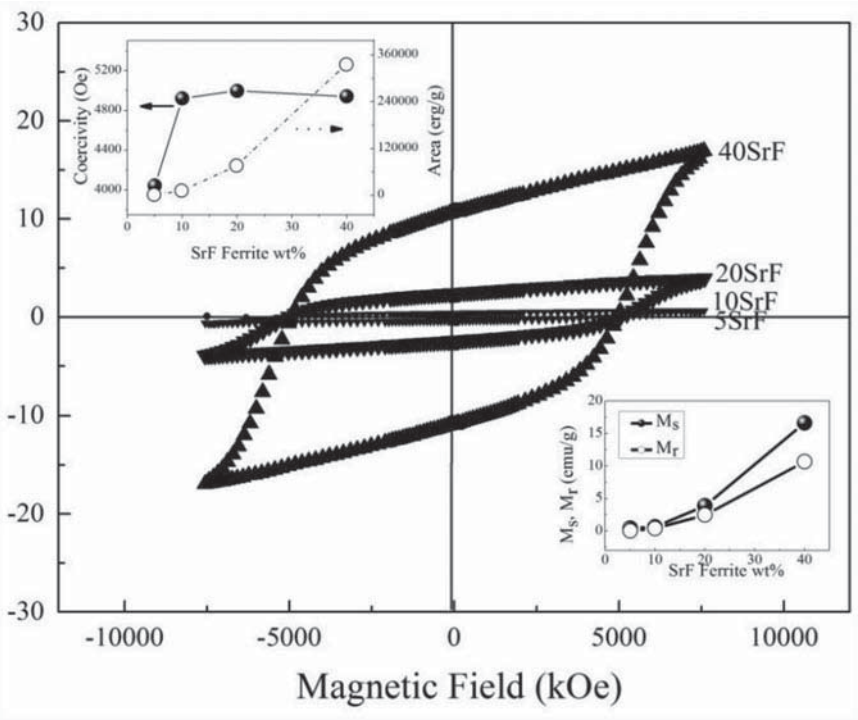

Figure 3. Hysteresis loops and magnetic properties of the glass-ceramic samples.

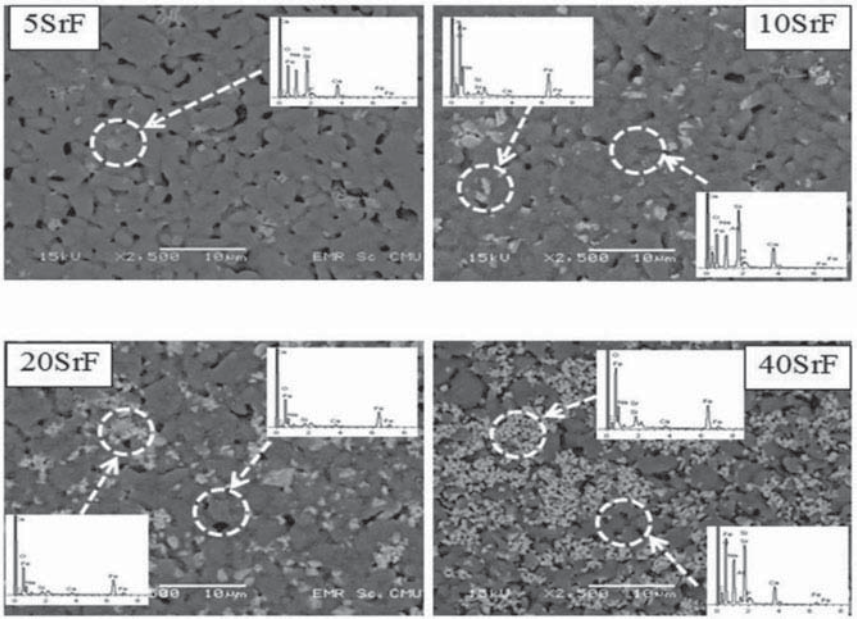

Figure 4. Backscattered images and EDS analyses of glass-ceramics.

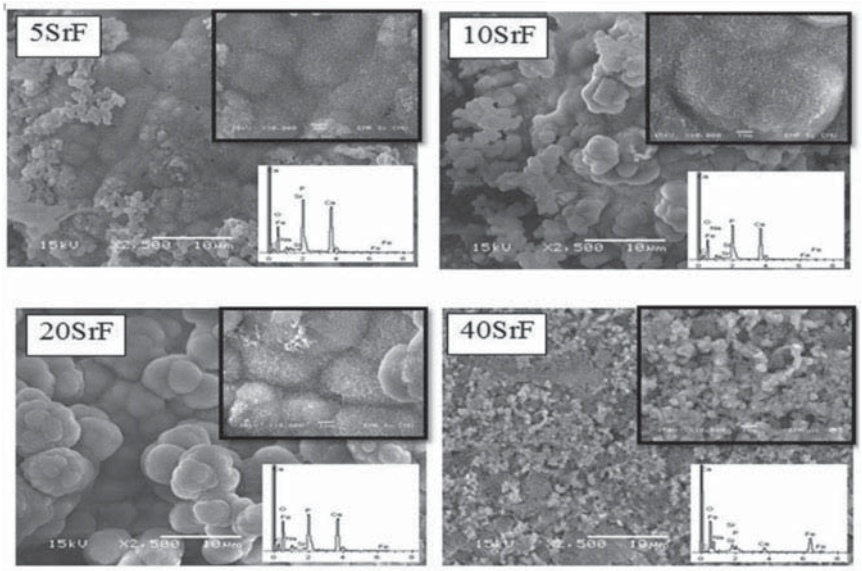

Figure 5. SEM micrographs and EDS analyses of glass-ceramic samples after 14 days in SBF.

Figure 4 illustrates the backscattered micrographs of all samples sintered at 800°C before incubating in SBF. The micrographs reveal small granular crystals distributed in the glass ceramic fracture surface. EDS analysis indicated that these granular crystals (bright areas) contained high concentration of Fe, O, and Sr. It may be assumed that these crystals are $SrFe_{12}O_{19}$ phase. The matrices (dark area) of all samples consisted of Si, O, Na and Ca atoms as shown in the corresponding EDS spectra. Therefore, $Na_4Ca_4Si_6O_{18}$ crystals may be embedded in these matrices. However, the difference in atomic number of the glass matrix and $Na_4Ca_4Si_6O_{18}$ crystal may be too low to show the atomic contrast image of these two phases using backscattered mode.

Figure 5 shows SEM images of the sintered samples for various SrF content after being incubated in SBF for 14 days. The surfaces of all samples were covered by a newly formed layer of numerous spherical particles. EDS analysis revealed that these spherical particles contained very high concentrations of P and Ca, indicating the formation of a hydroxyl carbonate apatite (CHAp) layer. This could mean that all of the samples were bioactive. With increasing SrF content, the particle sizes of CHAp slightly increased. Also, the samples having higher strontium ferrite contents (20SrF) exhibited better apatite cell growth. EDS results also showed a remarkable increase in Sr content, while Si content decreased with increasing SrF content. This may be attributed to the substitution of some Ca sites of the hydroxyl carbonate apatite layer by Sr ions to form $(Ca,Sr)_5(PO_4)_3(OH)$ phase as also reported in [7]. Pina et al. also reported that the Sr-substituted Ca-P layer is expected to produce enhanced biological and chemical responses in the body [8]. These results confirm that the addition of the SrF magnetite phase does not inhibit bioactivity.

Figure 6 shows the variation of Ca and P ion concentrations as well as pH values in the SBF 14 days. In the first 3 days, P and Ca ions increased with increasing SrF content in all samples. This can be explained by the rapid ion exchange mechanism between the glass network modifiers (Na^+ and Ca^{2+}) with H^+ (or H_3O^+) ions in the SBF solution. The

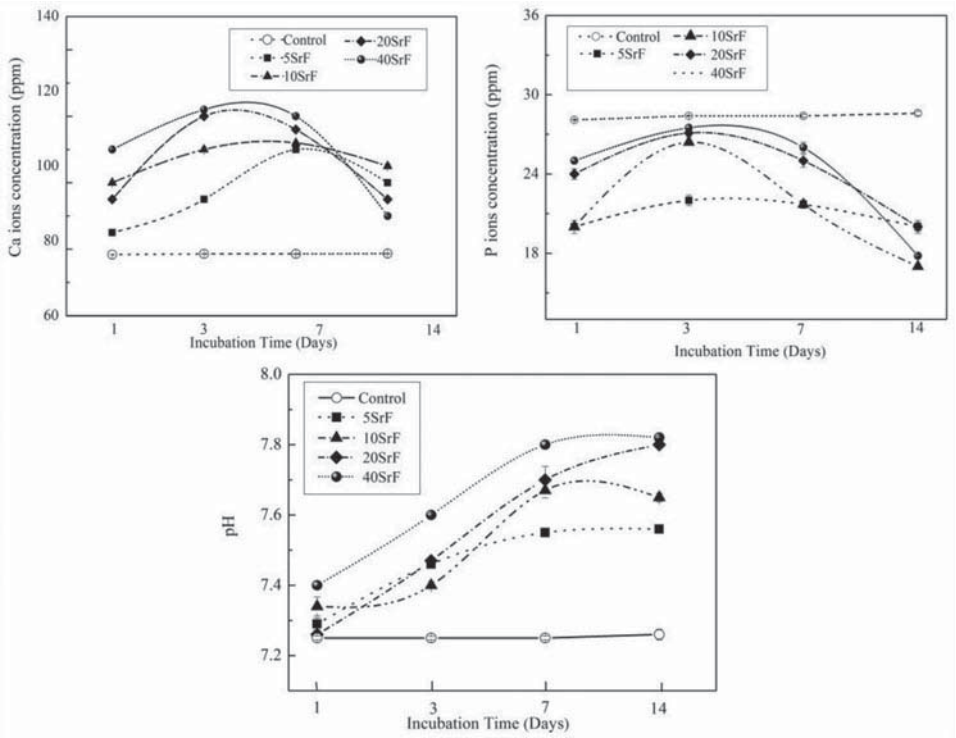

Figure 6. Ion concentrations and pH value of SBF after incubating for various times.

pH value in the first 3 days also increased due to the consumption of H^+ ions from the SBF solution and the continuous formation of Si–OH layers. After 3 days, the concentrations of calcium and phosphorus slightly dropped, especially for the 40SrF sample. The decrease in Ca and P ion concentrations may be associated with the migration of Ca^{2+} and PO_4^{3-} to the silica-rich surface which caused the rapid growth of the carbonated hydroxyapatite (HCA) layer [9].

The results shown in Fig. 6 confirm that the apatite formation observed with SEM and EDS (Fig. 5) was a result of reprecipitation of the ions dissoluted from the materials. Both calcium and phosphate concentration was subsequently drop in the late time point becoming carbonated hydroxyapatite covering the surface of the materials. Consistently, the pH of the material dissolution remained high to support the apatite layer formation. The formation of the apatite layer implies biocompatibility of the materials to bone.

The cytotoxicity test by MTT assay, using hFOB as a model, indicated that the studied glass-ceramic samples were non-toxic to the cells when the samples have an increasing SrF contents ranging from 5–40 wt.% (Fig. 7). A significant increase in metabolic activity of the cells incubated with the materials was observed when the SrF content increased. Especially, the samples with the highest SrF contents (40 wt.%) exhibited better living cellular activity. This finding has a good consistency with the SEM results, ion concentration and pH after the materials were incubated in SBF for 14 days. This evidence shows that hFOB cell activity could be improved by the presence of SrF content in the glass-ceramic samples. This result confirmed that all of the tested materials are biocompatible and bioactive.

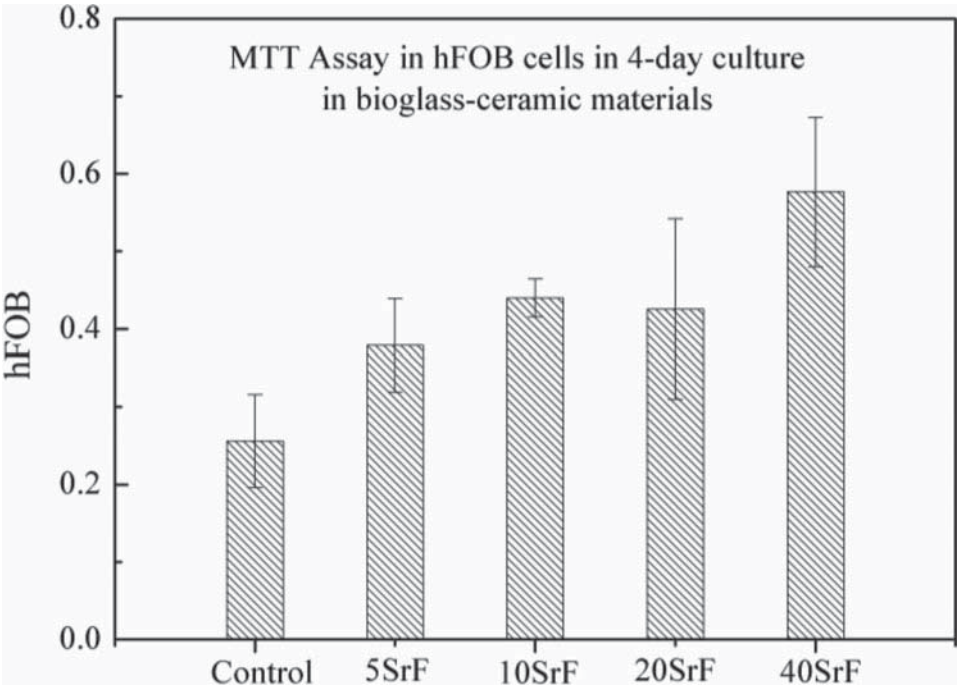

Figure 7. MTT Assay in hFOB in 4-days culture in glass-ceramic materials.

To confirm that the materials are biocompatible to the bone cells, MTT assay was employed and it was clearly shown that the cellular activity was higher when the percentage of SrF increased. It was shown that the materials are highly biocompatible.

4. Conclusion

Magnetic glass-ceramics of the glass-ceramics system SrF-SiO_2-CaO-Na_2O-P_2O_5 were obtained by modified sintering method. These glass-ceramics contained $SrFe_{12}O_{19}$, Fe_2O_3 and $Na_4Ca_4Si_6O_{18}$ phases. Characteristic of a hard magnetic material were found for all samples as confirmed by their hysteresis loops. The addition of SrF not only improves the magnetic properties of the glass-ceramics, but also enhances the bioactivity of the samples especially for the highest BF content sample (40SrF).

Acknowledgments

The authors would like to thank the Thailand Research Fund (TRF) and the National Research University (NRU), Office of Higher Education Commission and Faculty of Science, Chiang Mai University and Graduate School Chiang Mai University, Thailand, for financial support

References

1. L. L. Hence, R. J. Splinter, W. C. Allen, and T. K. Greenlee, Bonding mechanisms at the interface of ceramic prosthetic materials. *J. biomed. Mater. res* **2.**, 117–141 (1971).

2. S. A. Shah, M. U. Hashmi, S. Alam, and A Shamim, Magnetic and bioactivity evaluation of ferrimagnetic $ZnFe_2O_4$ containing glass ceramics for the hyperthermia treatment of cancer. *J. Magn, Magn. Mater.* **322**, 375–381 (2010).
3. C. S. Hsi, H. Z. Cheng, H. J. Hsu, *et al*., Crystallization kinetics and magnetic properties of iron oxide contained $25Li_2O$–$8MnO_2$–$20CaO$–$2P_2O_5$–$45SiO_2$ glasses. *J. Eur. Ceram. Soc*. **27**(10), 3171–3176 (2007).
4. G. D. Li, S. Feng, and D. Zhou, Magnetic bioactive glass ceramic in the system CaO-P_2O_5-SiO_2-MgO-CaF_2-MnO_2-Fe_2O_3 for hyperthermia treatment of bone tumor. *J. Mater. Sci: Mater. Med.* **22**, 2197–2206 (2001).
5. E. Gentleman, Y. C. Fredholm, G. Jell, N. Lotfibakhshaiesh, *et al*., The effects of strontium-substituted bioactive glasses on osteoblasts and osteoclasts in vitro. *Biomaterials*. **31**(14), 3949–3956 (2010).
6. S. Hesaraki, M. Alizadeh, H. Nazarian, and D. Sharifi, Physico-chemical and in vitro biological evaluation of strontium/calcium silicophosphate glass. *J. Mater. Sci: Mater. Med*. **21**(2), 695–705 (2010).
7. S. M. Salman, S. N. Salama, and H. A. Abo-Mosallam, The role of strontium and potassium on crystallization and bioactivity of Na_2O-CaO-P_2O_5-SiO_2 glasses. *Ceram. Inter.* **38**, 55–63 (2010).
8. S. Pina, P. M. Torres, F. Goetz-Neunhoeffer, J. Neubauer, and J. M. F. Ferreira, Newly developed Sr-substituted a-TCP bone cements. *Acta. Biomater.* **6**, 928–935 (2010).
9. H. Yan, K. Zhang, C. F. Blanford, L. F. Francis, and A. Stein, In Vitro Hydroxycarbonate Apatite Mineralization of $CaO-SiO_2$ Sol−Gel Glasses with a Three-Dimensionally Ordered Macroporous Structure. *Chem. Mater.* **13**, 1374–1382 (2001).

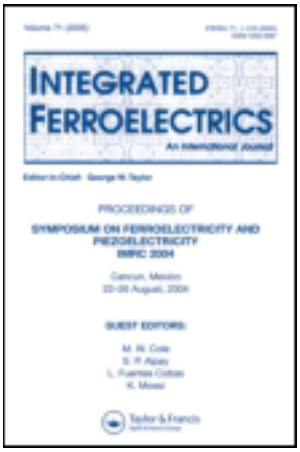

Integrated Ferroelectrics: An International Journal

Publication details, including instructions for authors and subscription information:
http://www.tandfonline.com/loi/ginf20

Fabrication and Magnetic Properties of P_2O_5-CaO-Na_2O Bioactive Glass Ceramic Containing $BaFe_{12}O_{19}$

Pratthana Intawin [a] , Wilaiwan Leenakul [a] , Pongsakorn Jantaratana [c] & Kamonpan Pengpat [a b]

[a] Department of Physics and Materials Science, Faculty of Science , Chiang Mai University , Chiang Mai , 50200 , Thailand

[b] Materials Science Research Center, Faculty of Science , Chiang Mai University , Chiang Mai , 50200 , Thailand

[c] Magnetic Materials Speciality Research Unit, Department of Physics, Faculty of Science , Kasetsart University , Bangkok , 10900 , Thailand

Published online: 07 Dec 2013.

To cite this article: Pratthana Intawin , Wilaiwan Leenakul , Pongsakorn Jantaratana & Kamonpan Pengpat (2013) Fabrication and Magnetic Properties of P_2O_5-CaO-Na_2O Bioactive Glass Ceramic Containing $BaFe_{12}O_{19}$, Integrated Ferroelectrics: An International Journal, 148:1, 171-177, DOI: 10.1080/10584587.2013.852458

To link to this article: http://dx.doi.org/10.1080/10584587.2013.852458

Integrated Ferroelectrics, 148:171–177, 2013

ISSN: 1058-4587 print / 1607-8489 online
DOI: 10.1080/10584587.2013.852458

Taylor & Francis
Taylor & Francis Group

Fabrication and Magnetic Properties of P_2O_5-CaO-Na_2O Bioactive Glass Ceramic Containing $BaFe_{12}O_{19}$

PRATTHANA INTAWIN,[1] WILAIWAN LEENAKUL,[1] PONGSAKORN JANTARATANA,[3] AND KAMONPAN PENGPAT[1,2,*]

[1]Department of Physics and Materials Science, Faculty of Science, Chiang Mai University, Chiang Mai 50200, Thailand
[2]Materials Science Research Center, Faculty of Science, Chiang Mai University, Chiang Mai 50200, Thailand
[3]Magnetic Materials Speciality Research Unit, Department of Physics, Faculty of Science, Kasetsart University, Bangkok 10900, Thailand

The fabrication of bioactive glass ceramics containing $BaFe_{12}O_{19}$ (BF) crystals has been carried out for the application in hyperthermia treatment. The $BaFe_{12}O_{19}$ powder was firstly prepared and subsequently mixed with the non-silicate P_2O_5-CaO-Na_2O bioactive glass with various BF concentrations. After that, the glass ceramics were produced via a sintering method at 600°C and their crystal phases were examined by XRD and in vitro test was carried out by soaking in simulated body fluid. Remanence and saturation magnetization and coercivity were deduced from magnetic measurement. It was found that the samples exhibited magnetic behavior which is similar to hard magnetic materials.

Keywords Ferrimagnetic; hyperthermia treatment; non-silicate bioglasses; sintering; glass-ceramic method

1. Introduction

Non-silicate glasses of the CaO-P_2O_5 system have a potential use as bone substituting applications, because their chemical composition is closely similar to that of natural bone. They have bioresorbable property which enables these glasses to be dissolved in physical fluids. The implant glass can be slowly replaced by regenerated tissue and has good biocompatibility and non-toxicity [1–2]. Recently, development of bioactive glass-ceramic containing magnetic properties has received much attention as thermoseed in hyperthermia treatment of cancer, especially effective in treating the deep seated tumors [3–4]. When granular seeds of glass-ceramics are implanted around tumors and then subjected to alternating magnetic fields, heat is generated from magnetic loss killing the tumors.

Received December 9, 2012; in final form August 25, 2013.
*Corresponding author. E-mail: kamonpan.p@cmu.ac.th

Several materials that generate heat by hysteresis loss and contain bioactivity behavior have been investigated. Singh et al. [8-9] showed the structural and magnetic properties of ferrimagnetic bioglass ceramics in the system [0.45(CaO,P_2O_5)(0.52-x)SiO_2 x$Fe_2O_3$0.03Na_2O], x = 0.25, 0.05, 0.10, 0.15, 0.20 and heat-treated in the temperature range of 600–1100°C . Moreover Bretcanu et al. prepared ferrimagnetic glass-ceramics with the composition in the SiO_2–Na_2O–CaO–P_2O_5 –FeO–Fe_2O_3 system, as a function of the melting temperature. These materials were obtained by melting of commercial reagents in the temperature range of 1400–1550°C [5–7].

The present work, therefore, attempted to fabricate bioactive glass-ceramics containing Ba-ferrite phase from P_2O_5-CaO-Na_2O system by a modified sintering method. Effects of BF addition on the magnetic properties and bioactivity of the prepared bioglass-ceramics were observed.

2. Experiments

2.1 Preparation of Glass Ceramics

Barium ferrite ($BaFe_{12}O_{19}$: BF) powder was produced by solid-state reaction technique using Fe_2O_3 and $BaCO_3$ as starting materials with a ratio of 6:1. The mixture was ball milled and calcined at 1100°C for 3 h in ambient atmospheric pressure using an electric furnace and a heating rate of 5°C/min.

The reagent grade Na_2CO_3, $CaCO_3$ and $NH_4H_2PO_4$ powders of 40CaO-15Na_2O-45P_2O_5 (in wt.%) bioglass composition were mixed with the calcined barium ferrite ($BaFe_{12}O_{19}$: BF) by 5, 10, 20 and 40 wt.%. The mixtures were then melted at 1000°C for 1 h and quenched between stainless steel plates to form bioglass. The quenched bioglass was ground into fine powder and subsequently dry-pressed into pellets in a steel die at 16 Mpa. The green bodies were sintered at 600 for 2 h in an electric furnace (heating rate 5°C/min).

2.2 Characterization of Glass Ceramics

Differential thermal analysis (DTA) was performed on finely powdered glass using 1600 DTA, Du Pont Instrument with a heating rate of 10°C/min and with alumina as the reference material. The glass transition temperature (T_g) and crystallization temperature (T_x) were identified from the DTA traces. X-ray diffraction (XRD: Siemen D-500) was used to investigate the phase composition of the glass ceramics using a Philips powder diffractometer with CuKα ($\lambda = 1.54178$ Å) radiation. The phases formed were identified by comparing the experimental diffraction patterns with the diffraction database. Magnetic measurements of glass ceramic samples were performed at room temperature. The glass ceramics were investigated using the vibrating sample magnetometer (VSM) at 8 kOe. Hysteresis loops were obtained in terms of M-H curves. The scanning electron microscope (SEM: JSM-6335F) was used to record images of the microstructure of the glass-ceramics and energy dispersive X-ray spectrometer (EDS) was used for compositional analysis of the bulk and of individual features. The glass ceramic samples were investigated for bioactivity by immersing in simulated body fluid (SBF). The SBF was buffered at pH 7.4 and maintained at 37°C for 7 days. After that, the glass ceramic samples were analysed for the apatite formation by using a scanning electron microscope based energy dispersive X-ray spectrometer.

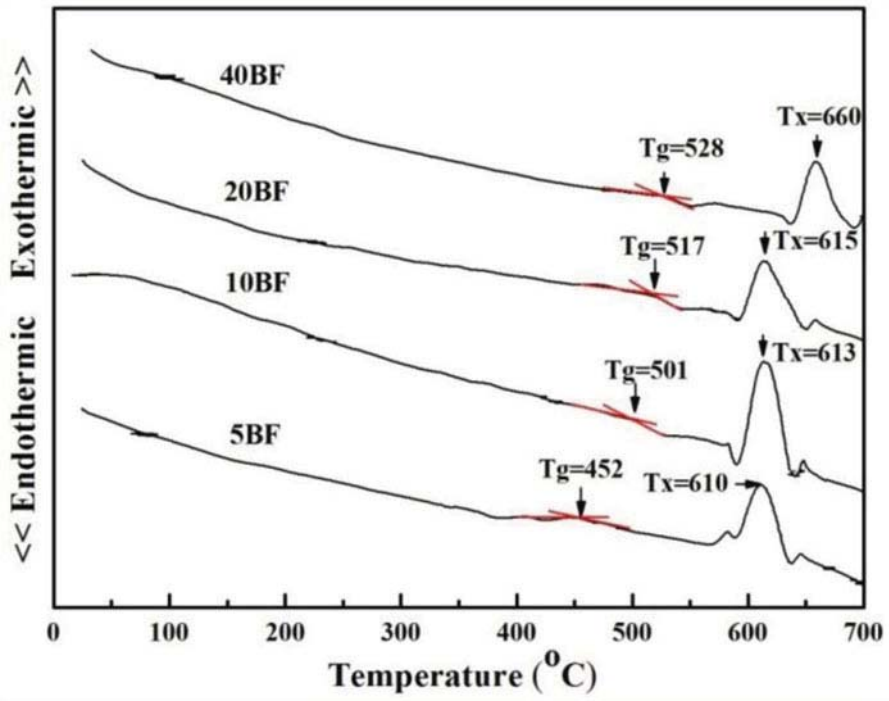

Figure 1. DTA traces. (Color figure available online.)

3. Results and Discussion

3.1 DTA Analysis

The DTA traces of glass samples are shown in Fig. 1 and are annotated with the glass transition temperatures (T_g) and crystallization temperatures (T_x) which are then graphically plotted in Fig. 2. It is shown that both T_g and T_x increase when the level of BF increases from 5 to 40 wt. %. Generally, a change in T_g and T_x with composition reflects a structural evolution in the glass network, and both linear trends observed in this study confirm that the presence of BF in the glass samples only increased the melt viscosity and the crystallization temperature of the glass samples, without affecting the structural continuity of the parent glass matrix.

3.2 XRD Analysis

The phase formation behavior of the samples after sintering process was investigated by XRD. Fig. 3 shows the XRD patterns of glass-ceramic samples with different BF content after sintering at 600°C. The patterns demonstrate the presence of four prominent crystalline phases: barium ferrite ($BaFe_{12}O_{19}$) (JCPDS 27-1029), sodium calcium phosphate ($Na_{1.8}Ca_{1.1}P_6O_{17}$) (JCPDS 47-0863), calcium hydrogen phosphate ($CaH_2P_2O_7$) (JCPDS 51-0200) and calcium phosphate ($Ca_2P_2O_7$)(JCPDS 71-2123). The peak intensity of barium ferrite increases with increasing BF content, indicating an increase in the amount of

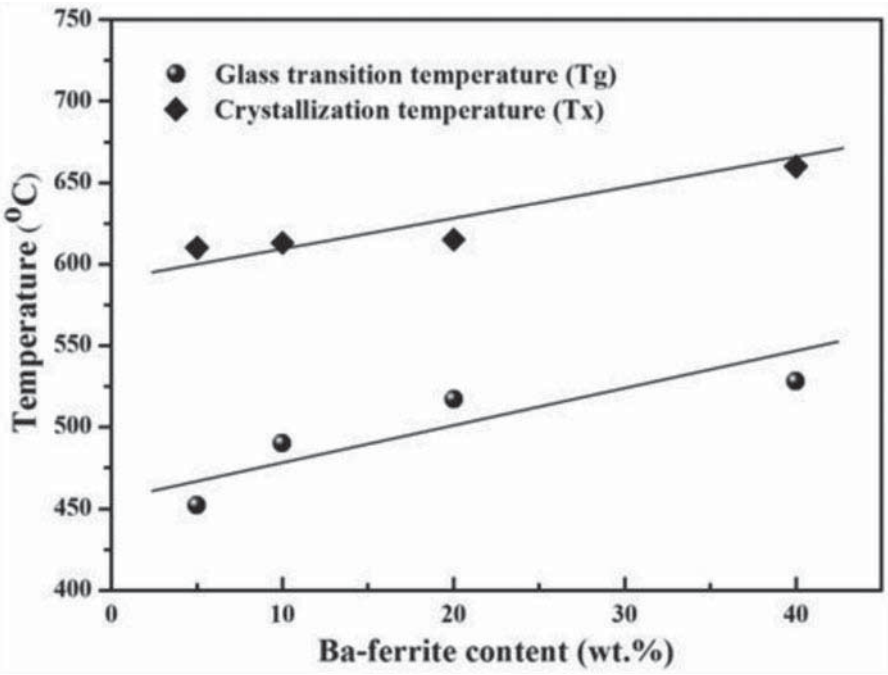

Figure 2. T_g and T_x of quenched glasses versus BF content.

barium ferrite phase in the glass ceramics, which shows its growing crystallization due to the increase of $BaO–Fe_2O_3$ interactions.

3.3 VSM Analysis

The magnetic properties were measured at room temperature using the Vibrating Sample Magnetometer (VSM). The applied magnetic field (H) was swept from 8 to - 8 kOe with both field alignment in-plane and out-plane sample orientation. Fig. 4 shows the VSM hysteresis graphs of glass ceramic samples. It can be found that the remanence magnetization (Mr) and coercivity (Hc) increase with increasing BF content as shown in the insets of Fig. 4. It may be assumed that the number of magnetic domains and hence the saturation magnetization are proportional to the crystallized $BaFe_{12}O_{19}$ content. $BaFe_{12}O_{19}$ is a ferimagnetic phase and contributes to lower the saturation magnetization. Magnetic properties of the materials i.e. remanance magnetization (Mr), saturation magnetization (Ms), coercivity (Hc) and hysteresis area are also listed in Table 1. Crystallization of ferrimagnetic $BaFe_{12}O_{19}$ increases with the increase in BF content. Accordingly, the increase in saturation magnetization is in good agreement with the crystallized $BaFe_{12}O_{19}$ content in the XRD results.

3.4 In Vitro Analysis

Figure 5 shows the SEM micrographs of glass ceramic samples at various BF contents after immersion in SBF for 7 days. It is evident that the surfaces of all samples were covered with spherical Ca-P particles, which can be presumed to be an apatite layer. EDS

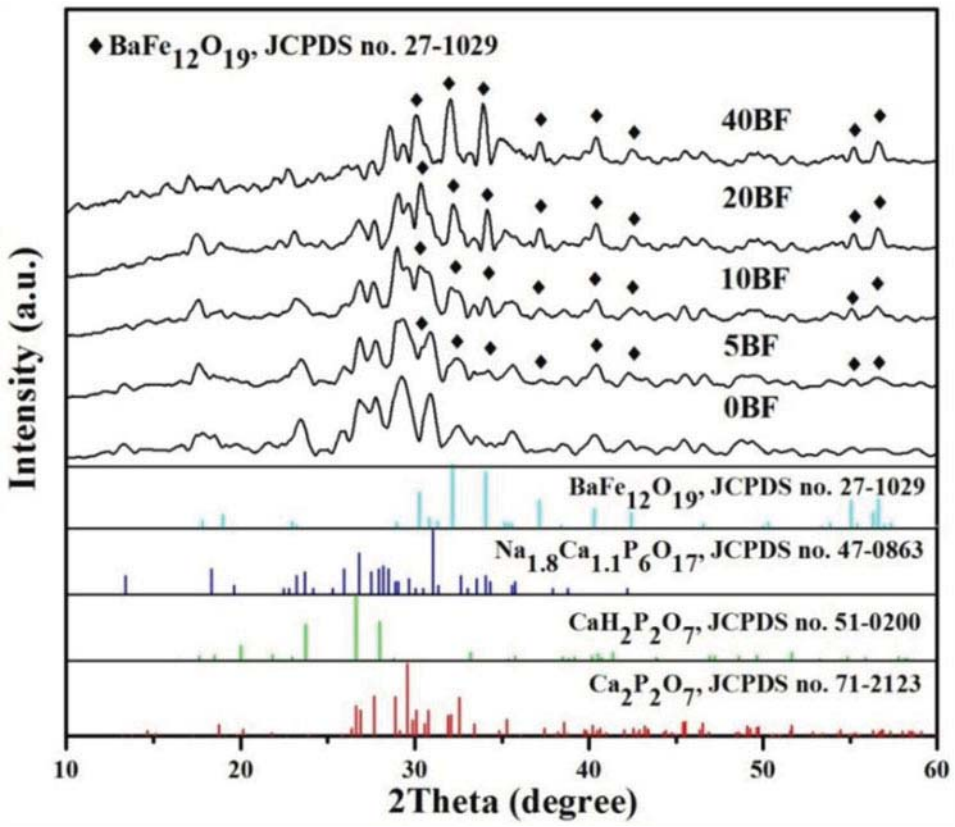

Figure 3. XRD patterns of the glass-ceramic samples sintered at 600°C. (Color figure available online.)

shows the Ca-P concentration changed in SBF during the in vitro assay. The concentration of Ca and P were found to increase with increasing BF content. These changes in ion concentration may be associated with the crystallization of apatite phase. The addition of $BaFe_{12}O_{19}$ to CaO-P_2O_5-Na_2O composition activated the apatite formation on the surface of the glass-ceramics, confirming their bioactivity.

Table 1
Magnetic parameters of glass-ceramics

Magnetic parameters	**5BF**	**10BF**	**20BF**	**40BF**
Saturation magnetization Ms (emu/g)	1.54	3.13	7.7	14.82
Coercive force Hc (Oe)	4386	4466	4545	4641
Remanence magnetization Mr (emu/g)	0.97	1.91	4.8	9.11
Interpolated hysteresis area (erg/g) ± 8 kOe	31467.24	63277.19	152175.65	291241.24

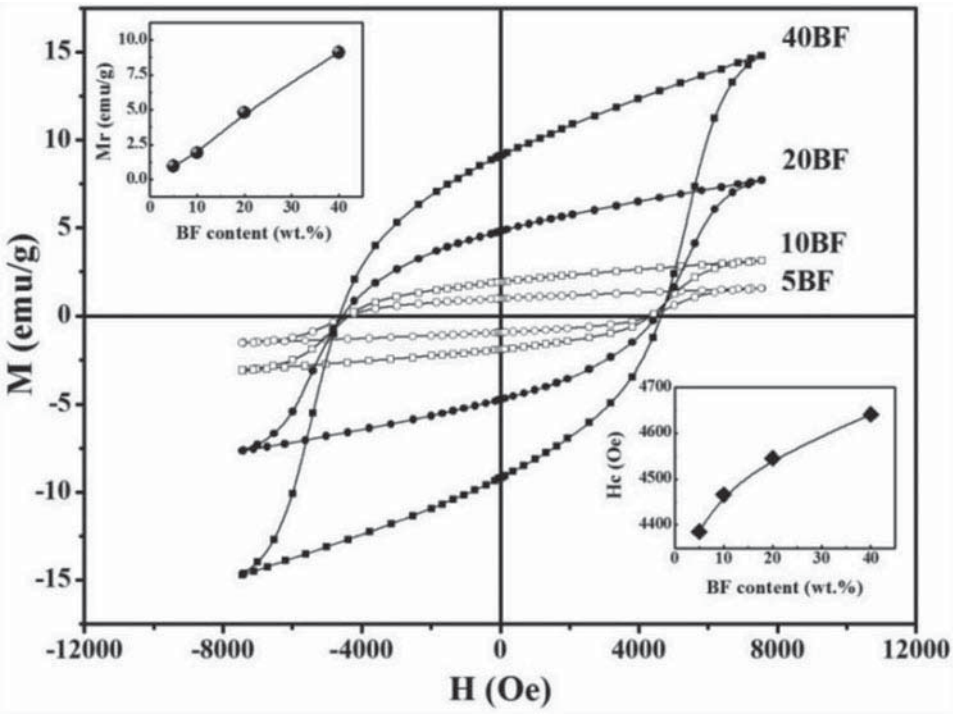

Figure 4. VSM hysteresis loops of samples 5BF, 10BF, 20BF and 40BF at 8 kOe.

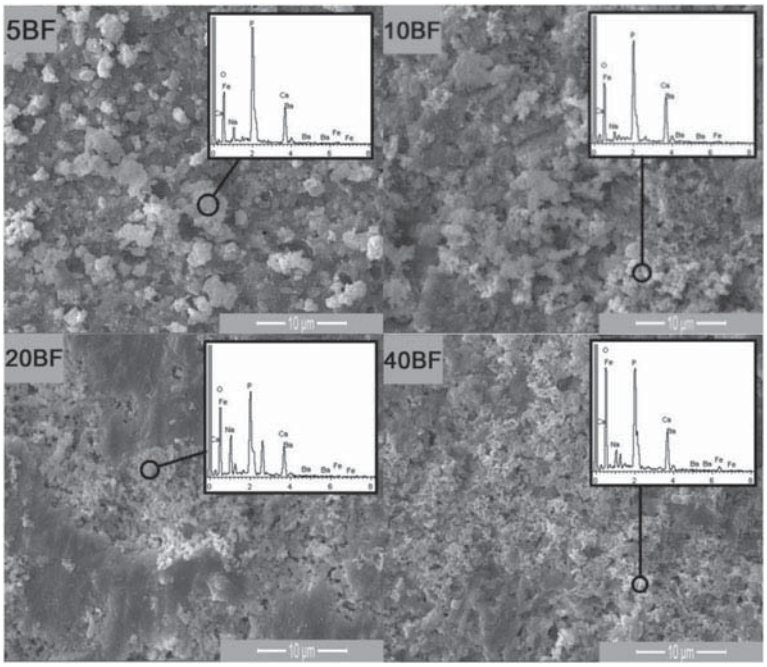

Figure 5. SEM micrographs of glass ceramic samples after 7 days of immersion in SBF

4. Conclusion

Bioactive glass ceramics with barium ferrite content (BF) varied from 5 - 40 wt.% were fabricated. The ($BaFe_{12}O_{19}$), ($Na_{1.8}Ca_{1.1}P6O_{17}$), ($CaH_2P_2O_7$), ($Ca_2P_2O_7$) and ($NaFe(P_2O_7)$) phases were detected in the XRD patterns of the prepared glass-ceramics. Vibrating sample magnetometer (VSM) data at 8 kOe showed that remanence magnetization, coercivity and hence hysteresis area increased with the increase in BF content. In vitro tests have been conducted on the glass ceramics samples by examining their apatite-forming ability in SBF. SEM studies revealed an increase in apatite-forming ability with an increase in BF content in the prepared glass-ceramics.

Acknowledgments

The authors would like to thank the Thailand Research Fund (TRF), National Metal and Materials Technology Center (MTEC), the National Research University (NRU) and Faculty of Science, Chiang Mai University, Thailand for financial support. P. Intawin would like to express her thanks to financial support from the Graduate School, Chiang Mai University.

References

1. Z. M. Da Cost, W. M. Pontuschka, J. M. Giehl, and C. R. Da Costa, ESR dosimeter based on P_2O_5-CaO-Na_2O glass system. *J. Non-Cryst. Solids*. **352**(32–35), 3663–3667 (2008).
2. D. Carta, J. C. Knowles, M. E. Smith, and R. J. Newport, Synthesis and structural characterization of P_2O_5-CaO-Na_2O sol-gel materials. *J. Non-Cryst. Solids*. **353**(11–12), 1141–1149 (2007).
3. P. Wust, B. Hildebrandt, G. Sreenivasa, B. Rau, J. Gellermann, H. Riess, R. Felix, P. M. Schlag, Hyperthermia in combined treatment of cancer. *Lancet Oncol*. **3**(8), 487–497 (2002).
4. A. Dupraz, T. P. Nguyen, M. Richard, *et al*., Influence of a cellulosic ether carrier on the structure of biphasic calcium phosphate ceramic particles in an injectable composite material. *Biomaterials*. **20**(7), 663–673 (1999).
5. O. Bretcanu, S. Spriano, E. Verne, M. Coisson, P. Tiberto, P. Allia, and P. Acta, The influence of crystallised Fe3O4 on the magnetic properties of coprecipitation-derived ferrimagnetic glass–ceramics. *Biomaterials*. **1**(4), 421–429 (2005).
6. O. Bretcanu, E. Verne, M. Coisson, P. Tiberto, and P. Allia, Temperature effect on the magnetic properties of the coprecipitation derived ferrimagnetic glass-ceramics. *J. Magn. Magn. Mater.* **300**(2), 412–417 (2006).
7. O. Bretcanu, E. Verne, M. Coisson, P. Tiberto, P. Allia, Magnetic properties of the ferrimagnetic glass-ceramics for hyperthermia. *J. Magn. Magn. Mater.* **305**(2), 529–533 (2006).
8. R. K Singh and A. Srinivasan, Apatite-forming ability and magnetic properties of glass-ceramics containing zinc ferrite and calcium sodium phosphate phases. *Mat. Sci. Eng. C-Biomim.* **30**(8), 1100–1106 (2010).
9. R. K Singh, A. Srinivasan, EPR and magnetic properties of MgO–CaO–SiO_2–P_2O_5–CaF_2–Fe_2O_3 glass-ceramics. *J. Magn. Magn. Mater.* **312**(18), 2749–2752 (2009).

Ferroelectrics
Publication details, including instructions for authors and subscription information:
http://www.tandfonline.com/loi/gfer20

Effect of Zn^{2+} and Nb^{5+} Co-Doping on Electrical Properties of BCZT Ceramics by the Seed-Induced Method

Piewpan Parjansri [a] , Kamonpan Pengpat [a] , Gobwute Rujijanagul [a] , Tawee Tunkasiri [a] , Uraiwan Intatha [b] & Sukum Eitssayeam [a]

[a] Department of Physics and Materials Science, Faculty of Science , Chiang Mai University , Chiang Mai , 50200 , Thailand

[b] School of Science , Mae Fah Luang University , Chiang Rai , 57100 , Thailand

Published online: 17 Jan 2014.

To cite this article: Piewpan Parjansri , Kamonpan Pengpat , Gobwute Rujijanagul , Tawee Tunkasiri , Uraiwan Intatha & Sukum Eitssayeam (2014) Effect of Zn^{2+} and Nb^{5+} Co-Doping on Electrical Properties of BCZT Ceramics by the Seed-Induced Method, Ferroelectrics, 458:1, 91-97, DOI: 10.1080/00150193.2013.850015

To link to this article: http://dx.doi.org/10.1080/00150193.2013.850015

Ferroelectrics, 458:91–97, 2014

ISSN: 0015-0193 print / 1563-5112 online
DOI: 10.1080/00150193.2013.850015

Taylor & Francis
Taylor & Francis Group

Effect of Zn^{2+} and Nb^{5+} Co-Doping on Electrical Properties of BCZT Ceramics by the Seed-Induced Method

PIEWPAN PARJANSRI,[1] KAMONPAN PENGPAT,[1] GOBWUTE RUJIJANAGUL,[1] TAWEE TUNKASIRI,[1] URAIWAN INTATHA,[2] AND SUKUM EITSSAYEAM[1,*]

[1]Department of Physics and Materials Science, Faculty of Science, Chiang Mai University, Chiang Mai 50200, Thailand
[2]School of Science, Mae Fah Luang University, Chiang Rai 57100, Thailand

The effects of Zn^{2+} and Nb^{5+} co-doping (x mol%ZN) on the electrical properties of lead-free $Ba_{0.90}Ca_{0.10}Zr_{0.10}Ti_{0.90}O_3$-Seed ceramic systems, where x = 0.0–1.0 mol% have been studied. The ceramics were prepared using the solid state reaction technique. The phase of the samples showed pure perovskite structure. The density values of the ceramics were in the range of 4.86–5.78 g/cm^3. The maximum dielectric constant was 40893 for 0.8 mol% ZN. The highest values of $P_r \sim 5.85$ μC/cm^2, $d_{33} \sim 381$ pC/N and $k_p \sim 38\%$ were obtained for the sample of 0.4 mol% ZN.

Keywords Lead free ceramics; phase formation; piezoelectric properties; perovskite structure

1. Introduction

In recent years, lead-free materials have received considerable attention because of their good piezoelectric properties and high curie temperatures and they have great potential for use in piezoelectric devices [1–3]. Work on lead free materials has been focused on modified $BaTiO_3$-base ceramics because of the phase transition temperature of BT which can be modified by A-site or B-site substitutions such as by the addition of calcium (Ca) into the barium (Ba) site or zirconium (Zr) into the titanium (Ti) site [4]. Lead free $(Ba_{1-x}Ca_x)(Zr_yTi_{1-y})O_3$ (BCZT) ceramic is one of the modified barium titanates which attracts considerable attention because of its high piezoelectric properties, good dielectric properties and large tunability [5–6]. From previous reports, these properties are found for $Ba_{0.85}Ca_{0.15}Zr_{0.1}Ti_{0.9}$ and it can be easily sintered because no volatile composition exists for this system [5–6]. However, these ceramics require very high calcining and sintering temperatures of about 1300–1350 °C and 1500–1540 °C, respectively for forming pure perovskite phase. Recently, the doping of various elements in BCZT ceramics (such as CeO or ZnO) has been widely reported due to their denser microstructure with lower calcining and sintering temperatures which results in improved electrical properties [7–8]. In addition, the Nb_2O_5 doping was reported to help promote domain wall motion, enhancing

Received December 11, 2012; in final form March 14, 2013.
*Corresponding authors. E-mail: sukum99@yahoo.com, sukum99@me.com

the densification and resistivity of piezoelectric ceramics [9–10]. However, BCZT doped with ZnO and Nb_2O_5 co-doping has not been reported. In the present work, we studied the effect of $Zn^{2+}$and Nb^{5+} co-doping on the properties of $Ba_{0.9}Ca_{0.1}Zr_{0.1}Ti_{0.9}$ ceramic systems by seed-induced method. Using seed compound to induce formation of the perovskite phase at low temperature because the energetic barrier of phase formation was decreased [11].

2. Experimental

$Ba_{0.9}Ca_{0.1}Zr_{0.1}Ti_{0.9}O_3$ (BCZT)-Seed ceramics doped with x mol% of Zn^{2+} and Nb^{5+} were prepared by the solid state reaction technique. BCZT seed was synthesized from $Ba_{0.9}Ca_{0.1}Zr_{0.1}Ti_{0.9}O_3$ powder by the molten-salt route. Reagent grade metal oxide powders were ball-mill for 24 h in ethanol with zirconia grinding media. The powders were then mixed with KCl-NaCl salt (1:1) and calcined at 1000°C for 2 h.

The powders were then washed with hot deionized water and dried in an oven at 120°C. Then, 5 mol% of the BCZT seed powders were mixed with BCZT and x mol% of Zn-Nb (x = 0.0, 0.2, 0.4, 0.6, 0.8 and 1.0). The slurry was dried and calcined in crucibles at 1200°C for 2 h. The dried powders were then mixed with organic binder (3 wt% PVA) and pressed into cylindrical pellets 10 mm in diameter and 1 mm in thickness using a force of 1 ton. The pellets were sintered at 1400°C for 2 h (after the PVA binder was burned out at 500°C for 1 h). Phase formation and microstructure of the samples was studied via X-ray diffraction (XRD) and scanning electron microscopy (SEM). For electrical properties characterization, the sintered ceramics were ground to obtain parallel faces and the faces were then coated with silver as electrodes. The dielectric constants and dielectric loss of the sintered ceramics were measured as a function of frequency and temperature with an automated dielectric measurement system. The ferroelectric properties were measured using a Sawyer Tower circuit. The electrode specimens were poled in a silicone oil bath at 28°C by applying a DC field of 3 kV/mm for 30 min. Then, the poled samples were characterized for piezoelectric properties using a KCF S5865 d_{33} meter. The electromechanical coupling coefficient k_p of poled samples was investigated by a resonance and anti-resonance method with using an impedance analyzer.

3. Results and Discussions

The XRD patterns of the ceramic samples as a function of x mol% Zn-Nb for BCZT-seed ceramics are illustrated in Fig. 1(a). The samples exhibited pure perovskite phase for all conditions. All samples exhibited coexistence between the orthorhombic phase and tetragonal phase. The existence of tetragonal phase in ceramics is confirmed by the splitting of the (002)/(200) peaks at 2θ of 44–46° [5, 12–13]. Fig. 1(b) shows grain size and density values of the samples. It was observed that as the ZN content increased from 0.0–0.4 mol% the grain size increased. As the ZN content increased from 0.6 to 1.0 mol% it was found that the grain size decreased. The sample of 0.4 mol% ZN showed the largest grain size of 13.5 μm. (Grain size was measured by the line intercept method from SEM micrographs). The increasing grain size was found to have an effect on the density of ceramics. However, for these conditions there is very little change in density value.

Figure 2 indicates the dielectric constant (a) and dielectric loss values (b) as a function of frequency at room temperature. The graph is expanded for the frequency range of 1–100 kHz (as shown in Fig. 2(a1) and (b1)). The results show that the dielectric constant (ε_r) and dielectric loss (tan δ) values of samples at 0.0–0.6 mol% ZN change with frequency

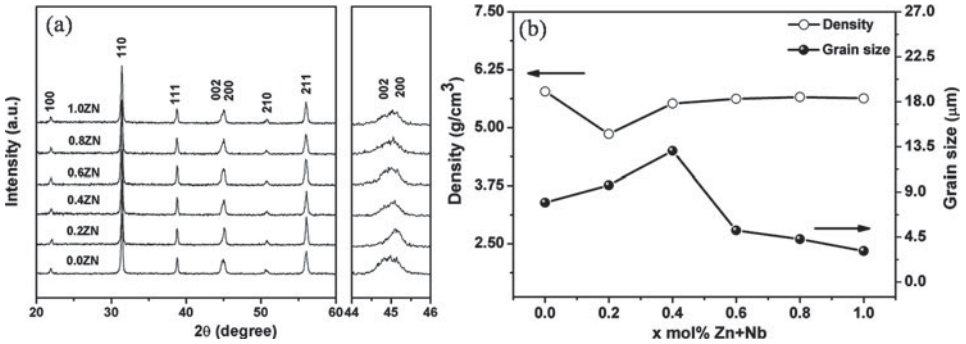

Figure 1. (a) XRD diffraction patterns and (b) density and grain size values of the sintered BCZT-seed-mol% ZN ceramic samples.

and significantly change with ZN content of 0.8–1.0 mol%. The ε_r of ceramic were in the range of 1500–45000 (measured at 1 kHz) with the highest value found for 0.8 mol% ZN content. The high dielectric constant can be due to the densification and mechanisms of domain wall mobility when Zn-Nb dope the ceramics [14]. Dielectric loss for ceramics showed significant change with frequency because the concentration of charge carriers was not constant [15].

Moreover, the tan δ values in the frequency range of 1–100 kHz were less than 0.04 for the samples of 0.0–0.6 mol%ZN.

The relationship between dielectric properties and temperature is displayed in Fig. 3. From the figure, the ceramics exhibit two phase transitions corresponding to the orthorhombic-tetragonal ($T_{O\text{-}T}$) at ~50 °C and tetragonal-cubic (T_c) phase transitions were observed for the samples with mol% ZN = 0.0–0.4 [12]. With increased ZN content

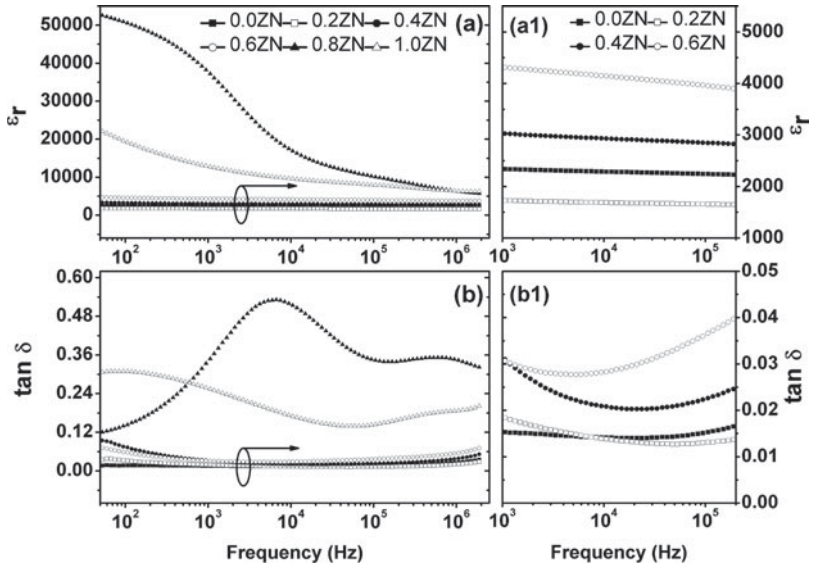

Figure 2. Dielectric constant (a) and dielectric loss (b) as a function of frequency at room temperature.

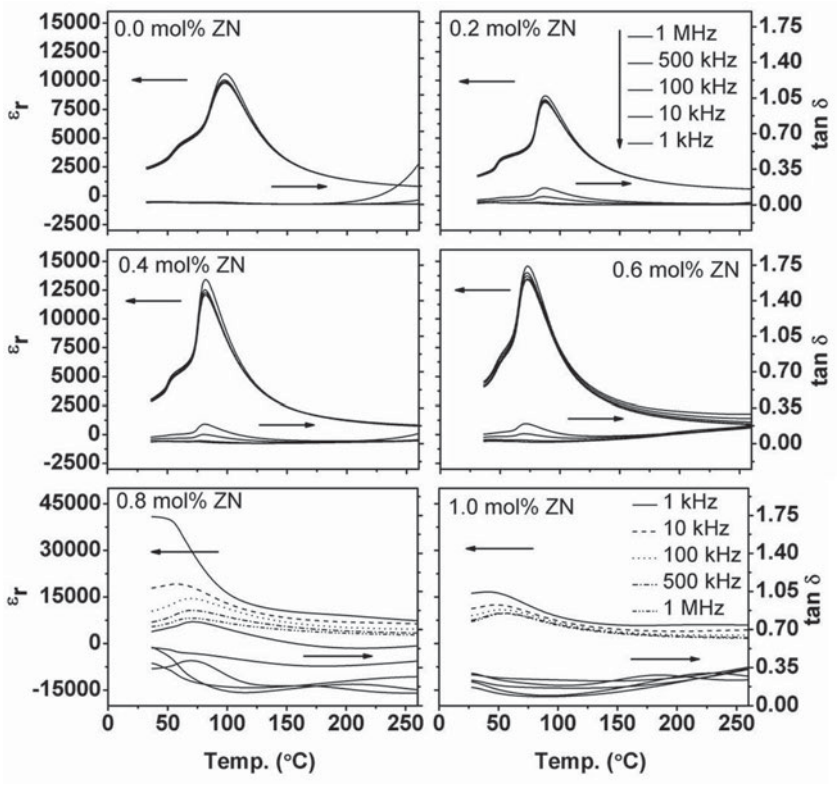

Figure 3. Dielectric constant (ε_r) and dielectric loss (tan δ) as a function of temperature and frequency for BCZT-seed-x mol% ZN ceramic samples.

(ZN = 0.8–1.0 mol%) the transition of orthorhombic to tetragonal phase at room temperature was not observed. The tetragonal-cubic (T_c) phase transitions temperature was reduced from 100°C to 40°C with increased ZN content. These results suggest that the Curie temperature decreased because the substitutions of Zn^{2+} and Nb^{5+} ions lead to deformation of the ABO_3 lattice [5]. Thus, the increasing ZN content had an effect on the phase formation from tetragonal to cubic phase at lower temperatures [7]. Also, the dielectric peak at T_c becomes broader with temperature for samples of 0.8–1.0 mol% ZN which may be the diffuseness of the phase transition in BCZT ceramics [16]. In addition, the maximum dielectric constant (dielectric constant at T_c) tended to increase with increase of ZN content from 0.0–0.8 mol% ZN and then decrease at 1.0 mol% ZN. The highest dielectric constant of 40893 was found for the 0.8 mol% ZN sample. The dielectric loss shows similar behavior as the dielectric constant behavior. Hence ZN co-doping improved the dielectric properties of BCZT ceramics.

The samples of 0.0–0.6 mol% ZN content were selected for investigation of the ferroelectric and piezoelectric properties because these samples exhibited low dielectric loss at 1 kHz (lower than 0.03). The hysteresis loops (P-E loop) of the samples for 0.0–0.6 mol% ZN are shown in Fig. 4(a). It can be seen that all samples indicated ferroelectric behavior with a slim loop. The remanent polarization (P_r) of the ceramics tended to increase with increasing ZN content (as shown in Fig. 4(b)). Maximum $P_r \sim 5.85\ \mu C/cm^2$ was obtained for sample with 0.4 mol% ZN and the coercive field (E_c) value decreased with increasing

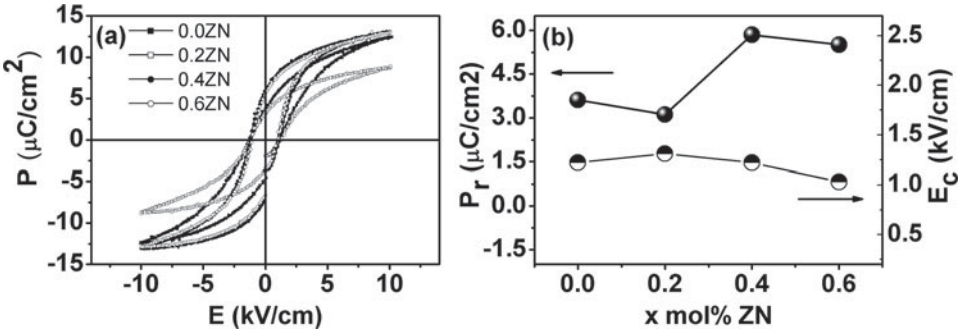

Figure 4. (a) Polarization vs electric field hysteresis loops and (b) P_r and E_c values for BCZT-seed-mol% ZN ceramic samples.

ZN content. The decrease of E_c for ceramics may be because the Nb^{5+} doped BCZT can promote domain wall motion in ceramics [10]. The 0.4 mol% ZN sample showed highest P_r which suggests that this sample should have better piezoelectric properties [17]. Fig. 5 illustrates the piezoelectric coefficient d_{33}, voltage piezoelectric coefficient g_{33} and planar mode electromechanical coupling coefficient k_p of ceramics as a function of mol% ZN. The coefficient g_{33} was calculated by the equation [18]. It can be observed that ZN co-doping has a large effect on the d_{33}, k_p and g_{33} values.

The value of d_{33} and k_p tended to increase with increased ZN content for 0.0–0.4 mol% and then decrease for sample of 0.6 mol% ZN (maximum values of d_{33} and k_p were 381 pC/N and 38%, respectively). The value of g_{33} increases from 10×10^{-3} Vm/N for 0.0 mol% ZN to 23×10^{-3} Vm/N for 0.2 mol% ZN and then gradually decreased with increasing ZN content. The highest values of d_{33} and k_p for BCZT ceramics may be attributed to the coexistence of orthorhombic phase and tetragonal phase near room temperature [5, 19]. The large P_r and low E_c values for sample of 0.4 mol% ZN may result in enhanced piezoelectric properties because these values indicate improvement of the poling process [20]. Moreover, it was found that the piezoelectric properties were associated with grain size of BCZT ceramics. The decreased d_{33} and k_p values of 0.6 mol% ZN may be due to the decreased domain size (grain size decreases) which constrain the movement of the domain walls in polarization process [21].

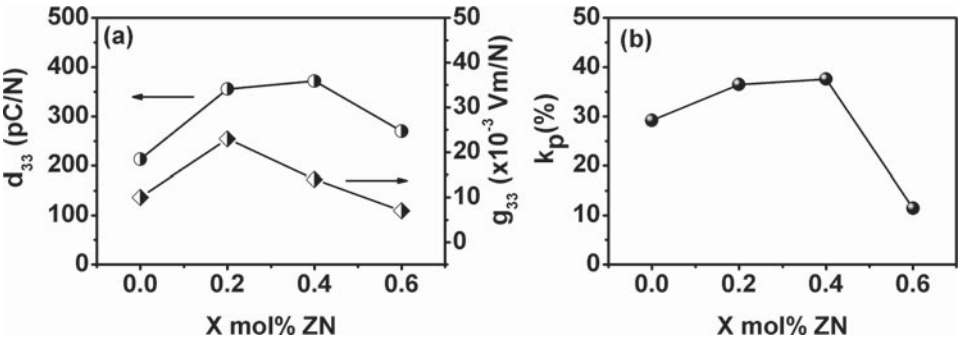

Figure 5. (a) Piezoelectric coefficient (d_{33}), piezoelectric voltage coefficient (g_{33}) and (b) electromechanical coupling coefficient (k_p) for BCZT-seed-mol% ZN ceramics.

4. Conclusion

The effect of Zn-Nb co-doping on the electrical properties of BCZT ceramics produced by seed-induce method were investigated. It was found that the seed induce method reduced the calcination temperature to a lower temperature (by ∼100–150°C). All ceramics indicated existence of orthorhombic phase and tetragonal phase. The ZN co-doping demonstrated enhancement of the dielectric constant ($\varepsilon_{max} \sim 40893$). The highest values of $P_r \sim 5.85\ \mu C/cm^2$, $d_{33} \sim 381$ pC/N and $k_p \sim 38\%$ were obtained for the sample of 0.4 mol% ZN.

Acknowledgments

The authors would like to thank the Thailand Research Fund (TRF) for financial support, including the support given through the Royal Golden Jubilee Ph.D. Program, Office of the Higher Education Commission, Thailand, National Metal and Materials Technology center (MTEC), Faculty of Science Chiang Mai University, and Graduate School Chiang Mai University.

References

1. R. C. Chang, C. Yuan, Y. P. Wong, Y. F. Lin, and C. S. Hong, Properties of $(Na_{0.5}K_{0.5})NbO_3$–$SrTiO_3$ based lead-free ceramics and surface acoustic wave devices. *Sensors and Actuators*. *A* **136**, 267–272 (2007).
2. J. Yoo, J. Hong, H. Lee, Y. Jeong, B. Lee, H. Song, and J. Kwon, Piezoelectric and dielectric properties of La_2O_3 added $Bi(Na,K)TiO_3$–$SrTiO_3$ ceramics for pressure sensor application. *Sensors and Actuators*. *A* **126**, 41–47 (2006).
3. D. Wu, B. Xiao, B. Wu, W. Wu, J. Zhu, Z. Yang, and J. Wang, Sintering temperature induced electrical properties of $(Ba_{0.90}Ca_{0.10})(Ti_{0.85}Zr_{0.15})O_3$ lead-free ceramics. *Mater Res Bull*. **47**, 1281–1284 (2012).
4. O. P. Thakur, C. Prakash, and A. R. James, Enhanced dielectric properties in modified barium titanate ceramics through improved processing. *J Alloys Compd*. **470**, 548–551 (2009).
5. W. Liu and X. Ren, Large piezoelectric effect in Pb-free ceramics. *Phys Rev Lett*. **103**, 257602–4 (2009).
6. P. Wang, Y. Li, and Y. Lu, Enhanced piezoelectric properties of $(Ba_{0.85}Ca_{0.15})(Ti_{0.9}Zr_{0.1})O_3$ lead-free ceramics by optimizing calcinations and sintering temperature. *J Eur Ceram Soc*. **31**, 2005–2012 (2011).
7. Y. Cui, X. Liu, M. Jiang, X. Zhao, X. Shan, W. Li, C. Yuan, and C. Zhou, Lead-free $(Ba_{0.85}Ca_{0.15})(Ti_{0.9}Zr_{0.1})O_3$–$CeO_2$ ceramics with high piezoelectric coefficient obtained by low-temperature sintering. *Ceram Int*. **38**, 4761–4764 (2012).
8. J. Wu, D. Xiao, W. Wu, Q. Chen, J. Zhu, Z. Yang, and J. Wang, Role of room-temperature phase transition in the electrical properties of (Ba, Ca)(Ti, Zr)O_3 ceramics. *Scripta Mater.* **65**, 771–774 (2011).
9. H. Zheng, I. M. Reaney, W. E. Lee, N. Jones, and H. Thomas, Effect on strontrium substitution in Nb-doped PZT ceramics. *J Eur Ceram Soc*. **21**, 1371–1378 (2001).
10. M. Pereira, A. G. Peixoto, and M. J. M. Gomes, Effect of Nb on the microstructural and electrical properties of PZT ceramic. *J Eur Ceram Soc*. **21**, 1353–1356 (2001).
11. Z. Li, A. Wu, and P. M. Vilarinho, Perovskite phase stabilization of $Pb(Zn_{1/3}Ta_{2/3})O_3$ ceramics induced by $PbTiO_3$ seeds. *Chem Mater.* **16**, 717–723 (2004).
12. W. Li, Z. J. Xu, R. Q. Chu, P. Fu, and G. Z. Zang, High piezoelectric d_{33} coefficient in $(Ba_{1-x}Ca_x)(Ti_{0.98}Zr_{0.02})O_3$ lead-free ceramics with relative high Curie temperature. *Mater Lett*. **64**, 2325–2327 (2010).

13. P. Z. Zhang, M. R. Shen, L. Fang, F. G. Zhang, X. L. Wu, J. C. Shen, and H. T. Chen, Pr^{3+}photoluminescence in ferroelectric $(Ba_{0.77}Ca_{0.23})TiO_3$ ceramics: sensitive to polarization and phase transitions. *Appl Phys Lett*. **92**(22), 222908 (2008).
14. A. Banerjee, A. Bandyopadhyay, and S Bose, Influence of La_2O_3, SrO, and ZnO addition on PZT. *J Am Ceram Soc*. **89**(5), 1594–1600 (2006).
15. U. Intatha, S. Eitssyeam, J. Wang, and T. Tunkasiri, Impedance study of giant dielectric permittivity in BaFe0.5Nb0.5O3 perovskite ceramics. *Curr Appl Phys*. **10**, 21–25 (2010).
16. W. Li, Z. Xu, R. Chu, P. Fu, and G. Zang, Structural and dielectric properties in the $(Ba_{1-x}Ca_x)(Ti_{0.95}Zr_{0.05})O_3$ ceramics, *Curr Appl Phys*. **12**, 748–751 (2012).
17. P. Parjansri, S. Inthong, K. Sutjarittangtham, G. Rujijanagul, T. Tunkasiri, U. Intatha, P. Pengpad, and S. Eitssayeam, Effects of B-site doping on piezoelectric and ferroelectric properties of $Pb_{0.88}Sr_{0.12}(Zr_{0.54}Ti_{0.44}Sb0.02)_{(1-y)}$–$(Zn_{1/3}Nb_{2/3})_yO_3$ ceramics, *Ferroelectrics*. **415**, 29–34 (2011).
18. A. J. Moulson and J. M. Herbert, *Electroceramics Materials, Properties, Applications, second ed*. New York: J. Wiley and Sons, 2003.
19. S Zhang, Ru Xia, T. R. Shrout, G. Zang, and J. Wang: Piezoelectric properties in perovskite $0.948(K_{0.5}Na_{0.5})NbO_3$–$0.052LiSbO_3$ lead-free ceramics. *J Appl Phys*. **100**, 104108–6 (2006).
20. Q. Xu, X. L. Chen, W. Chen, S. T. Chen, B. Kim, and J. Lee, Synthesis, ferroelectric and piezoelectric properties of some $(Na_{0.5}Bi_{0.5})TiO_3$ system compositions. *Mater Lett*. **59**, 2437–2441 (2005).
21. J. Hao, W. Bai, W. Li, and J. Zhai, Correlation between the microstructure and electrical properties in high-performance $(Ba_{0.85}Ca_{0.15})(Zr_{0.1}Ti_{0.9})O_3$ lead-free piezoelectric ceramics. *J Am Ceram Soc*. **95**(6) 1998–2006 (2012).

Ferroelectrics
Publication details, including instructions for authors and subscription information:
http://www.tandfonline.com/loi/gfer20

Preparation of Potassium Sodium Niobate in Tellurite Glass System Doped with Er_2O_3

Ploypailin Yongsiri [a] , Phiangkhwan Mhuangthong [a] , Anocha Munpakdee [b] & Kamonpan Pengpat [a c]

[a] Department of Physics and Materials Science, Faculty of Science , Chiang Mai University , Chiang Mai , 50200 , Thailand

[b] Department of General Science, Faculty of Science , Srinakharinwirot University , Sukhumvit , Bangkok , 10110 , Thailand

[c] Materials Science Research Center, Faculty of Science , Chiang Mai , 50200 , Thailand

Published online: 24 Jan 2014.

To cite this article: Ploypailin Yongsiri , Phiangkhwan Mhuangthong , Anocha Munpakdee & Kamonpan Pengpat (2014) Preparation of Potassium Sodium Niobate in Tellurite Glass System Doped with Er_2O_3 , Ferroelectrics, 459:1, 153-159, DOI: 10.1080/00150193.2013.849512

To link to this article: http://dx.doi.org/10.1080/00150193.2013.849512

Ferroelectrics, 459:153–159, 2014

ISSN: 0015-0193 print / 1563-5112 online
DOI: 10.1080/00150193.2013.849512

Taylor & Francis
Taylor & Francis Group

Preparation of Potassium Sodium Niobate in Tellurite Glass System Doped with Er_2O_3

PLOYPAILIN YONGSIRI,[1] PHIANGKHWAN MHUANGTHONG,[1] ANOCHA MUNPAKDEE,[2] AND KAMONPAN PENGPAT[1,3,*]

[1]Department of Physics and Materials Science, Faculty of Science, Chiang Mai University, Chiang Mai, 50200, Thailand
[2]Department of General Science, Faculty of Science, Srinakharinwirot University, Sukhumvit, Bangkok, 10110, Thailand
[3]Materials Science Research Center, Faculty of Science, Chiang Mai, 50200, Thailand

In the present study, potassium sodium niobate (KNN) doped with Er_2O_3 in TeO_2 glasses were successfully prepared using melting-quenching method. The glass composition of 70KNN-30TeO_2 mol% doped with 1 mol% of Er_2O_3 has been chosen. A batch was subsequently melted at 800°C and 900°C for 30–60 min and heated at the temperature ranging between 300–530°C in order to form the glass ceramics with desired crystal phases. XRD results showed that KNN crystals distributed over the glass-ceramic samples. From SEM observation, it was found that nano-crystals of several phases were precipitated in all glass-ceramic matrices. Dielectric constant increased with increasing heat treatment temperature.

Keywords Potassium sodium niobate; glass-ceramics; tellurite glass; incorporation method

1. Introduction

Ferroelectric glass-ceramics have been studied extensively as they possesses the properties of non-porous glasses and solid crystals [1–2]. $(K_{0.5}Na_{0.5})NbO_3$: KNN is one of ferroelectric materials and shows an interesting electro-optical property [3–5]. In this study, we have produced the glasses based on this KNN phase using tellurium oxide as a glass former and doped with Er_2O_3 for achieving glasses and glass-ceramics with desired opto-electrical property. Tellurium oxide (TeO_2), one of good glass forming oxides, has a high refractive index ($n > 2$). Its IR transmission range is up to 6 μm and possesses a large third order non-linear optical susceptibility (χ^3) [6–7]. Moreover, many researchers have been interested in glass–ceramics doped with rare earth (RE) ions, such as Er^{3+}, Eu^{3+}, Yb^{3+}, and Pr^{3+}, because these RE ions promoted a good luminescence media via energy transfer which are able to generate an amplifier [8–9].

In this work, KNN-TeO_2 glass-ceramics containing KNN crystals with small amount of (1 mol%) Er_2O_3 were prepared using incorporation method. In the incorporation method,

Received December 11, 2012; in final form March 13, 2013.
*Corresponding author. E-mail: kamonpan.p@cmu.ac.th

a simple mixed-oxide technique was firstly employed to synthesize the KNN single phase powder before mixing with the glass former oxide and dopant of TeO_2 and Er_2O_3, respectively and then the mixture were melted-quenched to form glass. The crystallization of the KNN crystals in the glass was accomplished by heat treatment processes which were also used to control the KNN crystal shape and size. Here, we report the physical, thermal and electrical properties of the prepared KNN glass-ceramics.

2. Experimental

The glass of 30KNN-70TeO_2 (mol%) doped with 1 mol% of Er_2O_3 was prepared using incorporation method. KNN powder was firstly prepared by high purity Na_2CO_3 (Riedel-de Haën, 99.9%), K_2CO_3 (Sigma-Aldrich, 99.9%) and Nb_2O_5 (Sigma-Aldrich, 99.9%) powders. High purity of KNN powder was prepared by excess Na_2CO_3 and K_2CO_3 of 5mol% with ratio 1:1. For incorporation method, the prepare KNN powder was then mixed with the glass forming substance; TeO_2, in order to form transparent glass-ceramics. The components were mixed in a platinum crucible and subsequently melted at 800°C for 30 min (A), 800°C for 60 min (B), 900°C for 30 min (C) and 900°C for 60 min (D) and then quenched between stainless steel plates. The quenched glass was immediately annealed in another electric furnace for 2 hours to release their stress. Thermal properties of as-received glass were measured to find the glass transition temperature (T_g) and crystallization temperature (T_c) by using DTA (differential thermal analysis; Du Pont Instrument, USA). Then, as-received glass was subjected to heat treatment (HT) at temperatures ranging between 300 to 550°C depending upon the T_g and T_c of each glass, for 4 hours. Heating rate of 5°C/min and cooling rate of 10°C/min were employed.

To analyze the glass and glass-ceramic properties, various techniques were employed. XRD (X-ray diffractometer; D500 type, Siemens, UK) and FE-SEM (scanning electron microscope; JSM 6335F type, JEOL, JP) techniques were used to investigate the phase composition and to observe the microstructure of the glass and glass-ceramic samples. The room temperature dielectric constant (ε_r) and dielectric loss (tanδ) of the glass-ceramics were measured at various frequencies from 10 kHz to 1 MHz using a precision LCZ meter (E4980A type, Agilent Technologies, Malaysia).

3. Results and Discussions

3.1. Thermal and Physical Properties

The DTA curves were recorded for the precursor glass powders and the results are shown in Fig. 1. All glass conditions (A-D) exhibits glass transition in the temperature ranging between 375–388°C (T_g) followed by two exothermic peaks around 430°C (T_{c1}) and around 530–540°C (T_{c2}), corresponding to their crystallization. Silica (SiO_2) was used as standard reference and showed the reference peak around 580°C. From the DTA data, the glass thermal stability factor (T_{c1}–T_g) has been determined and it was found that glass A with 30 min dwell time has better stability than that of glass B with 60 min dwell time, both were melted at 800°C. The most stable glass is glass C using the melting temperature and dwell time of 900°C and 30 min, respectively, with the stability factor of approximately 57°C. The glass stability factors of all glass samples are indicated in Fig 1. The high thermal stability factor identifies the ability of glass to form nano-structured glass–ceramics which

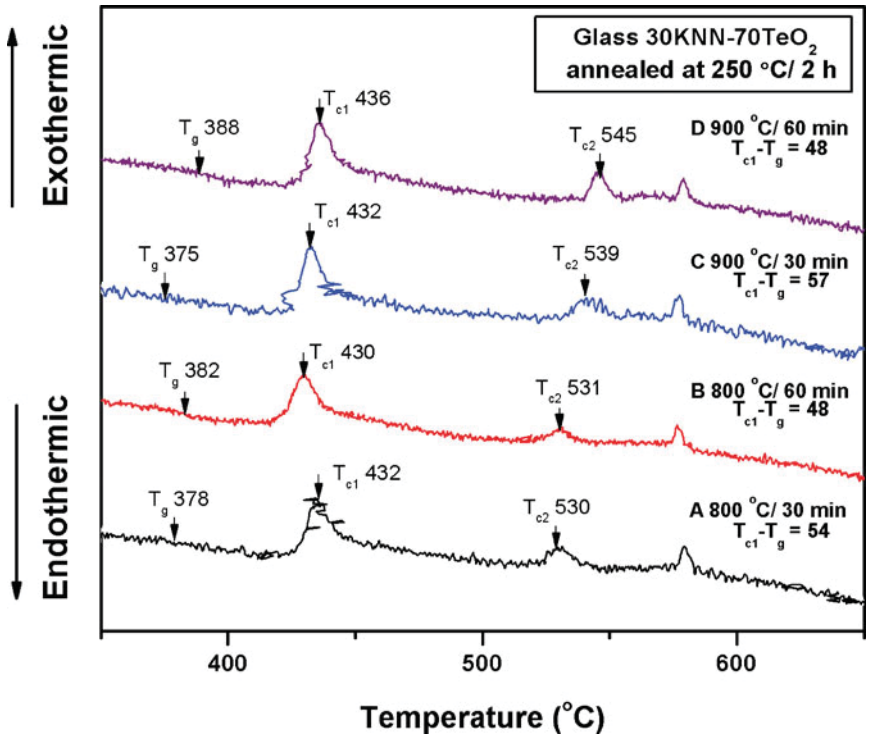

Figure 1. DTA curves of as-received glass powders at two different melting temperatures of 800°C and 900°C and 30 and 60 min dwell times. (Color figure available online.)

can be controlled by heat-treatment process. Then, these glasses were subjected to heat treatment schedules depending on their thermal profiles.

3.2. XRD Characterization

In Fig. 2, the XRD results of the heat treated glass-ceramics contains no KNN; $(K_{0.5}Na_{0.5})NbO_3$ crystal phase. This may be due to two reasons, first, the very low viscosity of telluride glasses at their melting temperatures; 800°C and 900°C, giving rise to compositional fluctuation. Another one is, because the melting temperature of TeO_2 is relatively low (732°C), therefore it is easily evaporated resulted in the slightly change in glass compositions during melting at elevated temperature [11]. The heat treatment temperature also plays an important role in controlling the crystal phase in the glass-ceramics. As-received A. glass sample exhibits amorphous pattern with very small trace of crystalline peaks of cubic KNN phase, while that of other B.-D. glasses contained clearer crystalline peaks of the cubic KNN. When all A.-D. glass samples were heat-treated at 325°C, they exhibit similar crystalline phases, which may be identified as the typical cubic $(K,Na)NbO_3$ phase with random variation of K and Na ions in the A-site of the unit cell [12]. The heat treated samples at T_{c1} and T_{c2} for each glass composition are also illustrated in Fig 3. Glass ceramics heat treated at = 430°C (T_{c1}) contained two other phases apart from the cubic $(K,Na)NbO_3$ phase, which may be identified as $KNbTeO_6$ (•) and TeO_2 (⊙). At T_{c2}, the additional $Na_2Nb_4O_{11}$ (♦) phase was clearly revealed in all glass ceramics, together

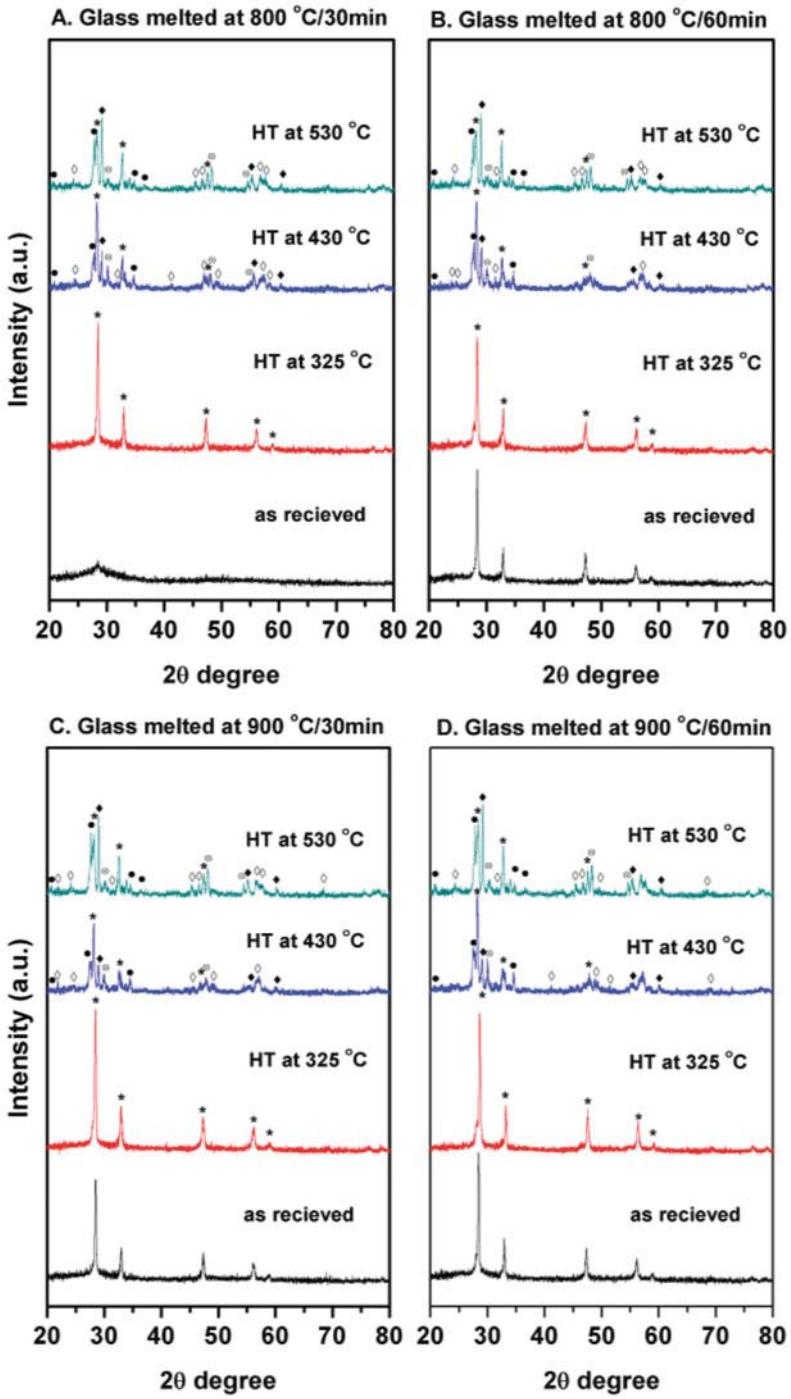

Figure 2. XRD patterns of all glasses and glass-ceramics produced from different conditions. (Color figure available online.)

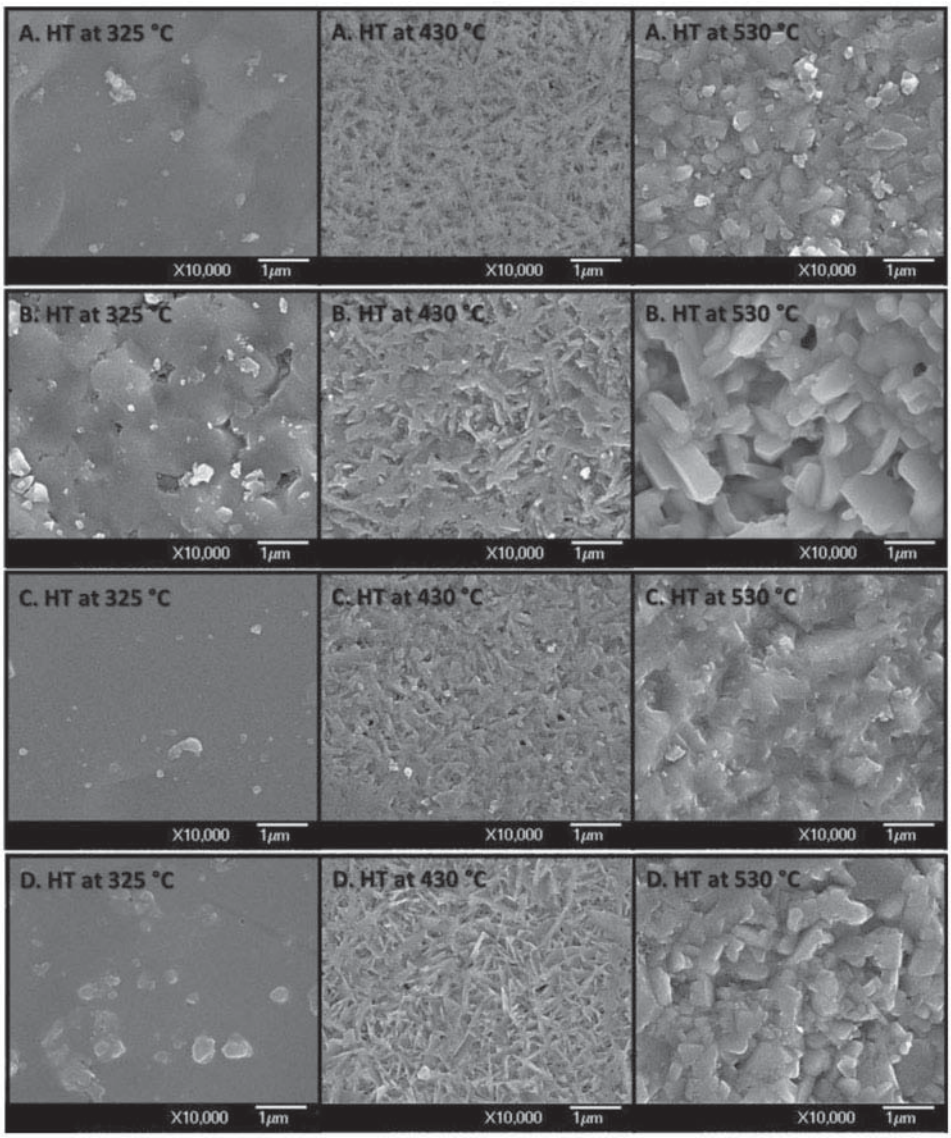

Figure 3. SEM micrographs of heat treated samples.

with two phases of $KNbTeO_6$ (•) and TeO_2 (⊙). It may be assumed that the intensity of glass melted for 60min was not different from glass melted for 30min, meaning that the melting time has slight effect on the crystallization in glass-ceramics. This may be due to the slightly different in stability factors of these glasses which lie between 48–57°C.

3.3. SEM Observation

FE-SEM was used to investigate the morphology and crystallite size in the prepared glass-ceramics as shown in Fig. 3. At lowest heat treatment temperature of 325°C, no crystalline evidence is clearly revealed by using secondary electron image (SEI) mode except in D.

glass. This may be caused by the difference in crystallite size of the cubic (K,Na)NbO_3 phase in this glass-ceramics, however, the careful study such as Scherrer equation should be performed to confirm this assumption. The small bulk crystals of the KNN phase with rectangular shape occurred in all glass-ceramic samples subjected to the heat treatment at 430°C. For higher heat treatment temperature at 530°C, irregular shape of crystals is revealed. The crystals of all samples are homogeneously embedded throughout the glass matrix with random orientations. However, by using SEI mode the atomic contrast between the cubic KNN phase and other co-precipitated phases could not be revealed.

3.4. Dielectrics Property

Figure 4 shows the dielectric properties of the heat treated glass-ceramics at various temperatures. The maximum dielectric constant was found in C. glass ceramic heat treated at T_{c2}, which was as high as 675 at 10 kHz and the dielectric loss was rather low about 0.01. It

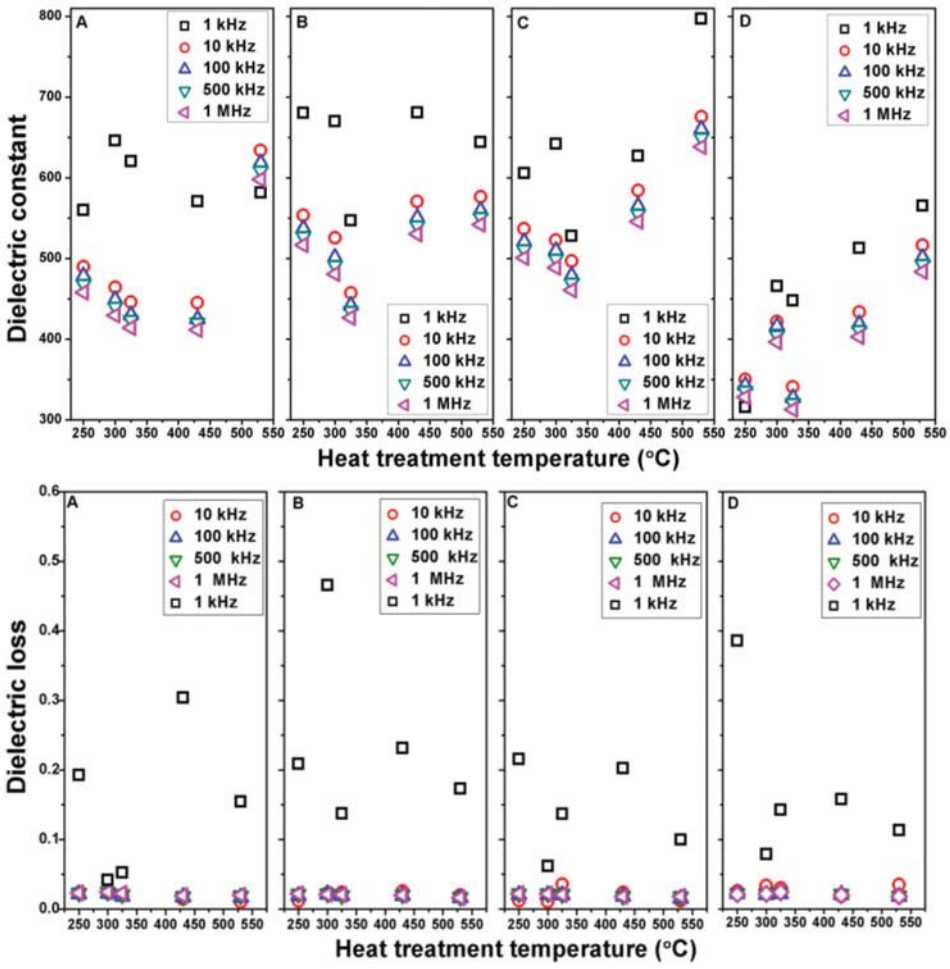

Figure 4. Dielectric constant and dielectric loss of all glass-ceramics at various heat treatment temperatures and frequencies. (Color figure available online.)

can be seen that the dielectric constant decreased when increasing dwell time. This may be due to the fluctuation of glass composition which is evidenced by the difference in stability factor of each glass condition.

4. Conclusion

The ferroelectric glass-ceramics from KNN-TeO_2 doped Er_2O_3 system have been successfully prepared via the incorporation method. The melting temperature and dwell time did not played a significant role for the type of crystalline phase in the glass ceramics. Dielectric properties of these glasses and glass-ceramics are high compared with another KNN containing glass-ceramic system. By the way, these glass ceramics possesses poor mechanical robust and low transparency. The more detail studies in terms of mechanical and optical properties, therefore, are needed in future works.

Acknowledgments

The authors would like to express their sincere gratitude to the Thailand Research Fund, National Metal and Materials Technology Center, and Faculty of Science, Chiang Mai University for financial support. We wish to thank the Graduate School Chiang Mai University and The National Research University Project under Thailand's Office of the Higher Education Commission for financial support. P. Yongsiri would like to thank the Thailand Graduate Institute of Science and Technology for her scholarship.

References

1. N. F. Borrelli, and M. M. Layton, Electroopic properties of transparent ferroelectric glass-ceramic system. *Trans Electron Device*. **6**, 511–514 (1969).
2. H. Jain, Transparent ferroelectric glass-ceramics. *Ferroelectrics*. **306**, 1, 111–127 (2004).
3. L. Egerton, and D. M. Dillon, Piezoelectric and dielectric properties of ceramics in the system potassium-sodium niobate. *J. Am. Ceram. Soc*. **42**, 438–442 (1959).
4. B. Jaffe, W. R. Cook, and H. Jaffe, *Piezoelectric ceramics*. Academic Press. London. JCPDS 71–2171. 1971.
5. P. Yongsiri, S. Eitssayeam, G. Rujijanagul, S. Sirisoonthorn, T. Tunkasiri, and K. Pengpat, Fabrication of transparent lead-free KNN glass-ceramics by incorporation method. *Nanoscale Research Letters*. **7**, 136 (2012).
6. Raouf AH El-Mallawany, *Tellurite glasses handbook: physical properties and data*. USA: CRC Press LLC; 2002.
7. E. D. Jeong, M. G. Ha, H. K. Pak, B. K. Ryu, P. H. Borse, J. S. Lee, T. Komatsu, H. J. Kim, and H. G. Kim, Thermal stabilities, physical and optical properties of K_2O-Na_2O-Nb_2O_5-TeO_2 glasses. *J. Ind. Eng. Chem*. **12**, No 6, 926–931.
8. B. S. Richard, Luminescent layers for enhanced silicon solar cell performance: Down-conversion. *Sol. Energ. Mat. Sol. C*. **90**, 1189–1207 (2006).
9. R. S. Chaliha, K. Annapurna, A. Tarafder, V. S. Tiwari, P. K. Gupta, and B. Karmakar, Optical and dielectric properties of isothermally crystallized nano-KNbO3 in Er^{3+}-doped K_2O-Nb_2O_5-SiO_2 glasses. *Spectrochim Acta A*. **75**, 243–250 (2010).
10. L. M. Sharaf El-Deen, M. S. Al Salhi, and Meawad M. Elkholy, IR and UV spectral studies for rare earths-doped tellurite glasses. *J. Alloy. Compd*. **465**, 333–339 (2008).
11. D. Zhu, C. S. Ray, W. Zhou, and D. E. Day, On glass formation for a Na_2O•4TeO2 melt: Effect of melting temperature, time, and raw material. *J. Mater. Sci*. **39**, 7351–7357 (2004).

Ferroelectrics

Publication details, including instructions for authors and subscription information:
http://www.tandfonline.com/loi/gfer20

Electrical Properties of Calcium Phosphate/BZT Bioglass-Ceramics Prepared by Incorporation Method

Siriporn Tigunta [a] , Nuttapon Pisitpipathsin [a] , Puripat Kantha [b] , Sukum Eitssayeam [a] , Gobwut Rujijanagul [a] , Tawee Tunkasiri [a] & Kamonpan Pengpat [a]

[a] Department of Physics and Materials Science, Faculty of Science , Chiang Mai University , Chiang Mai , 50200 , Thailand

[b] School of Ceramic Engineering, Institute of Engineering , Suranaree University of Technology , Nakhon , Ratchasima , 30000 , Thailand

Published online: 24 Jan 2014.

To cite this article: Siriporn Tigunta , Nuttapon Pisitpipathsin , Puripat Kantha , Sukum Eitssayeam , Gobwut Rujijanagul , Tawee Tunkasiri & Kamonpan Pengpat (2014) Electrical Properties of Calcium Phosphate/BZT Bioglass-Ceramics Prepared by Incorporation Method, Ferroelectrics, 459:1, 188-194, DOI: 10.1080/00150193.2013.849527

To link to this article: http://dx.doi.org/10.1080/00150193.2013.849527

Ferroelectrics, 459:188–194, 2014

ISSN: 0015-0193 print / 1563-5112 online
DOI: 10.1080/00150193.2013.849527

Taylor & Francis
Taylor & Francis Group

Electrical Properties of Calcium Phosphate/BZT Bioglass-Ceramics Prepared by Incorporation Method

SIRIPORN TIGUNTA,[1] NUTTAPON PISITPIPATHSIN,[1] PURIPAT KANTHA,[2] SUKUM EITSSAYEAM,[1] GOBWUT RUJIJANAGUL,[1] TAWEE TUNKASIRI,[1] AND KAMONPAN PENGPAT[1,*]

[1]Department of Physics and Materials Science, Faculty of Science, Chiang Mai University, Chiang Mai 50200, Thailand
[2]School of Ceramic Engineering, Institute of Engineering, Suranaree University of Technology, Nakhon, Ratchasima 30000, Thailand

Electrically active bioglass has received much attention as artificial bone graft material. In this study, the dielectric and piezoelectric properties of calcium phosphate-barium zirconium titanate bioglass-ceramics (CPGs-BZT bioglass-ceramics) were investigated as a function of BZT content. The $BaZr_{0.05}Ti_{0.95}O_3$–$40CaO$-$45P_2O_5$–$15Na_2O$ *bioglass (CPGs/xBZT where x = 0, 10, 20, 30, 40, 50 wt.%) was prepared by an incorporation method. Crystallization temperature of each glass was measured by differential thermal analysis (DTA). XRD and SEM techniques were also used to characterize the phase formation and microstructure. The results showed that the BZT content caused an increase in dielectric and piezoelectric properties. The bioactivity of BZT/CPGs bioglass-ceramics was found to be higher than that of the pure CPGs after soaking in SBF for 14 days.*

Keywords Bioglass; calcium phosphate; barium zirconium titanate; piezoelectric

1. Introduction

In recent years, researchers have paid attention to the development of new types of materials that stimulate a biochemical response from living tissue in order to obtain a strong chemical bond with biological fixation between the prosthesis and surrounding tissues [1,2]. Several glass compositions have been developed which have been revealed to be bioactive as they possess a property that causes the formation of a hydroxyapatite (HA) layer on their surfaces upon immersion in relevant physiological fluids [3]. The groups of materials that exhibit most potential uses are calcium phosphate-based glasses (CPGs), for the reason that they are easily degradable, and their degradation rate can be tailored to suit the end application [4]. Furthermore, CPGs have high potential for using as biomaterials in bone substituting applications and reconstruction of bone as their chemical compositions are closely similar to that of hard tissue, such as bone [5]. They also have good biocompatibility. Moreover,

Received December 11, 2012; in final form March 15, 2013.
*Corresponding author. E-mail: kamonpan.p@cmu.ac.th

they are able to dissolve after time to fill the defect with new bone and without toxicity [6]. The initial network former of these glasses is phosphorous pentoxide (P_2O_5) and sodium oxide (Na_2O) as well as calcium oxide (CaO) as network modifiers [4].

Unfortunately, in various situations, bone substitution by biomaterials has not been completely successful as there is a problem in reconstructive surgery, mainly due to the poor quality of the bone growth around implants [7]. Many researchers have found improvement in osteobonding and bone growth on the surface of polarized hydroxyl apatite (HA) due to the generation of a permanent surface charge on the materials in *vitro*. Nagamura *et al*. [8] found that apatite crystal growth on HA was accelerated by a negatively charged surface. Basset *et al*. [9, 10] independently showed in the sixties that bones produce electrical charges when deformed and found a relationship between piezoelectricity and callus formation. They also proposed that stress-induced bioelectric potentials control both bone cell activity and the orientation of their molecular bioproduct. Some research has attempted to combine the bioactive properties of HA with a piezoelectric and high permittivity ferroelectric material, such as $BaTiO_3$. Feng *et al*. [11] prepared HA–$BaTiO_3$ composites, which promoted osteogenesis in the jawbones of dogs. No reaction phases between the two phases were observed from X-ray diffraction analysis and the composites exhibited a d_{33} piezoelectric charge coefficient of 6 pC/N. There was, however, no indication of the precise composition of the composites. N. Pisitpipathsin *et al*. [12] studied HA-$BaZr_{0.05}Ti_{0.95}O_3$ composites, and found that the bioactivity of the HA composites was improved with 10 wt.% $BaZr_{0.05}Ti_{0.95}O_3$ after soaking in simulated body fluid (SBF) for 14 days.

In this work, the physical and electrical properties and biocompatibility of 40CaO-$45P_2O_5$–$15Na_2O$-x $BaZr_{0.05}Ti_{0.95}O_3$ bioglasses for orthopedic applications have been investigated by the addition of $BaZr_{0.05}Ti_{0.95}O_3$ in 40CaO-$45P_2O_5$–$15Na_2O$ bioglass, where x ranged from 0 to 50 wt.%. The electric and biocompatibility of the prepared BZT/CPGs bioglass-ceramic samples were also investigated.

2. Experimental Procedure

Calcium phosphate glasses (CPGs) with the weight composition of $45P_2O_5$–40CaO-$15Na_2O$ were prepared from $(NH_4)_2HPO_4$, $CaCO_3$ and Na_2O powders by conventional melt quenching method. The starting materials were mixed together and melted in alumina crucibles at 1000°C for 1 h. The melt was quickly poured into water for quenching and then the quenched CPGs were ground. Subsequently, barium zirconium titanate ($Ba(Zr_{0.05}Ti_{0.95})O_3$, BZT) powder was added to the prepared CPGs powder at 0, 10, 20, 30, 40, 50 wt.% and melted at 1000°C for 0.5 h. The melted CPGs-BZT bioglasses were placed onto a stainless-steel plate which had been preheated to 450°C and quickly pressed by another stainless steel plate. After that, the CPGs-BZT bioglass were placed back into the furnace for annealing at 450°C for 8 h. Differential thermal analysis (Stanton Redcroft DTA model 673-4) was used to find the proper heat treatment temperatures for crystallization in order to change the bioglasses into bioglass-ceramics. The CPGs-BZT bioglasses were subjected to heat treatment schedule at 550°C (according to the DTA result) for 2 h and cut into samples with the size of 5 × 5 × 1.5 mm. The respective bioglass-ceramic samples were denoted as G0BZT, G10BZT, G20BZT, G30BZT, G40BZT, and G50BZT following the added wt.% BZT content.

The microstructures of all CPGs-BZT bioglass-ceramics were observed by a scanning electron microscope (SEM) equipped with an energy dispersive X-ray analyzer (EDX). All

bioglass-ceramic surfaces were sputter coated with gold for electrical contacts. Micrographs were used to study the distribution of BZT particles and morphology of the phases occurring in each bioglass-ceramic. To identify the crystalline phases that precipitated during the heat treatment, the CPGs-BZT bioglass-ceramics were ground and analyzed using an X-ray diffractometer (XRD) with CuKα (1.54Å) radiation. The data were recorded over the 2Θ range of 20° to 60°. The X-ray diffraction patterns were identified according to standard JCPDS card to monitor the peak positions and their corresponding intensity data. The bioactivity of CPGs-BZT bioglass-ceramics was studied by soaking the bioglasses samples in approximate 15 ml of simulated body fluid (SBF). The SBF solution had ion concentrations and pH nearly equal to those of human blood plasma. The glass samples were immersed in SBF solution for 14 days at 37±0.5°C.

3. Results and Discussions

Phase formation study of CPGs-BZT bioglass-ceramics after being subjected to heat treatment at 550°C was carried out by X-Ray Diffraction. It can be noted that the samples subjected to heat treatment above 550°C were deformed. Therefore, in this work, we show only the result of the samples heat treated at 550°C. The XRD patterns of all bioglass-ceramics are presented in Figure 1. It can be seen that, using the same heat treatment temperature of 550°C, the resulting samples exhibited fully crystalline, partly crystalline and non-crystalline structure depending on their compositions. The bioglasses having lower BZT content (G0BZT, G10BZT, G20BZT) contained calcium phosphate phase of $Ca_2P_2O_7$ (JCDPS File no. 073-0440) and barium titanium zirconium oxide phase (JCDPS File No.

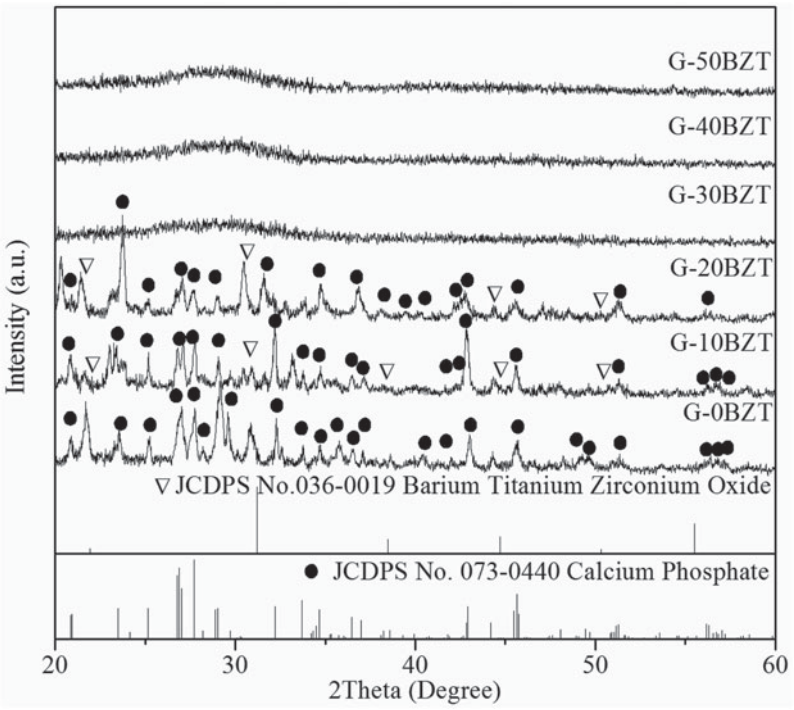

Figure 1. The XRD patterns of all CPGs-BZT bioglass-ceramic samples.

Table 1
Density, porosity, microhardness, glass crystalline temperature (T_c) and piezoelectric coefficient (d_{33}) of CPGs-BZT bioglass

Sample	Density (g cm^{-3})	Porosity (%)	Micro hardness (GPa)	Crystallization temperature (°C)	Piezoelectric coefficient (d_{33})
G0BZT	2.676	1.676	3.717	625	23
G10BZT	2.834	3.329	6.047	643	33
G20BZT	2.971	0.459	16.001	652	31
G30BZT	3.199	0.092	18.330	722	29
G40BZT	3.463	0.091	12.744	723	29
G50BZT	3.050	0.996	7.697	725	21

036–0019), while the bioglasses with high BZT content (G30BZT, G40BZT, G50BZT) remained mainly amorphous.

It is generally accepted that the controlled heat treatment of glasses above the glass transition temperature (T_g) and crystallization temperature (T_c) leads to the transformation of the glasses into their corresponding polycrystalline glass-ceramics. The thermal heat treatment of calcium phosphate glasses results in the release of stresses from the glasses and the possible formation of crystalline phase along with the residual glassy phase [13]. The crystalline temperatures (T_c) deduced from the DTA analysis are presented in Table 1.

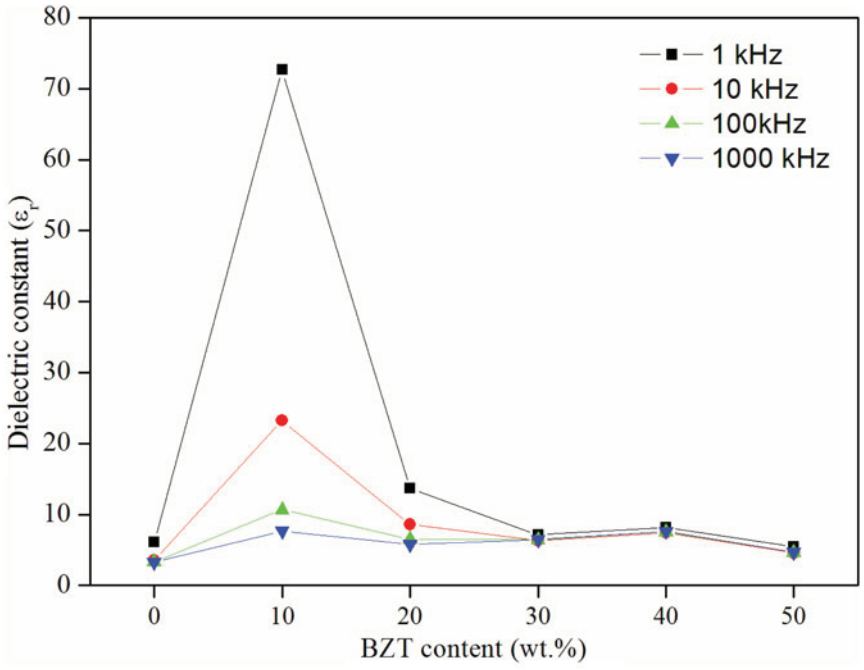

Figure 2. Room temperature dielectric constant (ε_r) vs BZT content at various frequencies from 1 kHz to 1000 kHz. (Color figure available online.)

The T_c(s) of the CPGs range from 625–725°C. Therefore, the amorphous like XRD patterns of the high BZT content from 30–50 wt.% were obtained at a low heat treatment temperature (550°C), as they have higher T_c than those of low BZT content samples.

The density of CPGs-BZT bioglass-ceramics varied from 2.676 gcm^{-3} to 3.463 gcm^{-3}, while the porosity between 0.091 and 3.329% as shown in Table 1. The density of CPGs-BZT samples increased with increasing BZT content up to 40 wt.% and then decreased at 50 wt.%. It was observed that addition of BZT resulted in creation of ionic

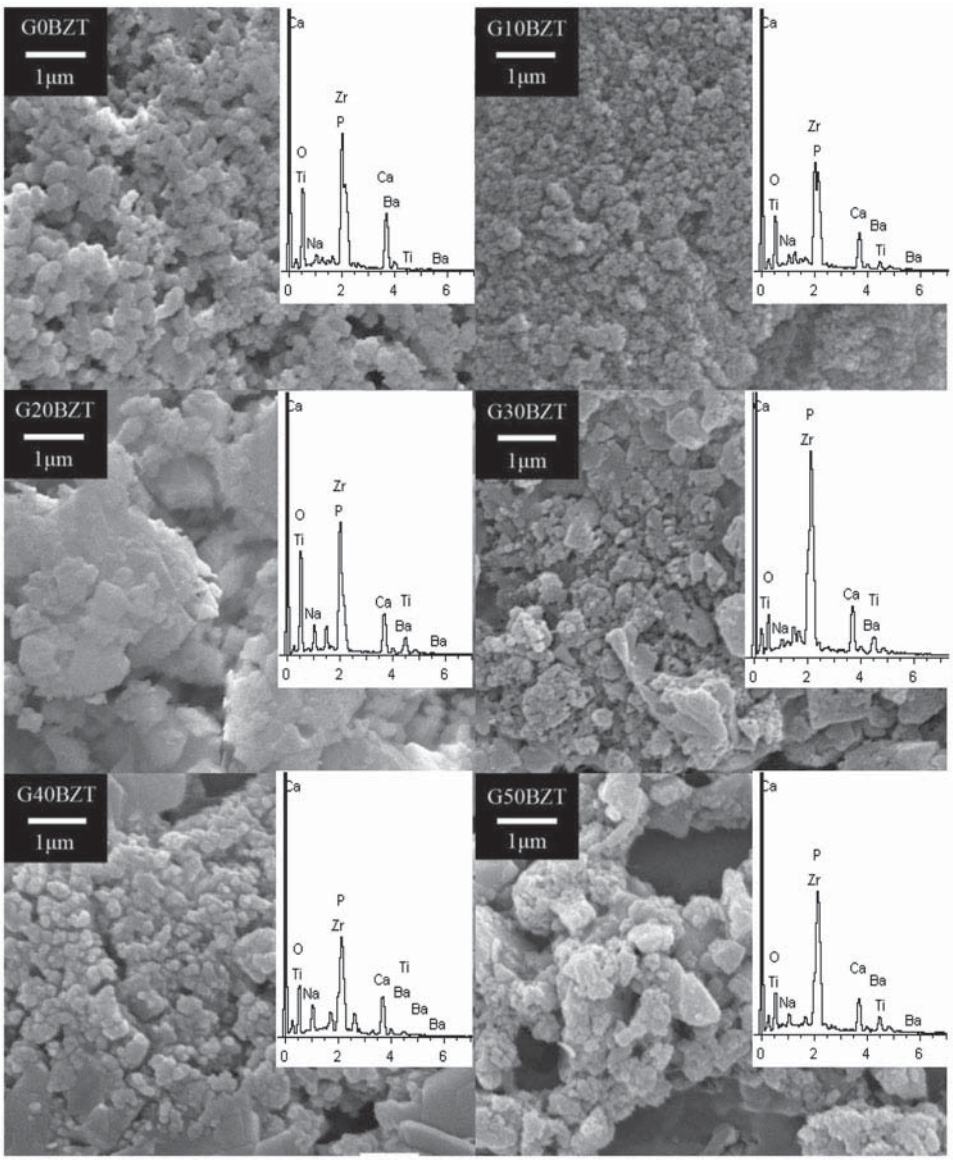

Figure 3. SEM micrographs of CPGs-BZT bioglasses after immersion in stimulated body fluid (SBF) for 14 days. (original magnification: ×10000)

cross linking between non-bridging oxygen of two different phosphate chains. The maximum density was observed for G40BZT sample which also possessed the lowest porosity. The microhardness value varied from 3.717 to 18.330 GPa as presented in Table 1. The maximum microhardness of CPGs-BZT bioglass-ceramic samples can be observed for G30BZT bioglass. As expected, high values of piezoelectric coefficient (d_{33}) were obtained from these CPGs-BZT samples with a range of 21–33 pC/N, compared to other previous work.

Figure 2 shows the room temperature dielectric constant (ε_r) at various frequencies from 1 kHz to 1000 kHz and BZT contents. The highest dielectric constant was obtained for the G10BZT sample at all frequencies. This sample also possesses the highest value of d_{33} (33 pC/N). Moreover, it can be seen that the higher BZT content samples (G30BZT to G50BZT) have low values of dielectric constant. This may be due to the amorphous nature of these samples with no trace of ferroelectric BZT crystals as confirmed by the XRD result.

The scanning electron micrographs of all CPGs-BZT bioglass-ceramics after immersed in stimulated body fluid (SBF) for 14 days are illustrated in Fig. 3. SEM observation revealed a layer of hydroxyl-carbonated apatite on the surfaces of all CPGs-BZT bioglasses and greatest for G10BZT sample, confirmed by the EDS analysis with highest Ca/P ratio in the inset of Fig. 3. It may be assumed that the 10BZT sample possesses the optimum amount of BZT in this bioglass-ceramic series, as it shows bioactivity, appropriate dielectric constant and the d_{33} value of about 33 pC/N.

4. Conclusion

Biocompatible piezoelectric 40CaO-45P_2O_5–15Na_2O-x$BaZr_{0.05}Ti_{0.95}O_3$ bioglasses for orthopedic applications have been produced by addition of $BaZr_{0.05}Ti_{0.95}O_3$ in 40CaO-45P_2O_5–15Na_2O bioglass, where x ranges from 0 to 50 wt.%. The results showed that the main phases identified from XRD analysis were $Ca_2P_2O_7$ and Ba(Zr,Ti)O_3. In terms of biocompatibility, all of the CPGs-BZT bioglass-ceramics revealed good bioactivity by in-vitro evaluation in SBF due to the formation of apatite-like layers at the reaction surface. Biocompatibility of bioglasses can be controlled by optimizing the design of bioglass composition and BZT phase. The addition of 10 wt.%BZT resulted in optimum in this study.

Acknowledgments

The authors would like to express their sincere gratitude to the Thailand Research Fund (TRF), the Royal Golden Jubilee Ph.D. Program, the Graduate School and Faculty of Science, Chiang Mai University, Thailand for their financial supports. We wish to thank the National Research University Project under Thailand's Office of the Higher Education Commission for financial support.

References

1. W. Liang, M. N. Rahaman, D. E. Day, N. W. Marion, G. C. Riley, and J. J. Mao, Bioactive borate glass scaffold for bone tissue engineering. Non-Crystal. *Solids*. **A 354**, 1690–1696 (2008).
2. C. R. Mariappan, D. M. Yunos, A. R. Boccaccini, and B. Roling, Bioactivity of electro-thermally poled bioactive silicate glass. *Acta Biomaterial*. **A 5**(4), 1274–1283 (2009).
3. S. R. Moosvi, and R. M. Day, Bioactive glass modulation of intestinal epithelial cell restitution. Acta Bio-materials. **A 5**(1), 76–83 (2009).

4. I. Ahmed, M. P. Lewis, S. N. Nazhat, and J. C. Knowles, Quantification of anion and cation release from a range of ternary phosphate-based glasses with fixed 45 mol% P_2O_5. *Biomaterials Applications*. **A 20**, (2005).
5. T. Kasuga, Bioactive calcium pyrophosphate glasses and glass-ceramics. *Acta Biomaterial*. **A 1**, 55–64 (2005).
6. A. A. El-Kheshen, F. A. Khaliafa, E. A. Saad, and R. L. Elwan, Effect of Al_2O_3 addition on bioactivity, thermal and mechanical properties of some bioactive glasses. *Ceramics International*. **A 34**, 1667–1673 (2008).
7. B. Miara, E. Rohan, M. Zidic, and B. Labat, Piezomaterial for bone regeneration design-homogenization approach. *The Mechanics and Physics of Solid*. **A 53**, 2529–2556 (2005).
8. S. Nakamura, T. Kobayashi, and K Yamachita: Enhanced osteobonding by negative surface charges of electrically polarized hydroxyapatite. *Biomedical Materials Research*. **A 57**, 477–484 (2001).
9. C. A. L. Basset, Review: biological significance of piezoelectricity. *Calcified Tissue Research*. **A 1**, 252–272 (1968).
10. C. A. L. Basset, R. J. Pawluk, and R. O. Becker: Effects of electrical current in bone in vivo. *Nature*. **A 204**, 652–654 (1965).
11. J. Q. Feng, H. P. Yuan, and X. D. Zhang, Promotion of osteogenesis by a piezoelectric biological ceramic. *Biomaterials*. **A 18**(23), 1531–1534 (1997).
12. N. Pisitpipathsin, P. Kantha, W. Leenakul, P. Sriprapa, K. Pengpat, S. Eitssayeam, and G. Rujijanagul, Effect of $BaZr_{0.05}Ti_{0.95}O_3$ addition on microstructure and piezoelectric properties of Hydroxyapatite bone. *Advanced materials research*. **A 56**, 166–169 (2012).
13. H. A. El-Batal, E. M. A. Khalil, and Y. M. Hamdy, In vitro behavior of bioactive phosphate glass–ceramics from the system P_2O_5–Na_2O–CaO containing titania. *Ceramics International*. **A 35**, 1195–1204 (2008).

Chiang Mai J. Sci. 2014; 41(1) : 213-223
http://epg.science.cmu.ac.th/ejournal/
Contributed Paper

Fabrication of Natural Tapioca Starch Fibers by a Modified Electrospinning Technique

Krit Sutjarittangtham [a], Patthanakorn Jaiturong [b], Uriwan Intatha [c], Kamonpan Pengpat [a], Sukum Eitssayeam*[a] and Jakkapan Sirithunyalug [b]

[a] Department of Physics and Materials Science, Faculty of Science, Chiang Mai University, Chiang Mai 50200, Thailand.

[b] Department of Pharmaceutical Science, Faculty of Pharmacy, Chiang Mai University, Chiang Mai 50200, Thailand.

[c] School of Science, Mae Fah Luang University, Chiang Rai 57100, Thailand.

*Author for correspondence; e-mail: sukum99@yahoo.com

Received: 13 October 2012
Accepted: 19 March 2013

ABSTRACT

We report the fabrication of high purity natural tapioca starch (NTS) fibers by using a modified electrospinning technique with a dehydration process using a -20°C ethanol collector bath to complement the conventional electrospinning technique. Electrospun fibers with diameters of 1.3-14.5 μm were generated from a simple solution of starch in deionized water with starting concentrations of 3.0 to 5.0 wt%. X-ray diffraction and FTIR analyses were employed to study the phase and functional groups occurring in the prepared NTS fibers. X-ray diffraction revealed an A crystalline type structure of the starting NTS and FTIR confirmed that the functional group of the NTS electrospun fibers remained unchanged, indicating unmodified NTS fiber products. The water swelling ratio was 148 % for the electrospun NTS at solution concentration of 4.5 wt% and 78% for 3 wt%. It has been found that using NTS fiber as a disintegrating excipient in tablet form for pharmaceutical applications w*as* not comparable with a superdisintegrant. However, by using a combination of NTS powders and NTS fibers, in particular in lower percentages, there were good results, with a disintegrating time of about one and half minute. These fibers were found to enhance swelling which shows that this fiber is a promising candidate for drug release applications.

Keywords: electrospinning, tapioca starch, electrospun fibers, starch fibers

1. INTRODUCTION

Natural starch has been compounded with other polymers to produce modified fibers using the electrospinning technique for applications in the field of controlled drug release [1]. These starches are biodegradable polymers with excellent biocompatibility and non-toxicity but often present difficulty when being formed. Additional polymers, for example synthetic polymers of Poly(lactide); PLA, Poly(caprolactone); PCL and Poly(vinyl alcohol); PVA or natural polymers of chitosan and alginate, are added to starch solutions to

improve the forming properties [1]. The need for high purity natural starch fibers without any additional added polymers requires the use of an improved electrospinning technique. In this modified process, a simple starch in deionized water solution is modified by use of an ethanol bath collector at -20°C.

In general, starch is the main energy storage resource for all higher plants and has gained much attention as a naturally occurring constituent of biodegradable thermoplastic materials [1-2]. Such materials are known as natural biopolymers, and have been widely used for the entrapment of food ingredients, fillers, binders, and disintegrants in the pharmaceutical field as they are cost effective, non-toxic, biodegradable, edible, and can be metabolized by the human body [1-3].

Two main components of biopolymers are amylose and amylopectin [4]. Three crystal structures (A, B, C) have been described, depending on the starch region and the type of processing of the starch products [4]. Differences between these polymorphs are found in the hydrogen-bonding pattern, the water content, and in the conformation of the polysaccharide chain. A-starches are usually found in grains while B-starches are found in tuberous plants. C-starches are rarer and found mainly in a few plant sources including the pea. Single helical V-type structures have also been observed when amylose crystals are prepared from complexes [4].

Starches and their derivatives play an important role in drug delivery as a form of adjuvants in tablet and capsule formulation [5]. In recent years, polymers based on starches have shown potential applications in matrix construction, such as matrix tablets for drug delivery applications and have been used widely because of the simple and low-cost manufacturing process [6, 7].

Natural tapioca starch (NTS) is of particular interest among commercial starches due to a lower amylase content than most starches, low levels of residual materials and high molecular weights of amylose and amylopectin which enable this starch to be directly used as a native starch substitute in industrial applications as well as a starting material for physical and chemical modification [8]. The use of tapioca starch is also of much interest in Thailand since Thailand is one of the world leaders in tapioca product exports.

The electrospinning technique is composed of two distinct process, electrospray and spinning (electro + spinning), which can produce fibers on the microscale to the nanoscale from a wide range of natural and synthetic polymers [9]. For the basic electrospinning set up, a high electric field is applied to droplets of a polymer solution (or melt), coming out from the tip of a die, which acts as one of the electrodes. The theory is based on the assumption that when a high voltage, usually in a range of 1 to 30 kV, is applied to the polymer melt or solution, it will experience two major types of electrostatic and coulombic forces. The first electrostatic force originates from the repulsion between the surface charges while the second is generated by an external electric field [9-10]. These electrostatic interactions cause the droplet to accelerate, undergo jet bending instability and split into micro or nanofibers as a non-woven mat on the grounded collector [9-12]. It has been found that microfibrous and nanofibrous structures from the electrospinning technique possess large surface area to volume ratios [13].

The initially generated mats then need to be separated and structured using an electrospinning technique to generate processed fibers which have modified properties including different diameters, composition, structure, morphology and

orientation depending on the fiber spinning method [14]. Modification of the setup for electrospinning can be done in by modifying the collector and spinneret. Reneker et al. produced a fluffy columnar network of fibers called a "garland", which slowly moved in large loops and long curves and provided relatively uniform mats [14-16]. Ultra-thin fibers with high productivity were successfully fabricated using an array of multiple hollow needles as the spinneret as reported by Chu et al. [14, 17]. Many researchers have used spinnerets consisting of two coaxial capillaries, resulting in electrospun composite nanofibers with core/sheath or hollow structures [14, 18-20]. With these approaches the structure and morphology of the electrospun fibers can be carefully controlled.

In addition, the morphology and properties of the electrospun fibers are highly tunable by modifying any number of fabrication parameters, including the concentration of polymer solution, the voltage between the nozzle and collector, humidity in the chamber, temperature, and solvents [12, 21]. The choice of solvent is also critical as to whether fibers are capable of forming and can also influence fiber porosity. To allow for sufficient solvent evaporation to occur in the time between the capillary tip and the collector, a volatile solvent must be used. Phase separation may also occur during the fiber jet trajectory through the atmosphere toward the collector before the solid polymer fibers are deposited. This process is greatly influenced by the volatility of the solvent.

The traditional electrospinning technique requires starch fibers to dehydrate in the short traveling time between the nozzle and collector. This is particularly difficult for starches such as pure Tapioca starch fibers since they can become quite swollen and be difficult to dehydrate. Thus, an innovative method capable of fabricating electrospun tapioca starch is required. The research described here examines the fabrication of highly pure Tapioca starch fibers, using a modified electrospinning setup with the addition of an ethanol collector bath cooled at -20°C in order to increase the dehydration speed of the swollen electrospun tapioca fibers. The processing parameters include such intrinsic properties of the polymer solution as concentration and viscosity and operation conditions such as the strength of the applied electric field, the distance between the nozzle and collector, and the flow rate. The prepared NTS fiber properties such as size, structure, morphology, water swelling ratio and disintegration properties [22-23] were then investigated.

2. MATERIALS AND METHODS

2.1 Preparation of Natural Tapioca Starch Solutions

NTS was purchased from E.T.C. International Trading Co., Ltd. (Thailand) and deionized water was supplied by Electroceramics Research, Physics and Material Science, Chiang Mai University, Thailand. They were mixed in concentrations of NTS of 3, 3.5, 4, 4.5 and 5 wt% and the mixtures were then stirred for 20 min at 75°C in order to fully dissolve the starch. After that, the prepared solutions were cooled to room temperature to be ready to be electrospun.

2.2 Electrospinning of Tapioca Starch Solution

Electrospinning is a process adapted from electrospraying where droplets of solid polymer are formed instead of fibers. In electrospinning, a number of processing parameters are, carefully controlled in order to generate the polymer fibers with the desired formation and structure as opposed

to just droplets. Three important parameters; the applied voltage, polymer flow rate and capillary-collector distance, are normally optimized. In this work, to form the required NTS fiber structure, these three parameters were first varied and then kept at optimum values of 20 kV for the applied voltage, 10 ml/h for the polymer flow rate, 0.9 mm diameter of the tip and 15 cm for the capillary-collector distance.

Figure 1 shows the experimental setup for the modified electrospinning technique. The ethanol bath at -20°C (Ethanol of 99.9% purity from Merck), was added to a typical syringe pump electrospinning system in order to enhance the rate of dehydration of the electrospun tapioca starch fibers. A metal grid was used as a target immersed within the ethanol bath. Tapioca starch pastes of various concentrations were forced through the needle using a syringe pump and then were electrospun directly to the metal target in the -20°C cooled ethanol bath. After that, water and ethanol stored within the electrospun tapioca starch fibers were removed using a vacuum pump.

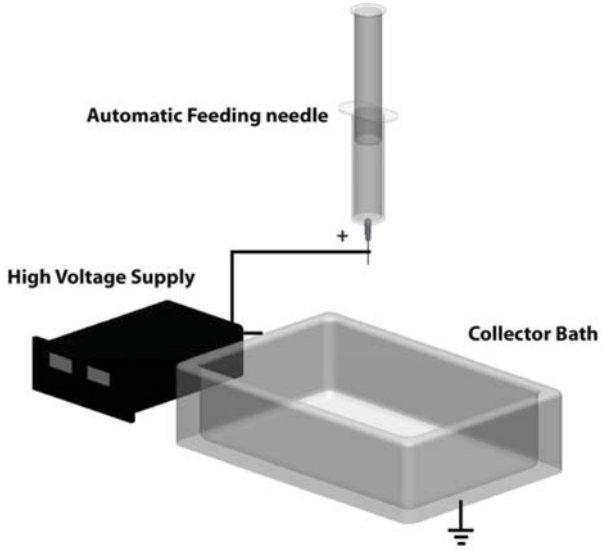

Figure 1. The modified electrospinning setup with -20°C ethanol bath.

2.3 Structure Characterization

FT-IR analysis was used to qualitatively characterize the functional groups of the tapioca starch powder and the electrospun fibers. The FTIR spectra were collected at a resolution of 2 cm^{-1} on a Nicolet 6700 FT-IR, from Thermo Electron Scientific Instrument,LLC (USA). The X-ray diffraction (XRD) patterns of the tapioca starch powder and fibers were investigated using an X-ray diffractometer (X' Pert Pro MTD, PANalytical) with Nickel-filtered Cu Kα radiation at 40 kV and 50 mA in the 2θ range of 5°- 60°.

2.4 Morphology Observations

The morphology of the tapioca starch fibers was examined using a scanning electron microscope (SEM; SNE-3000M, Nanoeye) to determine the pore and diameter characteristics. The samples were arranged on a metal stub using carbon adhesive tape and coated with gold under vacuum before observation.

2.5 Water Swelling Ratio

NTS fibers were left in a hot air oven; redLINE (BINDER, Germany) at 30±0.5°C for 2 days. The water swelling ratio (WSR)

of the electrospun tapioca starch fibers was calculated using the following equation:

$$WSR = \frac{W_1 - W_0}{W_0} \times 100\%$$

where W_0 is the weight of the tapioca starch fiber which was dried at 60°C until a constant weight was achieved and W_1 is the weight of the fully swollen fiber after being centrifuged at 4000 rev/min for 10 min. All the experiments were performed in triplicate [24- 26].

2.6 Disintegration Properties

In this test, the electrospun NTS fibers at 4.5 wt% of NTS solution were compared with NTS powders. NTS fibers of 4.5 wt% were was used as a disintegrating excipient in tablet form with concentrations of 1, 2.5, 5, 7.5 and 10 wt% in dibasic calcium phosphate dihydrate, compared with the same amount of tapioca starch, and the effects of both excipients on disintegration were studied. A direct compression dibasic calcium phosphate dihydrate (Sudeep Pharma Ltd., India) was tumble-mixed for 5 minutes in a plastic bag with the starch. Subsequently the homogeneous powder was thoroughly combined with magnesium stearate as lubricant, in the amount of 0.5 percent by weight, for one minute. The mixed powder was then compressed on a single stroke tablet-making machine (Hanseaten Exacta E1, Germany) using a compression force of 1800 kg. The tablets so obtained have a round shape and a flat surface, with a diameter of 10 mm, and a weight of 500 mg per tablet. The tablets were checked for hardness by hardness tester (Erweka, TBA-100, Germany). The tablet is placed between two jaws that crush the tablet. The machine measures the force applied to the tablet and detects when it fractures. And disintegration time was measured by disintegration apparatus (Pharmatest, PTZ-AUTO, Germany) in distilled water at 37°C, following USP 32/ NF 27.

3. RESULT AND DISCUSSION

3.1 Structure and Morphology Characterization

3.1.1 FT-IR analysis

Figure 2 shows the FT-IR spectra of the native tapioca starch powders and electrospun tapioca starch fibers. It can be seen that the FTIR spectra of the native tapioca starch powders have three main peaks with maximum absorbance at 1149 cm^{-1}, 1077 cm^{-1} and 995 cm^{-1}. The bands at 1149 $cm^{-1}$and 1077 cm^{-1} are associated with the ordered structures of starch, whereas, the band at 995 cm^{-1} is indicative of amorphous structured starch [27]. Other characteristic bands at 1210 cm^{-1} and 1720 cm^{-1} can be attributed to the bending and stretching vibration of the C-O bond while the broad 3423 cm^{-1} band corresponds to the stretching vibration of the O-H bond [28].

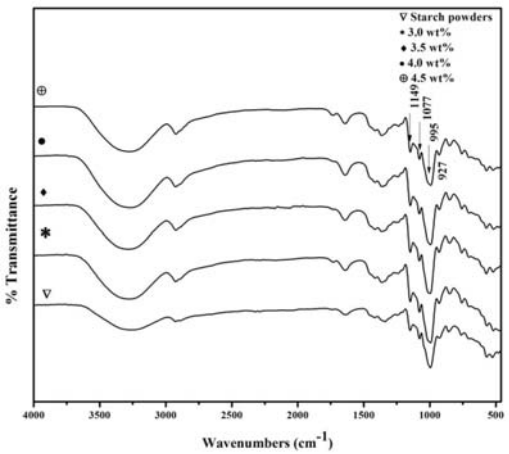

Figure 2. The FT-IR spectra of NTS powders and NTS fibers.

It can be seen that the intensity of the 995 cm^{-1} band of the electrospun NTS fibers increased between the NTS fibers with concentrations of 3.0 wt% and 3.5 wt%. These results suggest that the ordered structure of the native starch was disrupted which may occur during the preparation of the tapioca starch solution at 75°C to dissolve the starch in deionized water. The heat required during this process may disrupt the structure of the starch, resulting in a more amorphous structure of the electrospun fibers. For the NTS fibers prepared by NTS solution concentrations up to 4.0 wt% and 4.5 wt%, the 995 cm^{-1} band were decreasing. This is indicative of the increase in crystallinity of the fibers containing higher concentrations of tapioca starch due to the retrogradation of starch [27].

It is also interesting to note that the native starch has a prominent band at 927 cm^{-1}. This is a water sensitive band characteristic of hydrophilicity in starches [29]. Considering the FT-IR spectra of all electrospun fibers, the intensity of this band slightly increased compared to that of native tapioca starch powder, suggesting an increase in hydrophilicity. This may be related to the enhancement of the amorphous nature in the electrospun starch samples with a concomitant decrease in their ordered structure [24].

3.1.2 X-ray diffraction studies

The X-ray diffraction patterns of the NTS powder and electrospun NTS fibers are shown in Figure3. From the XRD patterns of the NTS powders there are diffraction peaks at 2θ of 15.2, 17.2, 19.9, 23.3 and 26.5 degrees, which are characteristic of an A-type starch [30]. All of the XRD patterns of the NTS fibers illustrate an amorphous type pattern showing a very broad pattern. For the electrospun fibers with 4.5 wt% of NTS concentration there is a noticeable diffraction peak at around 2θ = 13°. This may be attributed to increase in crystallinity of this 4.5wt% electrospun fiber. This result agrees well with FT-IR spectra as an increase in the crytallinity of the electrospun NTS was observed in these high concentration samples.

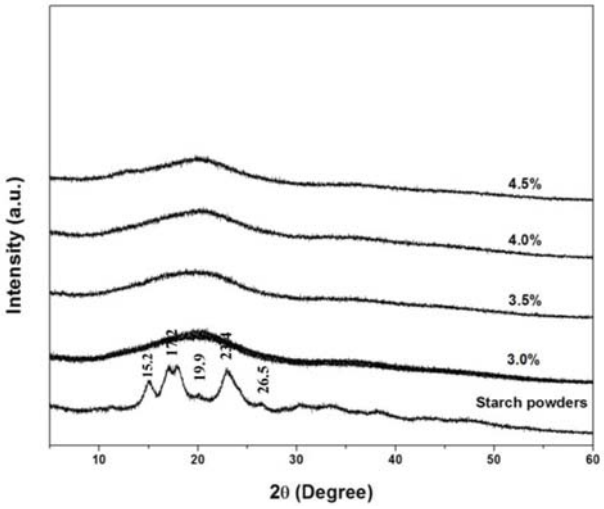

Figure 3. XRD patterns of NTS powder and the electrospun NTS fibers with starch concentrations of 3.0 wt%, 3.5 wt%, 4.0 wt%, and 4.5 wt%.

3.1.3 Morphology observations

The morphology of the NTS fibers was observed using a Scanning Electron Microscope and is shown in Figure 4. The electrospun NTS fibers have diameters of 1.3-14.5 μm. All formed well defined mats except for that of the 3 wt% sample, which showed a large connected area. This may be due to the incomplete dehydration process of the 3 wt% electrospun fibers where the remaining water may later dissolve some fibers resulting in a large connected area. It can be also noticed that the increase in NTS concentration gave rise to smoothness in the electrospun fibers with an optimum value of 4.5 wt%. The 5 wt% solution caused the block up of the spinneret tip as a result of its high viscosity.

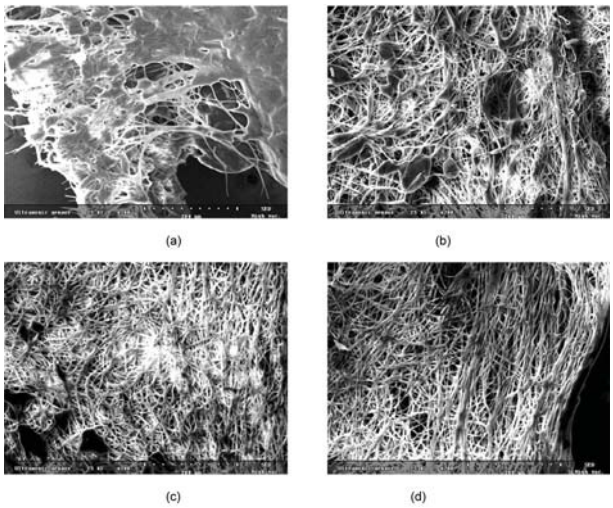

Figure 4. The morphology of the electrospun NTS fibers with starch concentrations of (a) 3 wt%, (b) 3.5 wt%, (c) 4 wt% and (d) 4.5 wt%.

3.2 Water Swelling Ratio

The tablet disintegration process is the beginning of the drug release process. If the tablet has rapid disintegration time this results in fast release. Swelling is the main mechanisms of the disintegration process. Normally, swelling agents absorb amounts of water and generate driving forces to disintegrate the tablet into small pieces before the dissolution process [31]. For drug-release application purposes, the water swelling ratios (WSR) of each of the electrospun NTS fiber mats were measured. Figure 5 shows the relationship between the WSR of the electrospun NTS fibers and their concentrations. It can be clearly seen that the WSR of the NTS fibers increased as the concentration of the NTS solution increased. Considering the morphology of the NTS fibers (Figure 4), the increase in NTS concentration not only affected the smoothness of the fibers but also increased the surface area of the fiber mats, leading to an increase in their WSR. This result is consistent with the FT-IR result as an increase in hydrophilicity of the electrospun NTS fibers was also observed with increasing starch concentration.

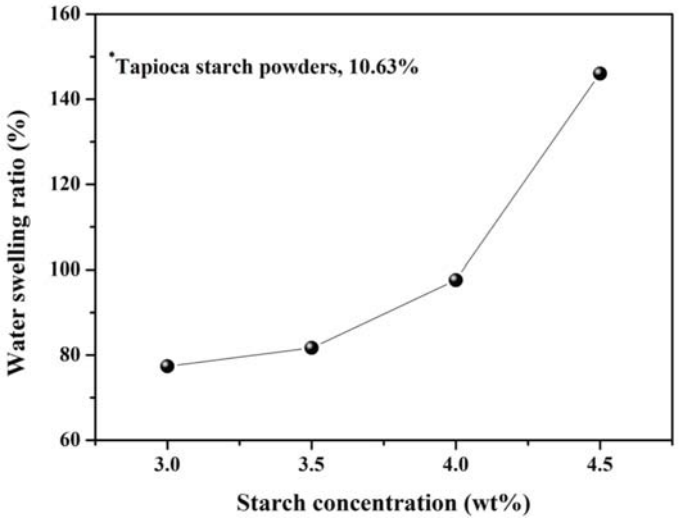

Figure 5. The relationship between the starch concentration and water swelling ratio.

3.3 Disintegrating Properties

The average disintegration times of tablets which contain 4.5 wt% NTS fiber (table 1) in percentages of 1, 2.5 and 5 wt% were 284, 241 and 223 seconds respectively. In comparison with NTS powder of the same amount, it was found that the disintegration times of tablets using NTS powder as disintegrate were more than 10 minutes longer than that of NTS fiber. For higher content, i.e. 7.5 and 10 wt%, the NTS powder showed lower values of 55 and 80 seconds disintegration time, while NTS fiber took 234 and 462 seconds. With higher content of NTS fiber, it was possible to prevent water uptake by the tablet surface thus also delaying disintegration because of its high swelling property, leading to blocking the water. From the results obtained, it can be concluded that NTS fiber can be used in much smaller amounts than NTS powder to promote tablet disintegration. This research controls the hardness in the range of 5-7 kgf for comparable disintegration times of NTS powders and NTS fibers. When 2.5 or 5.0 wt% each of NTS fiber and NTS powder were used in combination in tablet, it was evident that there were synergistic effects leading to a shorter tablet disintegration time, i.e. 95 and 84 seconds, compared with using a single component with the same amounts. To find other possible applications in pharmaceutical formulations of this new NTS fiber, further studies will be conducted.

Table 1. The disintegration times of tablets which contain NTS fibers and NTS powder.

	Disintegrations times (sec.)										
		NTS fibers (wt%)					NTS powders (wt%)				
No.	Emcompress	1	2.5	5	7.5	10	1	2.5	5	7.5	10
1	> 900	276	251	217	213	490	> 900	> 900	> 900	67	80
2	> 900	248	251	243	229	400	> 900	> 900	> 900	55	69
3	> 900	274	241	202	232	508	> 900	> 900	> 900	46	111
4	> 900	258	267	260	228	486	> 900	> 900	> 900	39	90
5	> 900	330	225	204	253	539	> 900	> 900	527	63	76
6	> 900	318	213	215	249	354	> 900	> 900	698	59	51
x	-	284.0	241.3	223.5	234.0	462.8	-	-	-	54.8	79.5
SD	-	32.9	19.6	23.1	14.8	70.6	-	-	-	10.6	20.2

4. CONCLUSION

An electrospinning technique with the addition of a cooled collecting bath of ethanol at -20°C was employed successfully for the fabrication of highly pure electrospun NTS fibers. Starch concentration of 4.5 wt% in deionized water gave rise to electrospun fiber mats with a smooth and homogeneous fiber surface. The largest surface area was also obtained for the 4.5 wt% sample which resulted in the highest value of the water swelling ratio. The structural studies in both FT-IR and XRD revealed an increase in the amorphous nature of all electrospun NTS fibers compared to that of NTS powder. This electrospun high purity NTS fiber mat may be of particular interest in drug-release applications. The use of NTS fiber and NTS powder in combination with a lower amount as disintegrant for each tablet, rendered good disintegrating times of about one and a half minutes. NTS fiber itself, however, cannot be compared with a superdisintegrant. To ensure the safe use of this product, further experiment in biocompatibility should be conducted.

ACKNOWLEDGEMENTS

The authors would like to express their sincere gratitude to the Thailand Research Fund (TRF), the Royal Golden Jubilee Ph.D. Program, Office of the Higher Education Commission (OHEC) and the Graduate School and Faculty of Science, Chiang Mai University, Thailand for their financial support. We also wish to thank the National Research University Project under Thailand's Office of the Higher Education Commission for financial support. The authors would to thank Dr. Denis Russell Sweatman for checking the manuscript.

REFERENCES

[1] Elvira C., Mano J.F., Roman J.S. and Reis R.L., Starch-based biodegradable hydrogels with potential biomedical applications as drug delivery systems, *Biomaterials*, 2002; **23**: 1955-1966.

[2] Ahmed J.M. AK. and Ali H.R. AD., Preparation and using of acrylamide grafted starch as polymer drug carrier, *Carbohyd. Polym*., 2010; **79**: 769-774.

[3] Biswas N., Dey S. and Agarwal A., Study of mucoadhessive microspheres of metoprolol tartarate based on crosslinked tapioca starch as new carrier for drug delivery, *Int. J. Contemp. Res. Rev*., 2010; **1**: 1-9.

[4] Jeroen J.G.S., Hubertus T., Dick W. and Johannes F.G.V., Short-range structure in (partially) crystalline potato starch determined with attenuated total reflectance Fourier-transform IR spectroscopy, *Carbohyd. Res*., 1995; **279**: 201-214.

[5] Lidia E., Ann-Charlotte E. and Marie W., Changes in starch structure during manufacturing of starch microspheres for use in parenteral drug formulations: Effects of temperature treatment, *Carbohyd. Polym*., 2009; **75**: 157-165.

[6] Marta C., Carmen F. and Jimenez-Castelled R.M., Graft tapioca starch copolymers as novel excipients for controlled-release matrix tablets, *Carbohyd. Polym*., 2010; **80**: 71-77.

[7] Ferrero C. and Jimenez-Castellanos M.R., The influence of carbohydrate nature and drying methods on the compaction properties and pore structure of new methyl methacrylate copolymer, *Int. J. Pharmaceut*., 2002; **248**: 157-171.

[8] Casas M., Strusi O.L., Jimenez-Castellanos M.R. and Colombo P., Tapioca starch graft copolymer and Dome Matrix modules assembling technology, Part I. Effect of module shape on drug release, *Eur. J. Pharmaceut. Biopharmaceut*., 2010; **75**: 42-47.

[9] Agarwal S., Wendorff J.H. and Greiner A., Use of electrospinning technique for biomedical applications, *Polymer*, 2008; **49**: 5603-5621.

[10] Chen J.W., Tseng K.F., Delimartin S., Lee C.K. and Ho M.H., Preparation of biocompatible membranes by electrospinning, *Desalination*, 2008; **233**: 45-54.

[11] Lee K.Y., Jeong L., Kang Y.O., Lee S.J. and Park W.H., Electrospinning of polysaccharides for regenerative medicine, *Adv. Drug Delivery Rev*., 2009; **61**: 1020-1032.

[12] Lu C., Chen P., Li J. and Zhang Y., Computer simulation of electrospinning, Part I. Effect of solvent in electrospinning, *Polymer*, 2006; **47**: 915-921.

[13] Changsarn S., Mendez J.D., Weder C., Srikhirin T. and Supaphol P., Electrospinning of light-emitting fibers from a tertiary blend solution of an inert polymer and two conjugated polymers, *Chiang Mai J. Sci*., 2011; **38**: 193-302.

[14] Li D. and Xia Y., Electrospinning of nanofibers: Reinventing the wheel?, *Adv. Mater*., 2004: 1151-1169.

[15] Kim J.S. and Reneker D.H., Polybenzimidazole nanofiber produced by electrospinning, *Polym. Eng. Sci*., 1999; **39**: 849-854.

[16] Reneker D.H., Kataphinan W., Theron A., Zussman E. and Yarin A.L., Nanofiber garlands of polycarpolactone by electrospinning, *Polymer*, 2002; **43**: 6785-6794.

[17] Fang D., Hsiao B.S. and Chu B., Multiple-jet electrospinning of nonwoven nanofiber, *Polym. Prepr*. 2003; **44**: 59-66.

[18] Gupta P. and Wilkes G.L., Some investigations on the fiber formation by utilizing a side-by-side bicomponent electrospinning approach, *Polymer*, 2003; **44**: 6353-6359.

[19] Sun Z., Zussman E., Yarin A.L., Wendroff J.H. and Grener A., Compound core-shell polymer nanofibers by co-electrospinning, *Adv. Mater*., 2003; **15**: 1929-1932.

[20] Larsen G., Spretz R. and Velarde-Ortz R., Use of coaxial gas jackets to stabilize taylor cones of volatile solutions and to induce particle-to-fiber transitions, *Adv. Mater*., 2004; **16**: 166-169.

[21] Thompson C.J., Chase G.G., Yarin A.L. and Reneker D.H., Effects of parameters on nanofiber diameter determined from electrospinning model, *Polymer*, 2007; **48**: 6913-6922.

[22] Medina M.L.R. and Kumar V., Evaluation of cellulose II poeders as a potential multifunctional excipient in tablet formulations, *Int. J. Phamaceut*., 2006; **322**: 31-35.

[23] Yamamoto Y., Fujii M., Watanabe K., Tsukamoto M., Shibata Y., Kondoh M. and Watanabe Y., Effect of powder characteristics on oral tablets disintegration, *Int. J. Phamaceut*., 2009; **365**: 116-120.

[24] Sevenou O., Hill S.E., Farhat I.A. and Mitchell J.R., Organization of the external region of the starch granules as determined by infrared spectroscopy, *Int. J. Biol. Macromol*., 2002; **31**: 79-85.

[25] Al-Karawi A.J.M. and Ali H.R. A.D., Preparation and using of acrylamide grafted starch as polymer drug carrier, *Carbohyd. Polym.*, 2010; **79**: 769-774.

[26] Wang Q., Zhang N., Hu X., Yang J. and Du Y., Chitosan/starch blend fibers and their properties for drug controlled release, *Carbohyd. Polym*., 2010; **82**: 842-847.

[27] Dupuy N., Wojciechowski C., Ta C.D., Huvenne J.P. and Legrand P., Midinfrared spectroscopy and chemometrics in corn starch classification, *J. Mol. Struct*., 1997; **410-411**: 551-554.

[28] Wang Q., Hu X., Du Y. and Kennedy J.F., Alginate/starch blend fibers and their properties for drug controlled release, *Carbohyd. Polym*., 2010; **82**: 842-847.

[29] Alexander R.J., Maltodextrins: Production properties and applications; in Scenck F.W., Hebeda R.A., eds., *Starch Hydrolysis Products, Worldwide Technology Production and Applications*, 1992; 233-276.

[30] Bos C.E., Native starch in tablet formulations: Properties on compaction, *Pharm. Weekly Sci*., 1987; **9**: 274-282.

[31] Omidian H. and Park K., Swelling agents and devices in oral drug delivery, *J. Drug Deliv. Sci.Technol*., 2008; **18**: 83-93.

Available online at www.sciencedirect.com

ScienceDirect

Ceramics International 40 (2014) 4251–4256

CERAMICS INTERNATIONAL

www.elsevier.com/locate/ceramint

Structural and electrical properties of BZT-added BNLT ceramics

P. Kantha[a], N. Pisitpipathsin[b], K. Pengpat[b], S. Eitssayeam[b], S. Pojprapai[a,*]

[a]School of Ceramic Engineering, Institute of Engineering, Suranaree University of Technology, Nakhon Ratchasima 30000, Thailand
[b]Department of Physics and Materials Science, Faculty of Science, Chiang Mai University, Chiang Mai 50200, Thailand

Received 7 August 2013; accepted 21 August 2013
Available online 29 August 2013

Abstract

Lead free piezoelectric ceramics $(1-x)$BNLT$-x$BZT with $x=0.00$, 0.06, 0.09 and 0.12 were prepared using a two-step mixed oxide method. Dielectric, ferroelectric and piezoelectric properties of the ceramics were improved by the addition of the BZT. XRD results show tetragonal symmetry structure of the BNLT–BZT ceramics. It was found that the tetragonality increases with increasing BZT content. The optimum composition is $x=0.09$, where the maximum values of the piezoelectric constant d_{33} ($\sim$126 pC/N) and dielectric constant ($\sim$2400) were obtained at room temperature. This BNLT–BZT system can be a promising candidate for lead-free piezoelectric ceramics.

Keywords: C. Dielectric properties; C. Piezoelectric properties; D. Perovskites; D. $BaTiO_3$ and titanates

1. Introduction

Lead-based piezoelectric materials are a source of pollution in electronic industrial applications and mostly come from the production of $Pb(Zr,Ti)O_3$ (PZT), $PbTiO_3$ (PT) and $Pb(Mg_{1/3}Nb_{2/3})O_3$ (PMN) compounds. Many researchers have focused on finding alternative piezoelectric materials containing no lead [1–6]. Bismuth sodium titanate (BNT: $(Bi_{0.5}Na_{0.5})TiO_3$) based materials have been of particular interest in the field of piezoelectric materials and devices for the past few decades [7–9]. BNT crystals have a perovskite structure with rhombohedral symmetry at room temperature and two phase transitions at T_2 ($\sim$220 °C) and T_m ($\sim$320 °C) where ferroelectric (FE) rhombohedral changes to antiferroelectric (AF) tetragonal, and AF tetragonal changes to paraelectric (PA) cubic, respectively. However, the drawback of BNT ceramics is the difficulty in poling due to high conductivity. This may be attributed to mobile ions (Na^+, Bi^{3+}) which diffuse easily in the material when an electric field is applied during the poling process, especially at elevated temperatures. Consequently, the dipole moments cannot be completely aligned along the direction of the applied electric field. This results in less the polarization of the material and poor piezoelectric and ferroelectric properties. This problem can be solved by doping A-site and B-site cations in BNT crystals. Recently, many works showed the improvement of piezoelectric and ferroelectric properties due to the effect of dopants in BNT-based materials such as BNLT [10], BNT–BT [11–13], BNT–BZT [14,15], BNT–KN [1,16] and BNT–BT–KNN [17]. In addition to BNT-based ceramics, barium zirconium titanate ($BaZr_xTi_{1-x}O_3$: BZT) solid solution has been investigated to develop high-quality lead-free ceramics because of its high dielectric constant and low loss [18]. The substitution of Zr^{4+} ions by the Ti^{4+} ions in $BaTiO_3$ significantly improves the overall electrical properties of the material due to its better chemical stability [19]. It is known that the ferroelectric phase transition temperature of BZT changes with Zr^{4+} content. If x content is more than 10 mol%, BZT ceramics exhibit relaxor behavior [20] while the x content is less than 10 mol%, the BZT ceramics exhibit normal ferroelectric behavior [21]. Recently, Yu et al. reported that $Ba(Zr_{0.05}Ti_{0.95})O_3$ exhibited relatively high piezoelectric and ferroelectric properties (e.g. 236 pC/N) compared to other lead-free ferroelectric materials [22]. In this present work, we aim to study the ferroelectric, piezoelectric and dielectric properties of $(1-x)$BNLT$-x$BZT with $x=0.00$, 0.06, 0.09 and 0.12. To improve the electrical properties of BNLT–BZT ceramics, the ceramics were prepared by using

*Corresponding author. Tel.: +66 44 224542.
E-mail address: soodkhet@sut.ac.th (S. Pojprapai).

0272-8842/$ - see front matter © 2013 Elsevier Ltd and Techna Group S.r.l. All rights reserved.
http://dx.doi.org/10.1016/j.ceramint.2013.08.089

the two-step mixed oxide method. The comparison between electrical properties of BNLT–BZT and that of BNT–BZT obtained from previous works was reported.

2. Experimental

The starting chemicals for producing the $(1-x)(Bi_{0.4871}Na_{0.4871}La_{0.0172}TiO_3$: BNLT$)-x(BaZr_{0.05}Ti_{0.95}O_3$: BZT) ceramics, where $x=0.0$, 0.06, 0.09 and 0.12, were high purity ($>99.0\%$) powders of bismuth oxide: Bi_2O_3 (Fluka), sodium carbonate: Na_2CO_3 (Riedel-de Haën), lanthanum oxide: La_2O_3 (Fluka), titanium dioxide: TiO_2 (Riedel-de Haën), barium carbonate: $BaCO_3$ (Fluka) and zirconium dioxide: ZrO_2 (Riedel-de Haën). BNLT and BZT powders were prepared separately by calcination at 900 °C and 1250 °C for 2 h, respectively and they were then mixed corresponding to the above formula using the ball-milling method for 24 h with ethanol as a milling media. The dried powders were then sieved to prepare pellets of 10 mm in diameter, which were subsequently sintered between 1075 °C and 1500 °C in an electric furnace and air atmosphere under controlled heating and cooling rates of 5 °C /min for 4 h. Phase identification and microstructure of the resulting ceramics were performed by using an X-ray diffractometer (XRD: Philip X'pert) with Cu K_α radiation and scanning electron microscope (SEM, JEOL JSM5910LV). The mean linear intercept method was used to determine the grain size of each sintered sample. Two circular surfaces of the sintered ceramics were polished and coated with silver paste as electrodes. The room temperature dielectric constant (ε_r) and dielectric loss ($\tan\delta$) of the ceramics were measured at 1–100 kHz using an LCZ meter (HP4276A). After the samples were poled for 15 min at 3.0 and 4.0 kV/mm, the piezoelectric charge constant (d_{33}) was measured by using a piezoelectric-d_{33}-meter (APC product inc. S5865). A Sawyer-Tower circuit was used to measure the hysteresis loop of the ceramic samples at room temperature under an electric field of 7 kV/mm.

3. Results and discussion

The phase formation study of $(1-x)$BNLT$-x$BZT ceramics where $x=0.00$–0.12 was carried out by XRD (see Fig. 1). It is found that each XRD pattern exhibited a pure perovskite phase and no second phases. All diffraction peaks were matched with the perovskite $Bi_{0.4871}Na_{0.4871}La_{0.0172}TiO_3$ phase with rhombohedral structure similar to that of the pure BNLT ceramics found in our previous works [2,3,5] Slight shift in d-spacing and splitting of the peak was observed around 46.5°. This implies that there was a change in the lattice parameters and c/a ratio of these ceramics. The lattice parameters were then calculated by using JADE software (version 6.5). Lattice constants (Å) as a function of BZT content are shown in Fig. 2. From the results, it implies that the fraction of the BZT content affects the crystal structure, tetragonality (c/a ratio) of the BNLT–BZT ceramics (e.g. tetragonality increases with increasing BZT content). This phenomenon can be caused by the substitution of Ba^{2+}, and Zr^{4+} into BNLT crystals. The ionic radii of Bi^{3+}, La^{3+} and Na^{+} in the 12 fold coordination

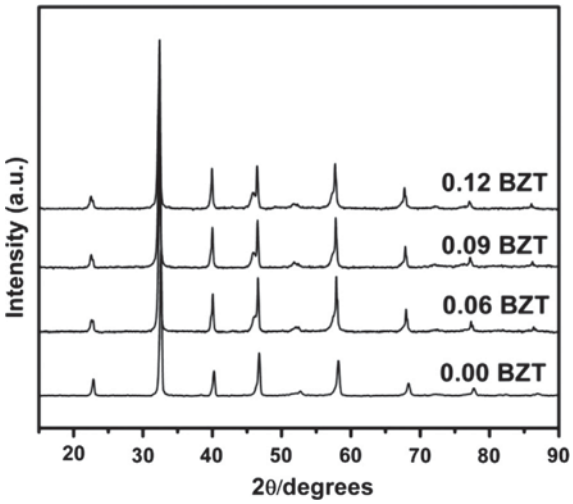

Fig. 1. X-ray diffraction pattern of $(1-x)$BNLT$-x$BZT ceramics where $x=0.0$–0.12.

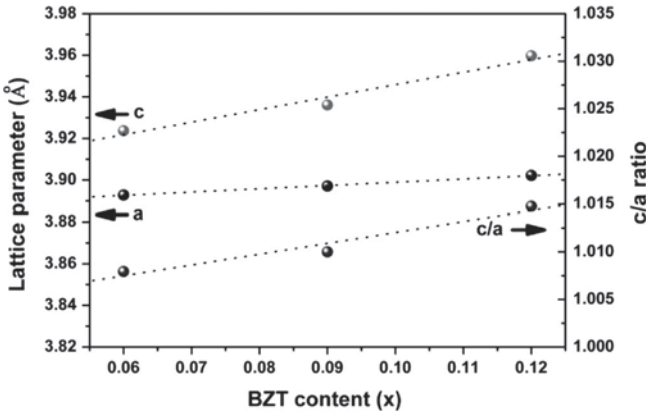

Fig. 2. Lattice parameters and c/a ratio of $(1-x)$BNLT$-x$BZT ceramics where $x=0.0$–0.12.

site and Ti^{4+} in the 6 coordination site for $Bi_{0.4871}Na_{0.4871}$-$La_{0.0172}TiO_3$ perovskite structure were 1.400 Å, 1.360 Å, 1.390 Å and 0.605 Å, respectively. The larger ionic radius Ba^{2+} (1.610 Å) for the 12 fold coordination site and Zr^{4+} (0.720 Å) for the 6 coordination site enter the $Bi_{0.4871}Na_{0.4871}$-$La_{0.0172}TiO_3$ perovskite structure and substitute for the Bi^{3+}, La^{3+}, Na^{+} and Ti^{4+} ions, having smaller ionic radii, resulting in the elongation of the crystal structure. Therefore, it can imply that the substitution of Ba^{2+} into the Bi^{3+}, La^{3+}, Na^{+} sites and Zr^{4+} into the Ti^{4+} site lead to deformation in lattice parameters and increasing tetragonality. The rhombohedral structure of BNLT ceramics changed continuously into a tetragonal one when the BZT content increased [23].

Fig. 3 shows the as-sintered surface of the $(1-x)$BNLT$-x$BZT ceramics. The microstructure results agree well with the XRD results, as no impurities were observed in the sintered pellets, which exhibited dense microstructures without abnormal grains. Round grains were observed in the pure BNLT ($x=0.0$) and rectangular grains were found in the BNLT–BZT samples. These results indicate that the addition of BZT content has an effect on the morphology of the

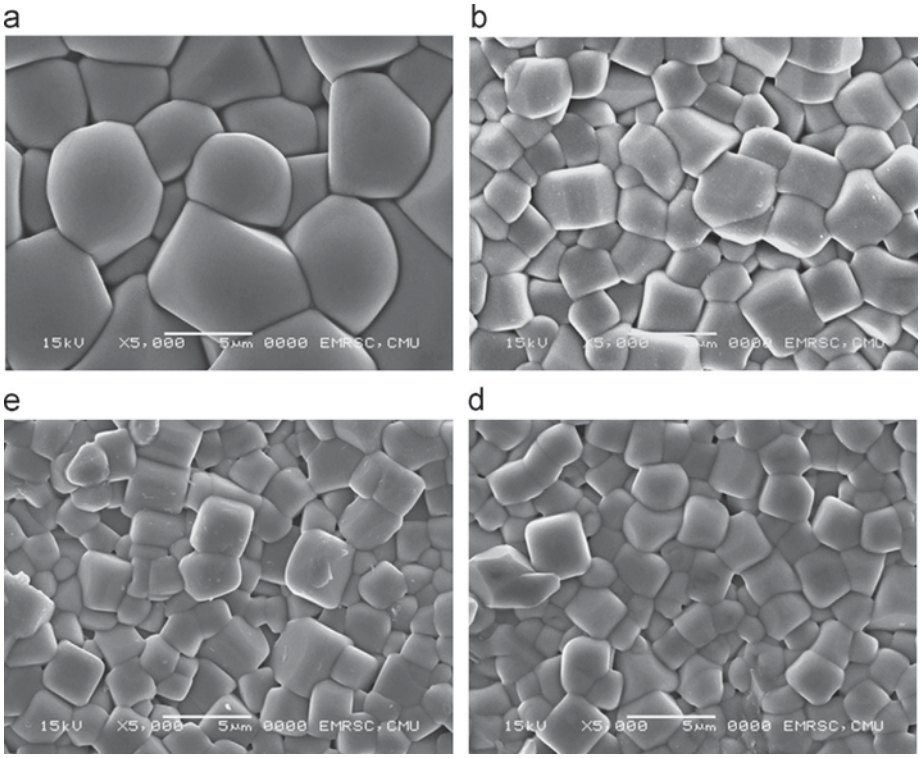

Fig. 3. SEM micrograph of $(1-x)$BNLT$-x$BZT ceramics where (a) $x=0.0$ (BNLT), (b) $x=0.06$, (c) $x=0.09$ and (d) $x=0.12$.

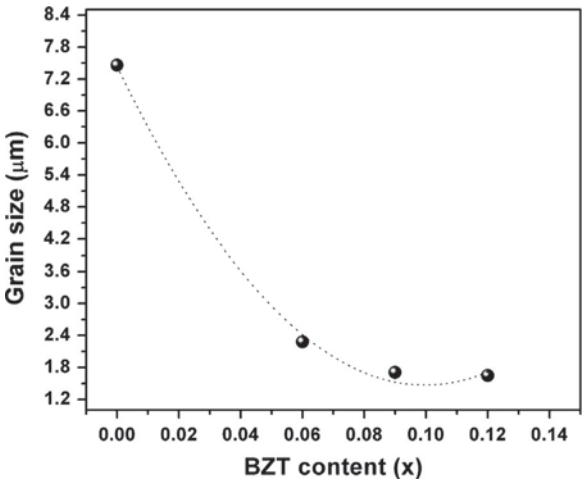

Fig. 4. The relationship between grain size and BZT content of the $(1-x)$ BNLT$-x$BZT ceramics.

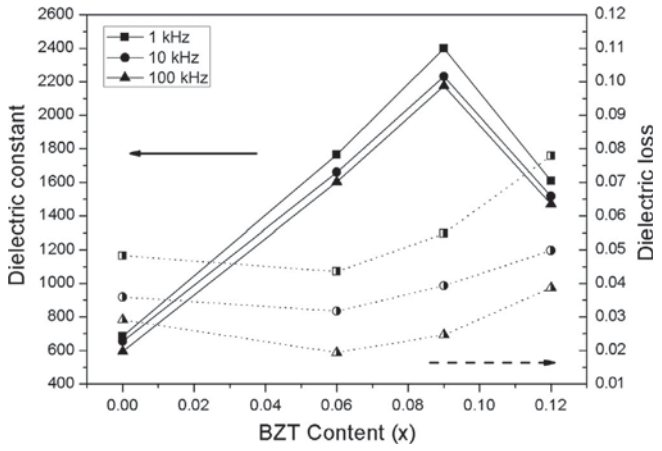

Fig. 5. The dielectric constant and dielectric loss at room temperature as a function of BZT content in $(1-x)$BNLT$-x$BZT system.

microstructure. From microstructural analysis, it was revealed that BZT addition causes a notable decrease in grain size as shown in Fig. 4. The average values of grain sizes, measured by the linear intercept method, decreased from $\sim$7.4 μm for pure BNLT to $\sim$1.5 μm for the $x=0.12$ sample. This is consistent with our previous work [24,25] where the substitution of larger A-site cations Ba^{2+} into the Bi^{3+} site, which possessed a smaller ionic radius, contributed to the inhibition of grain growth.

The dielectric constant (ε_r) of the $(1-x)$BNLT$-x$BZT samples with various frequencies at room temperature is shown in Fig. 5. It can be seen that the BZT addition enhances the dielectric constant of BNLT ceramics. The dielectric constant at 1 kHz was approximately 685 for pure BNLT ($x=0.0$) and increase up to $\sim$2400 at $x=0.09$, then decrease with further BZT addition. These results were partly attributed to ion substitution. In A site, when BZT is added into BNLT, the Ba^{2+} ions replace Na^{+} and act as donor ions. Then, A-site vacancies are created. Chopra et al.[26] reported that if the vacancies were in the lattice, the transfer of atoms would be easier than that in a perfect lattice and the domain wall motion could be induced by a smaller electric field. Thus, the increasing dielectric constant of ceramics was also attributed

to the increment in the magnitude of dipole moment due to the creation of cation vacancies in BNLT–BZT ceramics. However, the decreasing of dielectric constant at $x=0.12$ may be due to the excess of Ba^{2+} ions which replace the La^{3+} and/or Bi^{3+} sites, leading to oxygen vacancies. It is known that oxygen vacancies are the main cause of domain wall clamping which leads to the reduction of dielectric constant [27]. In the other hand, the substitution of Ti^{4+} site by Zr^{4+} ions improves the dielectric constant [14,22]. Low dielectric loss was observed for all samples. These properties may be useful for applications where low loss is particularly needed such as in capacitors and insulators.

The hysteresis loops of the BNLT–BZT ceramics, measured at room temperature using a Sawyer-Tower circuit, are illustrated in Fig. 6. The relevant remanent polarization (P_r) versus the BZT content was then plotted in Fig. 7. For the $x=0.00$ sample (pure BNLT), the hysteresis loop exhibits a typical ferroelectric P–E loop with high remanent polarization while slim hysteresis loops with small remanent polarization were observed for the BZT added samples ($x=0.06$). For $x \geq 0.06$, we observed double hysteresis loops. When BZT content increased, the hysteresis loop became an antiferroelectric-like shape. These results are closely similar to that of our previous study [3] as it was found that double P–E loops are observed in BNLT ceramics with added BT ≥ 6 mol%. This result implies that the anomalies in P–E loops resulted from the transition to an antiferroelectric phase at low temperature after adding BT and/or the electro-mechanical interaction between the polar and non-polar regions, which co-existed in the ceramics [28]. The addition of BZT causes a decrease in the remanent polarization. The same trend was also observed for the value of E_c as shown in Fig. 7. Good ferroelectric properties are generally shown in the sample with high value of the P_r and low value of the E_c. From Fig. 7, the BZT addition in BNLT ceramic with $x=0.06$ caused the reduction of E_c while high P_r was maintained. Therefore, it may be assumed that the 0.94BNLT–0.06BZT system has good ferroelectric properties with a high value of remanent polarization of 30.0 μC/cm^2 and a coercive electric field of 20.8 kV/cm. The low E_c of these samples indicates that the sample can be poled easily because the ferroelectric domains can be reoriented by the low applied field. In addition to P_r and E_c, the characteristics of ferroelectric properties can be qualified by the hysteresis loop squareness (R_{sq}). The R_{sq}

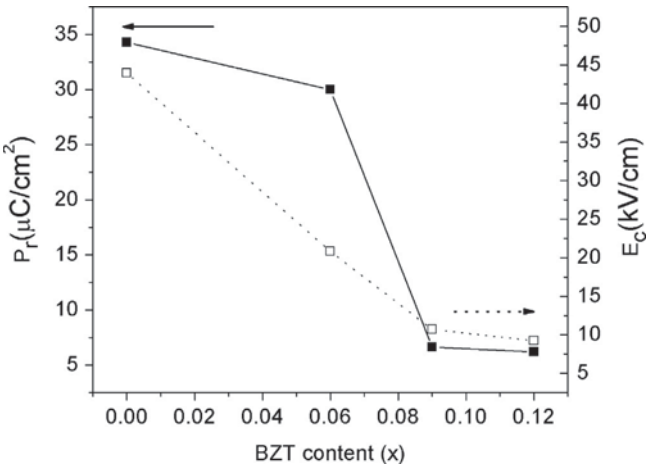

Fig. 7. Room-temperature remanent polarization (P_r) and coercive filed (E_c) as a function of BZT content (x).

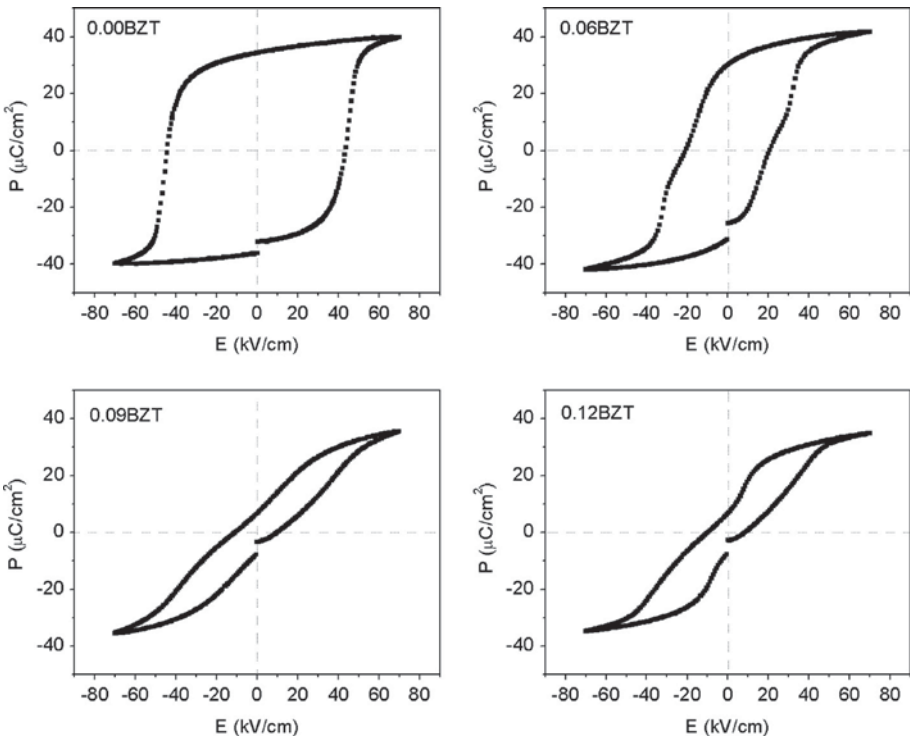

Fig. 6. Hysteresis loop of $(1-x)$BNLT$-x$BZT ceramics at room temperature.

coefficient can be calculate with the equation below [29].

$$R_{sq} = \left(\frac{P_r}{P_s}\right) + \left(\frac{P_{1.1Ec}}{P_r}\right) \quad (1)$$

where P_s is the saturated polarization obtained at some finite field strength below the dielectric breakdown. $P_{1.1Ec}$ is the polarization at the field equal to 1.1Ec. It is known that the ideal square loop, R_{sq} is equal to 2.00 [3]. As listed in Table 1, the loop squareness parameters R_{sq} values of ceramic samples were in the range from 0.26 to 1.55.

To study the piezoelectric property of the samples, the d_{33} piezoelectric coefficient was measured at room temperature using a d_{33}-meter. Two conditions of poling were used in the present work, the samples were poled at 3 kV/mm and 4 kV/mm at 50 °C for 15 min. The measured piezoelectric coefficient as a function of BZT content is shown in Fig. 8. It is seen that the electric field for poling has a strong effect for the d_{33} piezoelectric values, where the higher field gives rise to the higher d_{33} values. In addition, d_{33} values increase with increasing BZT content. For 3 kV/mm poling, the d_{33} value was increased from 71 pC/N for pure BNLT to 76 pC/N for the $x=0.09$ sample, followed by a reduction of d_{33} value to 73 pC/N for the $x=0.12$ sample. The reduction of the d_{33} value for higher BZT content may be due to the difficulty in poling as suggested above.

In case of poling at 4 kV/mm, the d_{33} and piezoelectric voltage coefficient (g_{33}) of the poled $(1-x)$BNLT$-x$BZT ceramics as a function of BZT content are tabulated in Table 1.

Table 1
The electrical properties of the $(1-x)$BNLT$-x$BZT samples.

Composition (X)	ε_r (at 1 kHz)	R_{sq}	d_{33}[a] (pC/N)	g_{33}[a] ($\times 10^{-3}$ Vm/N)
0.00	685	1.55	98	16.2
0.06	1762	0.83	98	6.28
0.09	2400	0.26	126	5.93
0.12	1600	0.29	118	8.33

[a]Poled at 4 kV/mm.

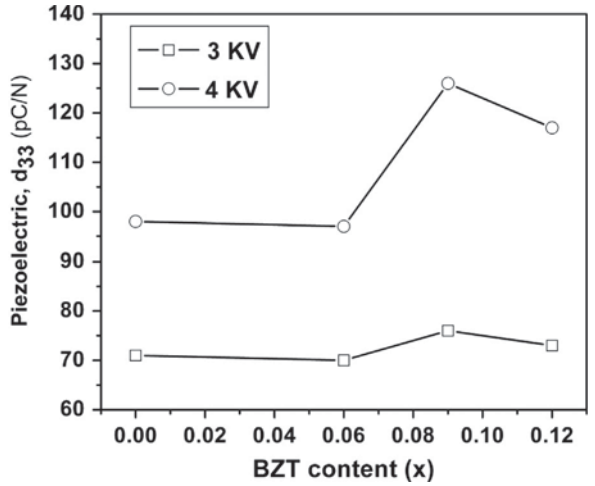

Fig. 8. Piezoelectric coefficient (d_{33}) at 3 and 4 kV of BNLT–BZT ceramics.

Table 2
The important dielectric and piezoelectric properties of the BNLT and 0.91BNLT–0.09BZT samples compared to that of previous works.

Samples	ε_r[a] (T_{room})	tan δ[a] (T_{room})	d_{33} (pC/N)
BNLT (this work)	685 (1 kHz)	0.05 (1 kHz)	98
0.91BNLT–0.09BZT (this work)	2400 (1 kHz)	0.05 (1 kHz)	126
BNLT [10]	550 (1 kHz)	0.04 (1 kHz)	91
0.94BNT–0.06BT [12]	950 (10 kHz)	0.01 (10 kHz)	125
0.91BNT–0.09BZT [14]	~880 (1 kHz)	0.03 (1 kHz)	147

[a]Frequency at 1 kHz.

The coefficient g_{33} was calculated via [30]:

$$g_{33} = \frac{d_{33}}{\varepsilon_0 \varepsilon_r} \quad (2)$$

where ε_0 is the permittivity of free space and ε_r is the relative permittivity. The ε_r was measured at room temperature and shown in Table 1. The significant effect of the d_{33} piezoelectric coefficient was found. The highest piezoelectric constants d_{33} were 126 pC/N and 118 pC/N for 0.91BNLT–0.09BZT and 0.88BNLT–0.12BZT samples, respectively (poled at 4 kV/mm) as compared with that of pure BNLT sample (98 pC/N). The improvement of piezoelectric properties is attributed to the deformation of the BNLT lattice caused by the incorporation of Ba^{2+} ions, which probable substitute Bi^{3+}, Na^{+} or La^{3+} ions at A-sites and/or Zr^{4+} ions, which substitute Ti^{4+} at B-sites of a BNLT perovskite structure. The difference in diameter of replacement ions induced a geometrical deformation of the BNLT lattice. This can lead to greater domain mobility, and therefore the piezoelectric properties are significantly enhanced [31,32].

Some electrical properties of the present work and results from other research groups are listed in Table 2. It should be noted that most of electrical properties of the present samples were enhanced by BZT addition. The optimum properties were observed at $x=0.09$ sample. Although the d_{33} value (126 pC/N) in this work is less than that found by Peng et al. [14] (147 pC/N), dielectric constant of our sample (~2400) was much greater than that found in the previous work (~880). Therefore, the $x=0.09$ sample was selected as the composition with optimum properties for this non-lead based system which offers a wide temperature range to use in electronic applications as an environmentally friendly piezoelectric material.

4. Conclusion

In the present work, $(1-x)$BNLT$-x$BZT ceramics with $x=0.00$, 0.06, 0.09 and 0.12 were prepared using a two-step mixed oxide method and a normal sintering technique. A perovskite phase with the mixing of rhombohedral and tetragonal symmetries was observed in all of the BNLT–BZT samples. BZT addition enhanced dielectric constant (ε_r) of BNLT ceramics while low dielectric loss (tan δ) remained. Furthermore, the d_{33} piezoelectric coefficient was improved by the BZT addition. Hysteresis loop of BNLT ceramics exhibited

a typical ferroelectric P–E loop and then deformed to antiferroelectric-like shape with increasing BZT content. The optimum composition for lead-free ferroelectric ceramics is $x=0.06$ because it has good ferroelectric properties with a high value of remanent polarization of 30.0 μC/cm^2 and a low coercive electric field of 20.8 kV/cm. However, the optimum composition for the lead-free piezoelectric ceramics is $x=0.09$, where the maximum values of the piezoelectric constant ($d_{33}\sim126$ pC/N) and dielectric constant ($\varepsilon_r\sim2400$ at 1 kHz) at room temperature were obtained.

Acknowledgments

The authors are thankful to financial support from SUT Research and Development Fund, Suranaree University of Technology.

References

[1] N. Pisitpipathsin, W. Koontasing, S. Eitssayeam, U. Intatha, G. Rujijanagul, K. Pengpat, T. Tunkasiri, Morphotropic phase boundary of lead-free piezoelectric ceramics from BNT–KN system, Advanced Materials Research 55-57 (2008) 225–228.

[2] P. Kantha, K. Pengpat, P. Jarupoom, U. Intatha, G. Rujijanagul, T. Tunkasiri, Phase formation and electrical properties of BNLT–BZT lead-free piezoelectric ceramics system, Current Applied Physics 9 (2009) 460–466.

[3] N. Pisitpipathsin, K. Pengpat, P. Kantha, W. Leenakul, S. Eitssayeam, G. Rujijanagul, T. Tunkasiri, Dielectric properties of lead-free solid solution of $Bi_{0.487}Na_{0.487}La_{0.017}TiO_3$–$BaTiO_3$, Phase Transitions 83 (2010) 875–883.

[4] N. Pisitpipathsin, P. Kantha, K. Pengpat, G. Rujijanagul, Influence of Ca substitution on microstructure and electrical properties of $Ba(Zr,Ti)O_3$ ceramics, Ceramics International 39 (Suppl. 1) (2013) S35–S39.

[5] P. Kantha, N. Pisitpipathsin, K. Pengpat, Enhanced electrical properties of lead-free BNLT–BZT ceramics by thermal treatment technique, Ceramics International 39 (Suppl. 1) (2013) S59–S63.

[6] J. Rodel, W. Jo, K.T.P. Seifert, E.M. Anton, T. Granzow, Perspective on the development of lead-free piezoceramics, Journal of the American Ceramic Society 92 (2009) 1153–1177.

[7] Q. Xu, X. Chen, W. Chen, S. Chen, B. Kim, J. Lee, Synthesis, ferroelectric and piezoelectric properties of some $(Na_{0.5}Bi_{0.5})TiO_3$ system compositions, Materials Letters 59 (2005) 2437–2441.

[8] D.Z. Jin, X.M. Chen, Z.C. Xu, Influence of dispersed coarse grains on mechanical and piezoelectric properties in $(Bi_{1/2}Na_{1/2})TiO_3$ ceramics, Materials Letters 58 (2004) 1701–1705.

[9] H. Nagata, T. Takenaka, Additive effects on electrical properties of $(Bi_{1/2}Na_{1/2})TiO_3$ ferroelectric ceramics, Journal of the European Ceramic Society 21 (2001) 1299–1302.

[10] A. Herabut, A. Safari, Processing and electromechanical properties of $(Bi_{0.5}Na_{0.5})_{(1-1.5x)}La_xTiO_3$ ceramics, Journal of the American Ceramic Society 80 (1997) 2954–2958.

[11] T. Takenaka, K. Sakata, K. Toda, Acoustic wave characteristics of lead-free $(Bi_{1/2}Na_{1/2})_{0.99}Ca_{0.01}TiO_3$ piezoelectric ceramic, Japanese Journal of Applied Physics (Suppl. 28-2) (1989) 59–62.

[12] T. Takenaka, K. Maruyama, K. Sakata, $(Bi_{1/2}Na_{1/2})TiO_3$–$BaTiO_3$ system for lead-free piezoelectric ceramics, Japanese Journal of Applied Physics 30 (1991) 2236–2239.

[13] R. Dittmer, K.G. Webber, E. Aulbach, W. Jo, X. Tan, J. Rodel, Electric-field-induced polarization and strain in $0.94(Bi_{1/2}Na_{1/2})TiO_3$–$0.06BaTiO_3$ under uniaxial stress, Acta Materialia 61 (2013) 1350–1358.

[14] C. Peng, J.F. Li, W. Gong, Preparation and properties of $(Bi_{1/2}Na_{1/2})TiO_3$–$Ba(Ti,Zr)O_3$ lead-free piezoelectric ceramics, Materials Letters 59 (2005) 1576–1580.

[15] B. Parija, T. Badapanda, S.K. Rout, L.S. Cavalcante, S. Panigrahi, E. Longo, N.C. Batista, T.P. Sinha, Morphotropic phase boundary and electrical properties of $1-x[Bi_{0.5}Na_{0.5}]TiO_3$–$xBa[Zr_{0.25}Ti_{0.75}]O_3$ Lead-free piezoelectric ceramics, Ceramics International 39 (2013) 4877–4886.

[16] H. Ishii, H. Nagata, T. Takenaka, Morphotropic phase boundary and electrical properties of bismuth sodium titanate—potassium niobate solid-solution ceramics, Japanese Journal of Applied Physics 40 (2001) 5660–5663.

[17] J.E. Daniels, W. Jo, J. Rodel, V. Honkimaki, J.L. Jones, Electric-field-induced phase-change behavior in $(Bi_{0.5}Na_{0.5})TiO_3$–$BaTiO_3$–$(K_{0.5}Na_{0.5})NbO_3$: a combinatorial investigation, Acta Materialia 58 (2010) 2103–2111.

[18] S. Mahajan, O.P. Thakur, D.K. Bhattacharya, K. Sreenivas, A comparative study of $Ba_{0.95}Ca_{0.05}Zr_{0.25}Ti_{0.75}O_3$ relaxor ceramics prepared by conventional and microwave sintering techniques, Materials Chemistry and Physics 112 (2008) 858–862.

[19] Y. Zhi, A. Chen, R. Guo, A.S. Bhalla, Dielectric properties and high tunability of $Ba(Ti_{0.7}Zr_{0.3})O_3$ ceramics under dc electric field, Applied Physics Letters 81 (2002) 1285–1287.

[20] P. Kumar, S. Singh, J.K. Juneja, C. Prakash, K.K. Raina, Influence of calcium substitution on structural and electrical properties of substituted barium titanate, Ceramics International 37 (2011) 1697–1700.

[21] F. Moura, A.Z. Simoes, B.D. Stojanovic, M.A. Zaghete, E. Longo J.A. Varela, Dielectric and ferroelectric characteristics of barium zirconate titanate ceramics prepared from mixed oxide method, Journal of Alloys and Compounds 462 (2008) 129–134.

[22] Z. Yu, C. Ang, R. Guo, A.S. Bhalla, Piezoelectric and strain properties of $Ba(Ti_{1-x}Zr_x)O_3$ ceramics, Journal of Applied Physics 92 (2002) 1489–1493.

[23] R.D. Shannon, Revised effective ionic radii and systematic studies of interatomic distances in halides and chalcogenides, Acta Crystallographica Section A 32 (1976) 751–767.

[24] S. Eitssayeam, U. Intatha, G. Rujijanagul, K. Pengpat, T. Tunkasiri, Structural and electrical properties characterization of $(1-x)PbZr_{0.52}Ti_{0.48}O_3$–$xBaFe_{0.5}Nb_{0.5}O_3$ system, Applied Physics A 83 (2006) 295–299.

[25] P. Jarupoom, K. Pengpat, N. Pisitpipathsin, S. Eitssayeam, U. Intatha, G. Rujijanagul, T. Tunkasiri, Development of electrical properties in lead-free bismuth sodium lanthanum titanate–barium titanate ceramic near the morphotropic phase boundary, Current Applied Physics 8 (2008) 253–257.

[26] S. Chopra, S. Sharma, T.C. Goel, R.G. Mendiratta, Structural, dielectric and ferroelectric properties of La doped $PbTiO_3$ sol–gel derived thin films, Ferroelectrics 327 (2005) 97–101.

[27] Y. Xu, Ferroelectric Materials and their Application, Elsevier Science Publishing Company, Inc., New York, 1991.

[28] J. Suchanicz, Behavior of $Na_{0.5}Bi_{0.5}TiO_3$ ceramics in the A.C. electric field, Ferroelectrics 209 (1998) 561–568.

[29] A. Prasatkhetragarn, N. Vittayakorn, S. Ananta, R. Yimnirun, D.P. Cann, Synthesis and dielectric and ferroelectric properties of ceramics in $(1-x)Pb(Zr_{1/2}Ti_{1/2})O_3$–$(x)Pb(Co_{1/3}Nb_{2/3})O_3$ system, Japanese Journal of Applied Physics 47 (2008) 998–1002.

[30] A.J. Moulson, J.M. Herbert, Electroceramics Materials, Properties, Applications, second ed., J. Wiley and Sons, New York, 2003.

[31] X.Y. Zhou, H.S. Gu, Y. Wang, W.Y. Li, T.S. Zhou, Piezoelectric properties of Mn-doped $(Na_{0.5}Bi_{0.5})_{0.92}Ba_{0.08}TiO_3$ ceramics, Materials Letters 59 (2005) 1649–1652.

[32] T. Takenaka, T. Okuda, K. Takegahara, Lead-free piezoelectric ceramics based on $(Bi_{1/2}Na_{1/2})TiO_3$–$NaNbO_3$, Ferroelectrics 196 (1997) 495–498.

สำเนา

1201002747

แบบสป/สผ/อสป/001-ก

คำขอรับสิทธิบัตร/อนุสิทธิบัตร

- ☑ การประดิษฐ์
- ☐ การออกแบบผลิตภัณฑ์
- ☐ อนุสิทธิบัตร

ข้าพเจ้าผู้ลงลายมือชื่อในคำขอรับสิทธิบัตร/~~อนุสิทธิบัตร~~นี้ ขอรับสิทธิบัตร/อนุสิทธิบัตร ตามพระราชบัญญัติสิทธิบัตร พ.ศ 2522 แก้ไขเพิ่มเติมโดยพระราชบัญญัติสิทธิบัตร (ฉบับที่ 2) พ.ศ 2535 และ พระราชบัญญัติสิทธิบัตร (ฉบับที่ 3) พ.ศ 2542

สำหรับเจ้าหน้าที่

วันรับคำขอ 28 มิ.ย. 2555	เลขที่คำขอ 1201002747
วันยื่นคำขอ 28 มิ.ย. 2555	
สัญลักษณ์จำแนกการประดิษฐ์ระหว่างประเทศ	
ใช้กับแบบผลิตภัณฑ์ ประเภทผลิตภัณฑ์	
วันประกาศโฆษณา	เลขที่ประกาศโฆษณา
วันออกสิทธิบัตร/อนุสิทธิบัตร	เลขที่สิทธิบัตร/อนุสิทธิบัตร
ลายมือชื่อเจ้าหน้าที่	

1.ชื่อที่แสดงถึงการประดิษฐ์/~~การออกแบบผลิตภัณฑ์~~
แก้วเซรามิกรูพรุนสำหรับใช้เป็นวัสดุชีวภาพ

2.คำขอรับสิทธิบัตรการออกแบบผลิตภัณฑ์นี้เป็นคำขอสำหรับแบบผลิตภัณฑ์อย่างเดียวกันและเป็นคำขอลำดับที่
ในจำนวน คำขอ ที่ยื่นในคราวเดียวกัน -

3.ผู้ขอรับสิทธิบัตร/อนุสิทธิบัตร และที่อยู่ (เลขที่ ถนน ประเทศ) มหาวิทยาลัยเชียงใหม่ เลขที่ 239 ถ.ห้วยแก้ว ต.สุเทพ อ.เมือง จ.เชียงใหม่ 50200 ประเทศไทย	3.1 สัญชาติ - 3.2 โทรศัพท์ 053-210731-2 3.3 โทรสาร 053-210733 3.4 อีเมล์ -

4.สิทธิในการขอรับสิทธิบัตร/อนุสิทธิบัตร
☐ ผู้ประดิษฐ์/ผู้ออกแบบ ☑ ผู้รับโอน ☐ ผู้ขอรับสิทธิโดยเหตุอื่น

5.ตัวแทน(ถ้ามี)/ที่อยู่ (เลขที่ ถนน จังหวัด รหัสไปรษณีย์) นางสาวภาณุวรรณ จันทวรรณกูร หน่วยจัดการทรัพย์สินทางปัญญาและถ่ายทอดเทคโนโลยี มหาวิทยาลัยเชียงใหม่ 239 ถนนห้วยแก้ว ตำบลสุเทพ อำเภอเมือง จังหวัดเชียงใหม่ 50200	5.1 ตัวแทนเลขที่ 1320 5.2 โทรศัพท์ 053-210731-2 5.3 โทรสาร 053- 210733 5.4 อีเมล์ panuwan@gmail.com

6.ผู้ประดิษฐ์/ผู้ออกแบบผลิตภัณฑ์ และที่อยู่ (เลขที่ ถนน ประเทศ)
1. ผศ.ดร.กมลพรรณ เพ็งพัด ที่อยู่ 171/126 ม. 7 ต.ไชยสถาน อ.สารภี จ.เชียงใหม่ 50140 ประเทศไทย
2. ศ.เกียรติคุณ ดร.ทวี ตันฆศิริ ที่อยู่ 155/3 ม. 2 ต.ช้างเผือก อ.เมือง จ.เชียงใหม่ 50300 ประเทศไทย
3. รศ.ดร.กอบวุฒิ รุจิจนากุล ที่อยู่ 244/155 ม. 4 ต.หนองควาย อ.หางดง จ.เชียงใหม่ 50230 ประเทศไทย

7. คำขอรับสิทธิบัตร/อนุสิทธิบัตรนี้แยกจากหรือเกี่ยวข้องกับคำขอเดิม
ผู้ขอรับสิทธิบัตร/อนุสิทธิบัตร ขอให้ถือว่าได้ยื่นคำขอรับสิทธิบัตร/อนุสิทธิบัตรนี้ ในวันเดียวกับคำขอรับสิทธิบัตร เลขที่ - วันยื่น - เพราะคำขอรับสิทธิบัตร/อนุสิทธิบัตรนี้แยกจากหรือเกี่ยวข้องกับคำขอเดิมเพราะ
☐ คำขอเดิมมีการประดิษฐ์หลายอย่าง ☐ ถูกคัดค้านเนื่องจากผู้ขอไม่มีสิทธิ ☐ ขอเปลี่ยนแปลงประเภทของสิทธิ

หมายเหตุ ในกรณีที่ไม่อาจระบุรายละเอียดได้ครบถ้วน ให้จัดทำเป็นเอกสารแนบท้ายแบบพิมพ์นี้โดยระบุหมายเลขกำกับข้อและหัวข้อที่แสดงรายละเอียดเพิ่มเติมดังกล่าวด้วย

8.การยื่นคำขอนอกราชอาณาจักร

วันยื่นคำขอ	เลขที่คำขอ	ประเทศ	สัญลักษณ์จำแนกการประดิษฐ์ระหว่างประเทศ	สถานะคำขอ
8.1				
8.2				
8.3				

8.4 ☐ ผู้ขอรับสิทธิบัตร/อนุสิทธิบัตรขอสิทธิให้ถือว่าได้ยื่นคำขอนี้ในวันที่ได้ยื่นคำขอรับสิทธิบัตร/อนุสิทธิบัตรในต่างประเทศเป็นครั้งแรก โดย

☐ ได้ยื่นเอกสารหลักฐานพร้อมคำขอนี้ ☐ ขอยื่นเอกสารหลักฐานหลังจากวันยื่นคำขอนี้

9.การแสดงการประดิษฐ์ หรือการออกแบบผลิตภัณฑ์ ผู้ขอรับสิทธิบัตร/อนุสิทธิบัตรได้แสดงการประดิษฐ์ที่หน่วยงานของรัฐเป็นผู้จัด

วันแสดง วันเปิดงานแสดง ผู้จัด

10.การประดิษฐ์เกี่ยวกับจุลชีพ

10.1 เลขทะเบียนฝากเก็บ	10.2 วันที่ฝากเก็บ	10.3 สถาบันฝากเก็บ/ประเทศ

11.ผู้ขอรับสิทธิบัตร/อนุสิทธิบัตร ขอยื่นเอกสารภาษาต่างประเทศก่อนในวันยื่นคำขอนี้ และจะจัดยื่นคำขอรับสิทธิบัตร/อนุสิทธิบัตรนี้ที่จัดทำเป็นภาษาไทยภายใน 90 วัน นับจากวันยื่นคำขอนี้ โดยขอยื่นเป็นภาษา

☐ อังกฤษ ☐ ฝรั่งเศส ☐ เยอรมัน ☐ ญี่ปุ่น ☐ อื่นๆ

12.ผู้ขอรับสิทธิบัตร/อนุสิทธิบัตร ขอให้อธิบดีประกาศโฆษณาคำขอรับสิทธิบัตร หรือรับจดทะเบียน และประกาศโฆษณาอนุสิทธิบัตรนี้ หลังจากวันที่ เดือน พ.ศ

☐ ผู้ขอรับสิทธิบัตร/อนุสิทธิบัตรขอให้ใช้รูปเขียนหมายเลข ในการประกาศโฆษณา

13.คำขอรับสิทธิบัตร/อนุสิทธิบัตรนี้ประกอบด้วย

ก. แบบพิมพ์คำขอ 3 หน้า

ข. รายละเอียดการประดิษฐ์ หรือคำพรรณนาแบบผลิตภัณฑ์ 6 หน้า

ค. ข้อถือสิทธิ 1 หน้า

ง. รูปเขียน 6 รูป 3 หน้า

จ. ภาพแสดงแบบผลิตภัณฑ์

☐ รูปเขียน รูป - หน้า

☐ ภาพถ่าย รูป - หน้า

ฉ. บทสรุปการประดิษฐ์ 1 หน้า

14.เอกสารประกอบคำขอ

☑ เอกสารแสดงสิทธิในการขอรับสิทธิบัตร/อนุสิทธิบัตร

☐ หนังสือรับรองการแสดงการประดิษฐ์/การออกแบบ ผลิตภัณฑ์

☑ หนังสือมอบอำนาจ

☐ เอกสารรายละเอียดเกี่ยวกับจุลชีพ

☐ เอกสารการขอนับวันยื่นคำขอในต่างประเทศเป็นวันยื่นคำขอในประเทศไทย

☐ เอกสารขอเปลี่ยนแปลงประเภทของสิทธิ

☐ เอกสารอื่น ๆ

15. ข้าพเจ้าขอรับรองว่า

☑ การประดิษฐ์นี้ไม่เคยยื่นขอรับสิทธิบัตร/ อนุสิทธิบัตรมาก่อน

☐ การประดิษฐ์นี้ได้พัฒนาปรับปรุงมาจาก.....

16.ลายมือชื่อ (☐ ผู้ขอรับสิทธิบัตร / อนุสิทธิบัตร; ☑ ตัวแทน)

(นางสาวภาณุวรรณ จันทวรรณกูร)

ตัวแทนผู้รับมอบอำนาจ

6.ผู้ประดิษฐ์/ผู้ออกแบบผลิตภัณฑ์ และที่อยู่ (เลขที่ ถนน ประเทศ) (ต่อ)

4. อ.ดร.สุขุม อิสเสง่ียม ที่อยู่ 100 ซ. 7 (ถนนช้างเผือก) ต.ศรีภูมิ อ.เมือง จ.เชียงใหม่ 50200 ประเทศไทย

5. น.ส.สุธาทิพย์ ทองเล่ม ที่อยู่ 1/13 ม. 4 ต.ฝายหลวง อ.ลับแล จ.อุตรดิตถ์ 53130 ประเทศไทย

(นางสาวภาณุวรรณ จันทวรรณกูร)

ตัวแทนผู้รับมอบอำนาจ